AUTOMATED ROLL-TO-ROLL FLUIDIC SELF-ASSEMBLY OF MICROSCOPIC INORGANIC SEMICONDUCTOR CHIPS FOR APPLICATIONS OF MACROELECTRONICS

A DISSERTATION
SUBMITTED TO THE FACULTY OF
UNIVERSITY OF MINNESOTA
BY

Sechul Park

IN PARTIAL FULFILLMENT OF THE REQUIREMENTS
FOR THE DEGREE OF
DOCTOR OF PHILOSOPHY

Heiko O. Jacobs, Advisor
Bethanie J. Hills Stadler, Co-Advisor

2015

© Sechul Park 2015

Acknowledgements

My pursuit of a PhD in Electrical Engineering at the University of Minnesota has been a great challenge but life-changing experience. The completion of this dissertation and my PhD degree would not have been possible without the invaluable support and help from many people. While I am thankful to everyone who has helped me, there are some specific individuals who have made significant contributions.

First and foremost, I would like to express my sincere appreciation and thanks to my advisor, Professor Heiko O. Jacobs for guiding and supporting me throughout my doctoral study. He continually challenged me to see problems in different ways in insight. He has also taught me how to conduct exploratory research in a professional way. I have acquired a great deal of both knowledge and skills under his guidance. I appreciate all his time, ideas, and funding which have supported me to complete this work.

I would also like to thank to my co-advisor, Professor Bethanie Stadler for all her support and encouragement throughout my doctoral study. Her considerable advice and assistance have helped me to continue my goal with passion. I could not have been succeeded without her heartfelt support. Also, I greatly appreciate my other doctoral committee members, Professor Jeong-Hyun Cho and Professor Philippe Buhlmann for their time and helpful discussions over the years.

I gratefully acknowledge the National Science Foundation (NSF-EECS-0822202 and NSF- ECCS-1068013) for their financial support of my research.

I will forever be thankful to my former and present Jacobs' research group members including Robert Knuesel, Jesse Cole, En-Chiang Lin, Chris Smith, Forrent Johnson, Yu Chen, Michael Motala, and Jun Fang for their assistance, hours of discussion, enjoyable moments, and continued friendship. My thanks also go out to the friends surrounding me for encouragement, advice, and counselling.

Last, but certainly not least, I would like to thank to my beloved family for all their unconditional supports, endless sacrifice, and love. Their faith and encouragement have motivated me to pursue my career goal and to complete this long journey.

Abstract

Macroelectronics has been widely used in our daily lives for flat-panel displays, large-area solar panels, flexible displays, and large-area lighting modules. Due to high demand on scaling-up of such devices, the focus of macroelectronics research has been a "larger" device, which is the opposite of traditional microelectronics where its aim is to produce a "smaller" device with high functional density. Since the realization of scaling-up requires high throughput and low-cost production, novel ways to overcome these challenges need to be addressed.

One of possible solutions is to distribute and integrate functional semiconductor materials over a large area in a parallel manner, overcoming current series robotic pick-and-place technique. There are several methods used in this approach, which are inkjet printing, parallel transfer, and engineered self-assembly.

The engineered self-assembly is one of promising candidates for scaling the system size to any desired level because it utilizes an entirely parallel process. In this thesis, we focus on the implementation of a novel self-assembly method, enabling the high throughput integration of microscopic inorganic semiconductor components over a large area on flexible and/or stretchable substrate.

We introduce an automated system to assemble functional semiconductor components using the fluidic self-assembly based on surface-tension by combining conveyer belt-like process and roll-to-roll approach with solder based self-assembly. The system includes component recycling and dispensing unit, roll-to-roll self-assembly unit, automated agitation, and web moving. The system enables the distribution, assembly, and electrical connection of semiconductor components in a continuous and parallel fashion over large area substrates. At present the installed system achieves an assembly rate of 15,000 chips per hour and an assembly yield of 99%, enabling assembly of standard square shaped dies, 300-1000 μm in size. Scaling the system to any desired throughput is possible due to the parallel manner of self-assembly. The identification and modeling of the relationship between process parameters and forces have been studied and experimentally verified by testing the effect of the web angle, agitation on assembly, and

detachment rates. We applied this optimized process to produce solid-state lighting modules which require the distribution, assembly, and electrical connection of inorganic light emitting diodes (LEDs) on flexible substrates. This particular application uses a conductive, flexible multilayer-sandwich-structure, achieved by combining the introduced assembly process with a novel lamination step. This lamination step is to replace the processes of wire-bonding and additional metallization.

We experimentally demonstrated a millimeter thin rubber-like solid-state lighting module. The fabrication of our lighting module is based on the assembly of LEDs on the stretchable bottom electrodes and the lamination of stretchable top electrodes for thin multilayer structures, forming electrical connection. The advantage of stretchable bottom and top electrodes is that they can relieve the mechanical stress when the device is bent. We expect this work to be extended to a heterogeneous system with a careful design of shape recognition and multi-batch assembly.

Table of Contents

Acknowledgements .... **i**

Abstract .... **ii**

Table of Contents .... **iv**

List of Tables .... **vi**

List of Figures .... **vii**

1. INTRODUCTION **1**

1.1 Motivation for Self-Assembly 1

1.2 Engineered Self-Assembly Technologies 6

1.3 Self-Assembly Process Based On Surface-Tension Driven Self-Assembly 13

2. INTRODUCTORY NOTE FOR THE SET OF THREE ARTICLES **15**

3. A FIRST IMPLEMENTATION OF AN AUTOMATED REEL-TO-REEL FLUIDIC SELF-ASSEMBLY MACHINE **17**

3.1 Introduction 18

3.2 Results and Discussion 20

3.3 Conclusion 36

3.4 Experimental 37

3.5 Axknowledgements 40

3.6 Supporting Information 41

3.7 *Advanced Materials* Table of Contents 43

4. APPROACHING ROLL-TO-ROLL FLUIDIC SELF-ASSEMBLY: RELEVANT PARAMETERS, MACHINE DESIGN, AND APPLICATIONS **44**

4.1 Summary 45

4.2 Introduction 45

4.3 Results and Discussion 48

4.4 Conclusions 71

4.5 Experimental 71

4.6 Acknowledgements 74

5. MILLIMETER THIN AND RUBBER-LIKE SOLID-STATE LIGHTING MODULES FABRICATED USING ROLL-TO-ROLL FLUIDIC SELF-ASSEMBLY AND LAMINATION 75

5.1 Introduction...76

5.2 Results and Discussion 79

5.3 Conclusion 94

5.4 Experimental...97

5.5 Axknowledgements...99

5.6 Supporting Information...99

5.7 *Advanced Materials* Table of Contents..104

6. CONCLUSION 105

7. BIBLIOGRAPHY 108

List of Tables

Table 4-1. Summary of the forces, their range, and use...64

List of Figures

Figure 3-1. Automated RTR fluidic self-assembly scheme..22

Figure 3-2. Micrographs depicting assemblies of 500 μm wide Si chips testing periodic and arbitrary chip assemblies with different densities...26

Figure 3-3. Optimization of the relevant forces and experimental validations...28

Figure 3-4. RTR fluidic self-assembly system applied to the fabrication of area lighting modules..33

Figure 3-5. Periodic assemblies of 500 (middle), 700 (top), and 1000 μm (bottom) sized Si chips with different thicknesses (200, 350, and 500 μm, respectively)..41

Figure 3-6. Functional 2×10 LEDs array assembled by using the proposed RTR assembly system 42

Figure 3-7 Table of Contents...43

Figure 4-1. Automated Roll-to-Roll fluidic self-assembly process................................48

Figure 4-2. Photographs showing assembly results of various sized Si components 52

Figure 4-3. Comparison of the relevant forces, fluid dynamics computation, and experimental validation...55

Figure 4-4. Flexible solid state lighting modules realized by the roll-to-roll fluidic self-assembly platform...68

Figure 5-1. Overview of the three basic steps used to fabricate a rubber-like solid-state lighting module..80

Figure 5-2. Schematics (A) and photographs (B) of the fabricated stretchable bottom electrode. 82

Figure 5-3. Computational analysis and photograph depicting strain (color coded) and mechanical torsion and flexing (Ansys) of the metal ribbons...84

Figure 5-4. Chip attachment using roll-to-roll fluidic assembly and photographs of the resulting structures...88

Figure 5-5. Schematics and photographs describing the design, fabrication, and application of the stretchable top conductive lamination layer next to results of a completed 2 mm thin rubber-like module under test 91

Figure 5-6. Comparison of mechanical properties of various interconnect designs such as large amplitude, small amplitude with many turns....................100

Figure 5-7. Fabrication procedure of the bottom electrode 101

Figure 5-8. Electrical resistance testing with stretching....................102

Figure 5-9. Fabrication procedure of the top conductive lamination layer 103

Figure 5-10. Table of Contents....................104

CHAPTER I

1. Introduction

1.1 Motivation for Self-Assembly

The manufacturing of man-made products including wireless communications, solid-state lighting modules, displays, and computers incorporate assembly/integration and electrical connection of various microelectronic devices. Moreover, the assembly/integration process becomes increasingly important in the emerging fields of macroelectronics where the integration of semiconductor devices over a large area is desired. Macroelectronics aims to enlarge overall device size, which is in contrast to microelectronics that focuses on miniaturization and higher functional density. In other words, the direction of macroelectronics is about realization of scaled up electronic devices, rather achieving higher integration density and/or reducing feature size. Applications of macroelectronics include flat panel televisions, flexible/wearable health monitoring systems, solid-state lighting modules, flexible displays, and large area solar cell panels [1]. The realization of macroelectronics requires large-area distribution/assembly of functional semiconductor materials on inexpensive, flexible, and even stretchable substrates. According to the best of the author's knowledge, there have been four representative approaches, which are inkjet printing, robotic pick-and-place,

parallel transfer, and engineered self-assembly. All of these enable the distribution and integration of functional semiconductor materials over a large area substrate. Inkjet printing is most suitable for forming low performance organic or organic/inorganic hybrid devices, whereas the parallel transfer, robotic pick-and-place, and engineered self-assembly are preferred for assembling high performance inorganic devices. This difference in target materials (organic or inorganic) leads to a distinction in the fabrication process between inkjet printing and the other techniques – parallel transfer, robotic pick-and-place, and engineered self-assembly. For example, inkjet printing is based on “bottom-up” process which forms organic semiconductor devices with a sequential printing of organic materials at low temperature to prevent damages on the organic materials, while in other methods the integration of inorganic semiconductor devices occurs at the end of fabrication process after high temperature processes. Inorganic semiconductors provide higher performance due to higher carrier mobility and higher functional density compared with organic semiconductors. In addition, the production of inorganic semiconductor is advantageous in that well-established semiconductor device manufacturing technologies can be utilized. In short, such advantages have contributed to the progress in the field of inorganic semiconductor integration including robotic pick-and-place, parallel transfer, and engineered self-assembly.

Robotic pick-and-place technique is a widely used technology in industry to integrate various types of microelectronic components, ranging from simple passive electronic components to complicated microprocessors. The advancement of robotic

pick-and-place technique has enabled the integration of various sized electronic components with high precision and fast integration speed. High-end robotic assembly systems have been demonstrated with alignment accuracy of few tens of micrometers and assembly speed of ~48,000 chips per hour for few hundred micrometer sized chips [2]. On the other hand, robotic pick-and-place method has some drawbacks. First, throughput is limited since the robotic pick-and-place machine is based on the serial assembly process. For example, the assembly head of the robotic machine assembles the chips sequentially, one by one. This indicates that the robotic machine is only suitable for the system incorporating a small number of components. Even though the high-end robotic assembly machines employ multi-assembly heads that can cover a large area substrate and increase throughput, the increased throughput and expandability of these machines are not sufficient for macroelectronics, where massive assembly of components over a large areas is desired. Second, non-specific adhesion force occurs between surfaces of assembly head and components. The adhesion force from Van-der-Waals interaction, electrostatic and surface tension, sometimes causes undesired attachment the microscopic components either between themselves and/or with the assembly head, hindering accurate positioning [3-5]. It is especially challenging to manipulate components smaller than a few hundred micrometers, where the adhesion force dominates the gravitational force. Therefore, the size of components manipulated using the robotic machine is limited to only a few hundreds of micrometers [6].

To overcome these shortcomings of the serial robotic pick-and-place, parallel transfer [7-10] and engineered self-assembly techniques [11-21] have emerged in

macroelectronics research. Some examples include flexible [22] and curved displays [12] curved focal plane arrays [9], oscillators [7], RF ID tags [23], and solar cells [10] integrating ZnO [24], GaAs [11, 12, 25], InP [26], GaN [14, 27], Si [7, 9, 12, 18, 20, 21, 28, 29] on flexible, inexpensive, and even stretchable substrates. Parallel transfer picks up pre-fabricated semiconductor devices from a donor wafer using solid and/or flexible stamps. The devices that are transferred onto the stamps are attached on a target substrate that has a stronger adhesion with the device than the stamp. Use of the donor wafers and stamps allows parallel integration of high performance inorganic circuit elements after high temperature fabrication process. The parallel transfer technique has successfully been realized in various applications such as conformable photovoltaics [30], stretchable batteries [31, 32], artificial electronic skins [33, 34], and mechanically soft and conformable health monitoring devices [35, 36]. Parallel transfer, however, has an inherent difficulty due to the use of the donor wafer, although this debate is still on going. The pitch and functional density of the final device would be inherently identical with that of the donor wafer since transfer process maintains the orientation, pitch, and functional density of the donor wafer. In other words, modifying and changing the pitch and density of assembled device segments in the final system would be a challenge in the parallel transfer method because the donor wafer determines the integration density. This is in contrast to the engineered self-assembly technique which provides more flexibility in designing the integration density by re-organizing the functional material at the desired location.

Engineered self-assembly provides a dramatically different approach from other methods. By nature, it is based on the self-assembly process which is easily observed in the

field of biochemistry, nanotechnology, and material science. A simple example of this process is the formation of a cell membrane, a complex biological system using phospholipid molecules as a building block. The self-assembly process is a fundamental tool in nanotechnology since this process allows the formation of complex structures by engineering or designing with this simple building block. Ralph Nuzzo's pioneering work that first demonstrated the self-assembly of alkanethiol on gold surface by engineering the building block of self-assembly process [37]. This lead to the engineered self-assembly technique gaining rapid progress, enabling the construction of the complex geometric systems such as "Borromean rings" by using engineered biological and non-biological building blocks [38, 39]. Moreover, self-assembly process is further extended across the length scale, bridging nanoscale to mesoscale [40-42]. For example, the formation of a complicated system of 3D photonic crystals in micrometer scale is achieved by design and manipulation of the simple building blocks of nanoparticles that are nanometer in scale [43]. Moreover, research on engineered self-assembly has enlarged the size of the building block from a few nanometers to a few micrometers [40, 44]. This capability can be applied to realize electronically functional multi-components systems. Engineered self-assembly enables massive parallel integration of components in large numbers with submicron spatial precision. In contrast to the parallel transfer with fixed pitch and functional density of the components, engineered self-assembly redistributes the components/chips over large area and orders the unorganized components to any desired pitch and functional density with sub-micrometer positioning accuracy. For example, using engineered self-assembly, it is possible that a pile of components in a container can be redistributed and rearranged to desired locations on a

flexible substrate. In addition, engineered self-assembly process can be scaled to any desired level due to its parallel nature.

1.2 Engineered Self-Assembly Technologies

Applications based on the principle of engineered self-assembly have ranged from the molecular level to functional semiconductor chip scale [40, 41, 44-46], including protein recognition [47-50], complementary DNA assembly [51-54], nanoparticle assembly [43, 45, 46], hydrophobic/hydrophilic patterning [55, 56], magnetic assembly [57-59], dielectric assembly [60], and electrostatic assembly [61-63]. Also, self-assembly is regarded as a fundamental technique in realizing complex nano-scale structures. Plasmonic nano-particle arrays on solid/flexible substrates [64, 65], 3D closed packed arrays [43, 45], and colloidal crystal arrays [66, 67] are representative examples. Particularly, under Professor Jacobs, my colleagues and I have focused on the surface-tension based directed-self-assembly process to assemble microscopic components [13-18, 20, 21, 68-70]. This approach – self-assembly of microscopic functional semiconductors – provides a new opportunity in manufacturing technologies that fabricate the complicated system that integrates and electrically connects micro-meter scaled semiconductor chips. Recently, much attention has been drawn to self-assembly of microelectronic chips such as a new cost-effective manufacturing method for flexible, large-area macroelectronics, replacing the deterministic serial robotic pick-and-place method.

Several approaches have been developed to locate the microscopic semiconductor components precisely using various forces such as magnetic force [71-73], gravitational force [11, 74], electrophoretic force [75], dielectrophoretic force [60, 76, 77], and surface tension

[78-82]. However, only two methods can achieve nearly perfect assembly results: assembly using complementary 3D shape and assembly using surface tension. The following sections will briefly introduce the published work on these two approaches.

1.2.1 Self-Assembly Based on Complementary 3D Shape

Complementary 3D shape assisted by gravity has been introduced to self-assemble functional microscopic components. The principle of complementary 3D shape-based self-assembly can be easily explained as "Lock and Key". For example, specifically shaped wells (Lock) can only be filled by correspondingly-shaped components (Key).

Yeh and Smith have developed a fluidic self-assembly method on the basis of complementary 3D shape and gravity [11, 74]. They used trapezoid shaped microscopic components and similarly shaped wells on rigid and flexible substrates in a fluidic environment. Hydrodynamic force from liquid flow delivers the components into the holes. Once the components are assembled in the hole with correct orientation, the components stay in the holes due to gravity and Van der Waals force, minimizing hydrodynamic force. Since the hydrodynamic force is proportional to the cross-sectional area of the component, which is exposed to liquid flow, only components with the wrong orientation will be easily repelled from the hole. After this process, electrical interconnection is formed using conventional photolithography. This approach successfully was adopted by Alien Technology to produce small radio frequency identification (RFID) tags [74] and to demonstrate solid-state lighting panel assembling GaAs LEDs [11].

Also, Böhringer and coworkers have adopted the "Lock and Key" concept with complementary 3D shape. They used protruding "pegs" to support in-plane orientation in air environment [83, 84]. This approach was further extended to provide in-plane orientation without complicated pegs. This approach uses shape recognition supported by capillary force. First, the rectangular components are aligned by going through apertures on a plate that have been assembled on a patterned substrate, and transferred to a secondary substrate with permanent bonding.

1.2.2 Self-Assembly Based on Capillary Force

Capillary force is one of the dominant forces in the assembly process of nano-sized objects, since other forces like gravity and inertial force become less effective at the nanometer scale. Capillary force, however, still plays a key role even at the millimeter scale [79-81, 85-89]. Whiteside and coworkers have developed a self-assembly process based on capillary force [90, 91]. They demonstrated self-assembly of millimeter sized components with hydrophobic patterned surfaces. Capillary forces between the suspended components in liquid drive the components into an ordered aggregation.

This assembly strategy has been adopted by Howe and coworkers, where they fabricated assembled structures onto a rigid substrate [79, 80]. They demonstrated self-assembly of micromirrors onto hydrophilic/hydrophobic patterned surfaces. They used self-assembly monolayer (SAM) with gold pad to form hydrophobic patterns on the substrate. These hydrophobic patterns were selectively wetted with polymer-based adhesive which also acted as a lubricant during assembly process. This technique provides assembly yield of 100% with sub-micrometer positioning accuracy. Using this

technique, Böhringer and coworker have demonstrated multi-batch self-assembly, sequentially integrating different types of components on a single substrate [78]. In this approach, a set of receptors coated with hydrophobic SAM was sequentially deactivated to prevent assembly at undesired location. Electrochemical method was used to deactivate receptor site by modifying the hydrophobicity of receptor. Deactivated receptor became more hydrophilic so that the polymer-based adhesive only wet on the activated receptors which were hydrophobic. After assembling the components on the adhesive coated receptor (active state, hydrophobic), the adhesive were cured at high temperature, bonding the component permanently. During the assembly process, the deactivated receptors turned into hydrophobic again due to the removal of SAM. This process was then repeated for another set of receptors and components to construct the heterogeneous system.

1.2.3 Self-Assembly Based on Surface-Tension of Molten Solder

The principle of self-assembly based on surface-tension of molten solder, pioneered by Whiteside and coworkers [91], is basically identical to the capillary force based self-assembly. However, the unique properties of metal alloys used as the viscous fluid in capillary force based self-assembly are noteworthy, specifically:

(i) Metal alloys such as low meting point solder have very high interfacial energy in water (~400mJ/m^2) comparing with that of viscous fluid which is used as lubricant and adhesive in capillary force-based self-assembly. Such high interfacial energy of liquid metal provides a stable, well-aligned assembly under external disturbances such as fluid drag and agitation.

(ii) The metallic joint, after solidification of a molten solder, supports stable mechanical properties.

(iii) Molten solder-based self-assembly enables self-assembly and formation of electrical interconnection simultaneously, since the metallic joint is electrically conductive. It is the most important and unique property of molten solder based self-assembly compared to other capillary forces based-methods using non-conductive polymer adhesive.

Gracias *et al.* extended Whitesides' pioneering work by fabricating self-folding 3D polyhedral structures [92]. He used lithographically pattern and released 2D unfold templates which contained metal alloy coated receptors at each joint. When the temperature of carrier liquid surrounding the released templates was raised above the melting point of the solder, the surface tension of the molten solder directed the receptors to form a spherical shape, generating a torque on the template face on a joint. This process resulted in the template folded into complex 3D structures.

Jacobs *et al.* further explored Whitesides work in another direction, fabricating a cylindrical display that included distributed, self-assembled, and electrically connected 300 μm sized GaAs light emitting diodes (LEDs) [12]. The components were realized using micromachining and dicing process. The display was fabricated in two steps:

(i) The self-assembly of the LEDs on the bottom electrode which contained the solder based receptors.

(ii) The self-alignment of the top electrode to complete electrical interconnection. The surface tension of molten solder drove both steps.

Jacobs and coworkers have made important advances towards adaptation of the self-assembly process in manufacturing industry. They developed the solder driven self-assembly process for the realization of heterogeneous 3D structures using a new approach combining the previous shape-recognition self-assembly and solder-driven self-assembly[13-15]. This approach employed sequential, shape recognition, and solder driven self-assembly to demonstrate the packaging of LEDs and electrical interconnection. They packaged the LED chips onto the solder based receptor in the trapezoidal well on glass carrier. The packed LED chips onto glass carriers were subsequently encapsulated into another glass encapsulation unit. The encapsulated chips, then, were applied to a printed circuit board (PCB) to realize LED array. This process was tailored to demonstrate heterogeneous multicomponent systems [ref] and multicomponent transponders. They also developed statistical models that support the theoretical relationship of the assembly time and yield with process parameters, demonstrating that the engineered self-assembly process is stochastic and can be realized with minimum defect levels [15].

The ability to form the heterogeneous system using sequential self-assembly has enabled the realization of 2D heterogeneous systems [20]. Chung *et al.* demonstrated the self-assembly of different color LEDs having same dimensions by programming the receptor [17, 21]. They fabricated the distinguished type of receptors by coating the various melting point solder. By controlling the assembly temperature, a specific set of receptors could be activated, and the corresponding LEDs were introduced and

assembled. Then, this process was repeated for another set of receptors, LEDs at different temperature to produce the multicolor LED array.

The solder-driven self-assembly enables the self-assembly with unique orientation. Zhang *et al.* introduced single-angle orientation self-assembly using 3D shape-confined structures [18]. This process is required particularly for the contact pad registration desired for device operation. For example, previous applications assembled the component with a square-shaped contact onto a square shaped receptor, with four indistinguishable angular orientations such as 0°, 90°, 180° and 270°. To realize a unique orientation assembly, this symmetry should be removed. Use of the geometric shape recognition combining solder-driven self-assembly provided the single angular orientation assembly in the 2D heterogeneous system.

Knuesel *et al.* also developed a novel engineered self-assembly method for the assembly of tiny functional semiconductor chips [68]. Previous research in the field of chip-scale self-assembly used gravitational sedimentation in combination with different methods such as shape recognition and capillary forces. However, the scale of components in previous self-assembly method based on gravity was limited to a few hundred micrometers, since gravity becomes insignificant under 100 μm length scale. To overcome this scale limitation, Jacobs and coworkers used a new approach combining solder driven self-assembly with energy cascade to eliminate the influence of gravity using triple (liquid-liquid-solid) interfaces. These interfaces define a progressing front line where the self-assembly takes place. In the developed process, the components are transported, pre-orientated at liquid-liquid interface, delivered to substrate, assembled to

predefined receptors, and electrically connected. Transportation and pre-orientation of the components were achieved by a cascade interfacial energy reduction. This process allows the assembly of tiny and discrete components onto rigid and flexible substrates. As an application, they demonstrated flexible solar modules, assembling 20 μm thick silicon solar cells. This approach was also tuned for self-tiling process which assembled pre-oriented tiny components onto larger receptor domains with periodic lattices [69, 70]. This self-tiling process increases surface area coverage of components on a substrate.

1.3 Automated Roll-to-Roll Fluidic Self-Assembly Process Based On Surface-Tension Driven Self-Assembly

Developing a self-assembly process that simultaneously integrates a large quantity of microscopic components over a large area with high throughput is possible due to the parallel manner of self-assembly. Previously reported self-assembly methods, however, are limited to small substrate area (typically, less than $1cm^2$) and small batch process performed by experienced researchers. Among all previously published methods, only the method reported by Yeh and Smith [11, 74] was successful at scaling up to industrial level. To overcome these limitations, we have implemented an automated roll-to-roll fluidic self-assembly system based on surface-tension driven self-assembly using solder based receptors. The developed system uses conveyor belt-like fashion with roll-to-roll process and incorporates automated agitation, controlled web-motion, continuous component recycling, and dispensing. The process enables distribution, assembly, and electrical connection of functional semiconductor components in a continuous and parallel fashion over a large area substrate. The installed apparatus demonstrated an assembly rate of 15,000 components per hour and an assembly yield of 99% for a 2.5 cm wide web with square shaped silicon components. This system was

applied to fabricate a solid-state lighting module including distribution, assembly, and electrical interconnection of inorganic LEDs. A novel lamination method was introduced to remove the wire-bonding process.

This process was extended to demonstrate assembly of multi-sized Si components ranging from 300 μm to 1000 μm, achieving an assembly yield of 99%. The identification and modeling of the relationship between the operation parameters and forces were studied to find optimal operation conditions. Then, these relationships were experimentally verified with assembly rates and detachment rates of the component under various operation conditions. Finally, we demonstrated a flexible solid-state lighting module.

The process was further optimized for realizing millimeter thin rubber-like foldable solid-state lighting module. We fabricated the module by assembling and distributing the 300 μm square, 115 μm tall LED chips using the system. The module is designed to be foldable. It is composed of 2 mm thin multilayer structures where inorganic LEDs are sandwiched between stretchable top (up to 130%) and bottom electrode (up to 170%), relieving the mechanical stress when the structure is bent. The specific design is based on mechanical stress profile calculation. The design leads to a hybrid structure, composed of non-stretchable assembly sites to accommodate the hard and rigid LEDs. Stretchable meander-shaped conductors are embedded in silicone rubber to complete the electrical connections to operate the LEDs.

CHAPTER II

2. Introductory Notes for the Set of Three Articles

As described in the abstract, this thesis discusses the procedure, modeling, and experiment results of the automated roll-to-roll fluidic self-assembly process with applications in the field of macroelectronics. The following chapters present three articles which have been published or submitted in peer-reviewed journals. The supporting information is included at the end of each chapter where applicable. A brief summary of each publication is provided below.

Chapter III (Publication 1, published) describes an implementation of prototype of automated roll-to-roll fluidic self-assembly based on surface-tension driven fluidic self-assembly using molten solder-based receptors. The system supports 15,000 chips per hour with high assembly yield of 99%, testing standard square shaped silicon chips. The realization of a solid-state lighting module is demonstrated, incorporating distribution, self-assembly, and electrical interconnection of LEDs. A novel lamination method of top conductive layer to complete electrical connection is discussed.

Chapter IV (Publication 2, in revision) discusses the assembly result testing standard square shaped components, 300 μm - 1000 μm in lateral size. This publication also describes the effect of the web angle, agitation on assembly, detachment rates, and fluid dynamics computation for better understanding of the underlying processes. We demonstrated a flexible solid-state lighting module.

Chapter V (Publication 3, published) presents a millimeter thin rubber-like foldable solid-state lighting panel, applying the roll-to-roll process. The structure includes 2 mm thin multilayer structures where assembled LEDs are placed between a stretchable top and bottom electrode to relieve the mechanical stress when the structure is bent. The design of this stretchable interconnect is based on mechanical stress calculations.

CHAPTER III

3. A First Implementation of an Automated Reel-to-Reel Fluidic Self-Assembly Machine

Se-Chul Park[1], Jun Fang[1], Shantonu Biswas[2], Mahsa Mozafari[2], Thomas Stauden[2], and Heiko O. Jacobs[1,2,*]

1 University of Minnesota, Electrical and Computer Engineering, Rm. 4-178, 200 Union St. SE, Minneapolis, MN 55455, USA

2 Fachgebiet Nanotechnologie, Technische Universität Ilmenau, Gustav-Kirchhoff-Strasse 1, Ilmenau, D-98693, Germany

Reprinted with permission,
Se-Chul Park, Jun Fang, Shantonu Biswas, Mahsa Mozafari, Thomas Stauden, and Heiko O. Jacobs, "A First Implementation of an Automated Reel-to-Reel Fluidic Self-Assembly Machine," Advanced Materials, 26 (34), 5942-5949, (2014)

Copyright (2014) John Wiley & Sons, Inc.

3.1 Introduction

Macroelectronics is a field or research to extend the application range of electronic and optoelectronic devices. In macroelectronics "larger" is considered better which is in stark contrast to the conventional field of microelectronics where "smaller" and a high function density was the most important driver. The field of macroelectronics requires novel solutions to spread functional materials and electronic or optoelectronic devices over increasingly large areas, on curved, flexible or even stretchable substrates. Most prominent methods use inkjet printing, parallel transfer [7-10], robotic pick-and-place [93, 94], and fluidic self-assembly [11-13, 18, 19]. Inkjet printing [95] is most suited to deposit low performance organic semiconductors and hybrid organic/inorganic structures while parallel transfer and self-assembly techniques target the integration of higher performance inorganic devices in a massively parallel fashion. Parallel transfer [7-10] and self-assembly techniques [11-13, 18, 19, 44] have been used to fabricate flexible [22] and curved displays [12], curved focal plane arrays [9], oscillators [7], RF ID tags [23], and PV modules [10] spreading ZnO [24], GaAs[13, 25], InP [26], GaN [14, 27], and Si [7, 9, 12, 28, 29] over large and unconventional substrates. Transfer techniques, when compared to engineered self-assembly methods, use a donor substrate/wafer and maintain orientation and integration density which is in stark contrast to directed self-assembly which can redistribute components over large areas and order unorganized parts. For example, a binned container full of semiconductor dies/chiplets of a certain type and quality can be redistributed and assembled at precise locations on a substrate at

any desired pitch or required functional density using methods of template directed self-assembly.

The field of template directed self-assembly continues to grow rapidly. However, when it comes to yield and assembly of semiconductor dies/chiplets only two methods are known to approach assembly yields of 100%. The first method uses gravity in combination with complementary 3D shapes to assemble trapezoidal Si dies onto plastic substrates [11, 74, 96]. The second uses gravity in combination with surface-tension-directed-self-assembly either using hydrophilic/hydrophobic surface patterns [44, 79, 84] or using solder-patterned surfaces to assemble and electrically connect semiconductor dies/chiplets on surfaces with similar yields [12-15, 18, 97]. Among all the methods that have been published the method first referenced in [11] remains the only method that has been scaled to be used in an industrial manufacturing process; the blueprints of the "self-assembly machine", however, has never been disclosed. Unfortunately, all published reports describe assemblies over small areas typically less than 1 cm^2 and in small discontinuous batch like self-assembly experiments involving manual agitation and an experienced scientist. Scaling to large areas appears to be a "hard problem" where there are fewer low hanging fruits, yet it appears absolutely necessary for the research community to demonstrate first blueprints to aid technology adaptation.

In this communication, we report on recent progress towards a first implementation of a self-assembly machine that is based on surface-tension-directed-self-assembly. The reported assembly process is no longer a discontinuous small-batch hand-operated process but resembles an automated machine like process involving a conveyer

belt and a reel-to-reel (RTR) type assembly approach with automated agitation. As a comparison, the assembly rate of conventional chip level pick-and-place machines depends on the cost of the system and number of assembly heads that are used. For example, a high-end FCM 10000 (Muehlbauer AG) flip chip assembly system can assemble approximately 8000 chips per hour achieving a placement accuracy of 30 μm. Our current design achieves 15k chips per hour using a 2.5 cm wide assembly region which is only a factor of 2 better than one of the faster pick-and-place machines; scaling to 150k chips per hour, however would be possible using a 25 cm wide web, which would be a factor of 20 faster. In principle, scaling to any throughput should be possible considering the parallel nature of self-assembly. In terms of placement accuracy our precision increase with a reduction of chip and solder bump size [18]. Generally, it exceeds the 30 μm limits for the components that have been used. Under optimized operational conditions, we achieved an assembly yield of 99.8% using the self-assembly process. As an application the assembly machine is applied to the realization of area lighting panels incorporating distributed inorganic light emitting diodes (LEDs).

3.2 Results & Discussion

Figure 3-1A describes the layout of the automated RTR fluidic self-assembly platform used in the experiments. The system has two main parts: (i) RTR assembly unit (shaded in gray) consisting of a servo motor, vibrator, rollers, and polyimide web to precisely control relevant parameters such as agitation, web moving speed, and tension of web as well as a (ii) component recycling and dispensing unit (shaded in blue) which uses the principle of a jet pump to transport unassembled components upward in a

confined fluid channel to be released above the substrate to tumble down on the basis of gravity. The system is designed to test various conditions including gentle component introduction to the receptors primarily on the basis of gravity providing the option to minimize the influence of liquid flow induced drag forces inside the large liquid filled funnel which was determined to be an issue in other unsuccessful designs. The components are transported to the inlet using a narrow channel (5 mm inner diameter tubing) which is placed 5 cm away from the polyimide web (50 μm thick, 5 cm wide) typically pointing not directly at the web. As the components enter the large volume the velocity reduces and the components drop down on the basis of gravity transitioning into a vertical trajectory which is the point where the web is located; assembly too close to the nozzle reduces capture rates due to excessive component speeds and drag forces of the injected liquid.

Figure 3-1B describes the attachment process of the chips on the advancing substrate. The substrates are based on conventional photolithographically patterned copper clad polyimide (50 μm thick, Pyralux® LF series, DuPont, NC) films whereby the copper squares (dimensions visible in the results) are coated with a low melting point solder through dip-coating. The solder coating is required for the self-assembly process. The self-assembly takes place in water which is heated to 80 °C using a controlled emersion heat exchanger to melt the solder (Indalloy #117, MP. 47 °C, Indium Corp., NY); higher melting point solder can also be used but requires a different higher boiling point liquid such as ethylene glycol[28]. The metal contact (Au or Cu) on the chips adhere to the molten solder based receptors on the surface. This adhesion is driven by the

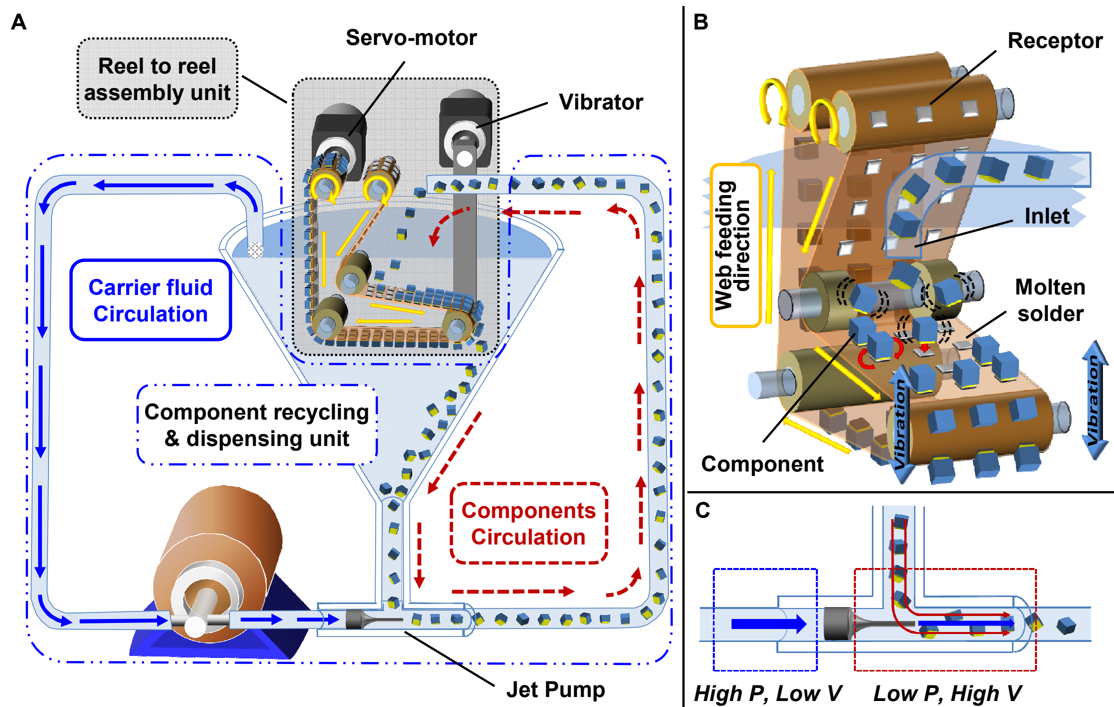

Figure 3-1. Automated RTR fluidic self-assembly scheme. (A) Overview depicting (i) component dispensing on the basis of liquid flow and gravity which transports the components to empty self-assembly sites (receptors) on a continuously advancing web, (ii) where the components attach at predetermined locations on the basis of surface tension directed self-assembly, and (iii) where recycling of access components is achieved on the basis of gravity at the turning point of the web before they are transported upward on the basis of a fluid drag inside a sufficiently small diameter channel. Mechanical up and down motion of the web is used to induce liquid flow and shear forces to dispense and agitate the components as well as to aid in the removal of excess component in the region of the upside-down oriented web. (B) Schematic depicting the details of surface tension directed self-assembly using molten-solder-bump-based-receptors to capture and connect to the metal contacts on the chips. (C) A jet pump based principle is used to achieve recirculation of the chips without passing the components through a mechanical pump where they would get damaged. A preferred location of the jet pump is at the bottom of the slanted funnel where access components arrive on the basis of gravity to be picked up by a high velocity directional jet.

minimization of the surface free energy of the liquid solder (400 mJ m^{-2} in water) yielding a stable, aligned, and electrically connected position. The process works particularly well if the pH of the water is adjusted to 2.0 (few drops of hydrochloric acid added) as this removes metal oxides from the surface of the solder drop; an oxide layer — if sufficiently thick — can block the wetting of the metal contact pads.

A typical web velocity using a single component deliver nozzle/zone is presently 10 meters per hour; higher velocities would require the use of multiple dispensing nozzles. As the components arrive at the inclined web a uniform distribution and sampling of the receptors is desired. The depicted process depends primarily on gravity driven sedimentation causing sliding and tumbling along the inclined web which can be adjusted using the inclination angle, typically 10 degree was favorable for the chip size used in the reported experiments. In addition, the web can be vibrated at a desired amplitude and frequency through an up-and-down motion of the lower roller which is one of the parameters that will be discussed in the results section. This additional gentle vibration aids in the spreading of the components and the removal of access components at the turning point of the web.

Reintroduction of access component at the top of the web requires either a pumping or conveyor belt type approach. The use of a normal mechanical pump such as rotary pump or diaphragm pump located in between the collection point and the dispensing nozzle failed as it led to mechanical damage to the semiconductor chips. The working alternative required the coupling of a mechanical pump (QV variable speed pump, Fluid metering, Inc., NY) with the illustrated custom made jet pump (Figure 3-

1C). The jet pump approach uses a smaller diameter nozzle (1.48 mm^2 in our design) to accelerate the carrier fluid into a desired direction; we typically use a velocity of 25 cm/s in the upward passage (20 mm^2 tubing) to drag the fairly dense semiconductor chips (density of 2.33 g cm^{-3}, versus 1.0 g cm^{-3} of water) upward to the dispensing head. Beyond this point the previously described gravity based sedimentation takes over again to determine the transport of the components finishing the cycle.

Figure 3-2 represents the self-assembly results testing a single component size and various receptor designs. The goal was to find out if (i) the location of the receptors on the substrate with respect to the edge of the substrate would present a challenge and cause an increase in the number of defects, (ii) if the orientation with respect to the component flow would matter, or (iii) if the self-assembly process would only support a certain pitch. In general terms we did not see a clear trend suggesting that the self-assembly process would prefer a certain pattern which means that the process is fairly robust enabling arbitrary and ordered assemblies at a desired pitch. In terms of yield the following numbers were found: Figure 3-2A shows 820 assembly sites, there were no missing and no excess chips present but 6 misaligned components reducing the yield to 99.3%; the misalignment was mainly due to an error in the solder bump height on 6 out of the 820 sites which is a limitation of manual dip-coating process that is currently used to fabricate the solder bumps [98].

An excessive solder height will lead to captured chips with variation in the tilt angle. In our experiments we used solder bumps that were 70 µm tall as measured in the center of the bump leading to a tilt angle variations of approximately 0.7°. A lower

thickness can reduce the tilt angle variations but would require a more involved process to apply the solder bumps.

This implies that the observed misalignments are not an integral part of the assembly system itself. Figure 3-2B depicts assembly results using arbitrary test patterns – a skeleton (left top), a walking person (left bottom), space invaders (right), and characters (bottom). The digitized patterns maintain the same pitch/or gap between nearest neighbors but have fewer numbers of assembled parts per area, specifically 29.8%, 41.9%, 49.1%, and 52.9% of the parts per area in (A). The question was to test if an irregular population would be somewhat more fragile than a regular population which was not the case. No defects were present in these assemblies. Figure 3-2C (upper half) represents a test using a hexagonal lattice where the spacing (340 μm) to the nearest neighbor/chip becomes smaller than the chip size (500 μm); this condition has been a challenge in previous reports [21] where an increase in chip entrapment in between such closely spaced receptors was reported; previous reports used a hand agitated drum like assembly approach and a slurry of access components which slid along the surface causing stronger shear forces and entrapment in between closely spaced receptors; this is no longer the case in the automated RTR assembly system where only a desired fraction of the chips interact with the assembly region causing less disturbance and defects (Figure 3-2C top shows 1396 assembly sites, 6 misalignments and 1 missing chip, representing a yield of 99.5%); Figure 3-2C bottom is the lower density counterpart with 365 assembly sites, one misaligned chip, 99.7% yield. In terms of overall numbers we are encouraged by the high yield since this begins to exceed deterministic robotic pick-and-

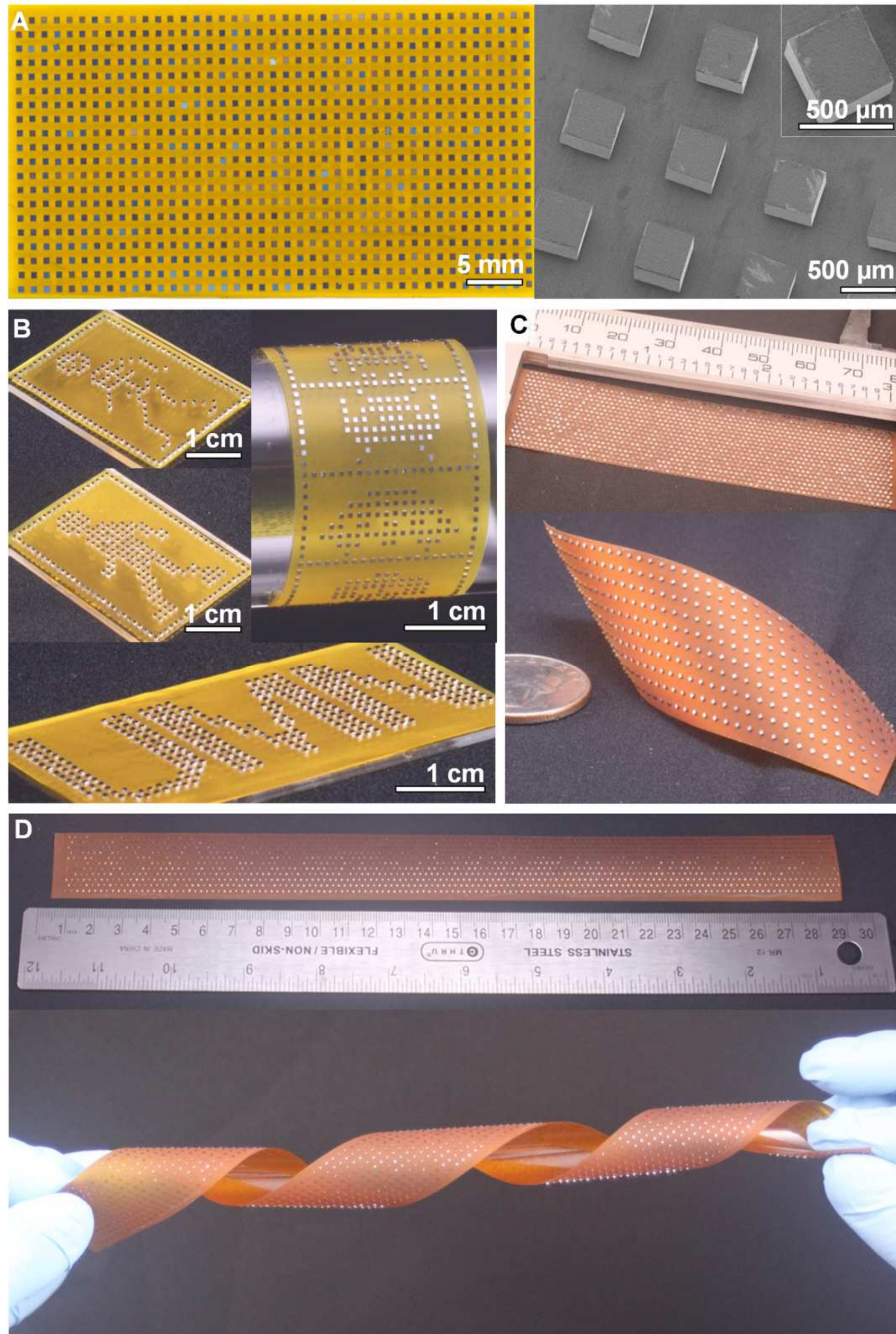

Figure 3-2. Micrographs depicting assemblies of 500 µm wide Si chips testing periodic and arbitrary chip assemblies with different densities. (A) Periodic assembly onto 1.1 mm pitched square lattice points, 820 chips, 6 defects. (B) Arbitrary assemblies representing a skeleton, a walking person, space invaders, and letters; in total 1163 chips no defects. (C) Periodic assemblies onto hexagonally located lattice points on a 1.05 mm (top, 1396 chips, 7 defects) and 4.2 mm pitch (bottom, 365 chips, 1 defect). (D) Overview depicting continuous assembly onto a 2 cm wide and 29 cm long assembly region.

place-like assembly methods that manipulate individual chips and that are at least an order of magnitude slower. Figure 3-2D depicts a 29 cm long and 2.5 cm wide assembly region with 1524 chips which took 6 minutes to assemble, 2 missing and 4 misaligned components were found in this sample representing a yield of 99.6 %. We did not observe a variance of the reported yield numbers across the areas which suggest that a single nozzle is sufficient to disperse the components across a 2 cm wide assembly zone. However, much wider webs are likely going to require an array of nozzles. We have not yet established the limits of the self-assembly process in terms of chip sizes that can be assembled. At this point we have done a few experiments that suggest that the process is capable to assemble 300 to 1000 μm sized chips with a thickness in the range of 200 to 500 μm. Preliminary tests assembling 500, 700, and 1000 μm sized Si chips are shown in Figure 3-5 (supporting information).

The results presented previously (Figure 3-2) were based on optimized operational conditions of the system considering component spreading on the web, component attachment on the web, and removal of access components. The operational conditions were carefully determined through the calculation of the relevant forces and experimental validations as summarized in Figure 3-3. Substrates with a constant 1.1 mm pitch (defined as the center-to-center distance between chips) were used in our experimental validation of the theory and optimization of the process parameters.

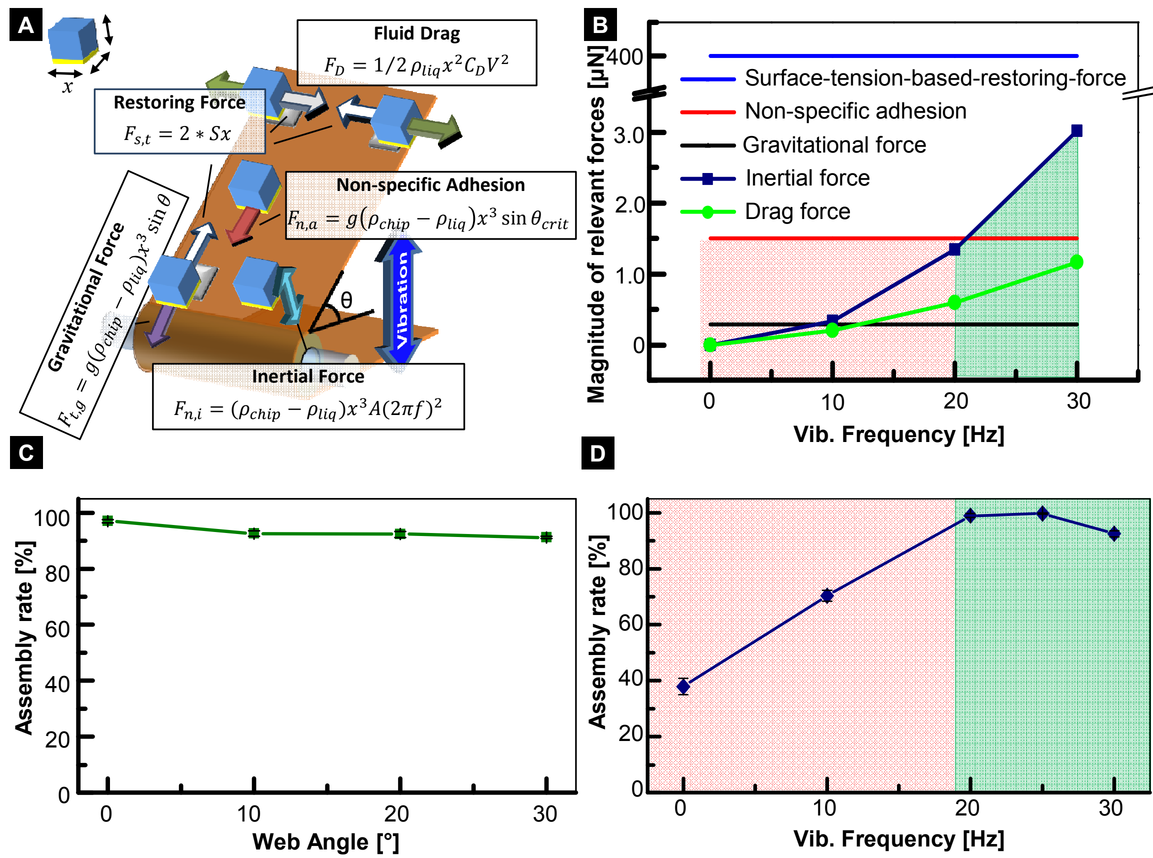

Figure 3-3. Optimization of the relevant forces and experimental validations. (A) Relevant forces due to surface tension, gravity, non-specific adhesion, inertia and fluid drag; the inertia and fluid drag are a result of an up-and-down vibrational web motion. (B) Comparisons of relevant force components with different vibration conditions. Experimental validation and optimization scheme studying the (C) assembly rate as a function of web angles, (D) assembly rate as a function of vibrational frequency.

Figure 3-3A depicts the relevant force components, specifically:

(i) The Surface-tension-based-restoring-force of a molten solder ($F_{s,t} = 2 * Sx$); the equation is valid if the chip is pulled out of alignment in the tangential direction to a point where the amount of misalignment exceeds the solder thickness [99]. The tangential restoring force is approximately 400 μN considering the 0.5 mm cube and 400 mN m^{-1} surface tension (*S*) of the solder; the chips in the illustrations are pulled out of alignment due to a gravitational force or drag force; actual misalignments are much smaller than what is illustrated. ***(ii)*** The tangential gravitational forces ($F_{t,g} = g(\rho_{chip} - \rho_{liq})x^3 \sin\theta$) on angled web is approximately 1.7μN*sinθ for a 0.5 mm Si cube (0.3 μN for 10° tilted web). ***(iii)*** The non-specific adhesion forces ($F_{nonspecific\ adhesion} = g(\rho_{chip} - \rho_{liq})x^3 \sin(\theta_{crit})$) due to static friction, surface tension, Van-der-Waals forces of the semiconductor chips on the polyimide web is important since these forces impacts the amount of spreading of the chips. For a 0.5 mm Si cube, this non-specific adhesion forces is 1.5 μN with critical angle (θ_{crit} = 60°, experimentally observed) which is the required angle to cause siding motion of previously static chips on the web; at this angle, the gravitational forces start to exceed the non-specific-adhesion. ***(iv)*** The inertial force due to the harmonic web oscillation with amplitude *A* and frequency *f* ($F_{n,i} = (\rho_{chip} - \rho_{liq})x^3 A\ (2\pi f)^2$); this equation is valid in the regime where the chips remain in contact with the web. ***(v)*** The fluid drag forces ($F_D = 0.5\rho_{liq}x^2 C_D V^2$) due to the oscillating shear flow originated from up-and-down vibrational motion of the web; the quadratic drag equation [100] needs to be used rather than Stoke's drag since the calculated Reynolds number exceeds 100 considering a 0.5

mm Si cube in water. To calculate the drag force, we assumed that the shear flow velocity (V) is comparable to oscillating speed of web ($A*2\pi f$). For example, a 0.5 mm 30Hz vibration represents a peak velocity of 100 mm s^{-1} and a drag force of approximately 1.3 μN.

Figure 3-3B compares the relevant force components that act onto the chips in our system as the vibration frequency is increased from 0 to 30Hz; all calculations assume a Si cube with a side length x = 0.5 mm, an optimized 10° tilt angle, and an optimized 0.5 mm vibration amplitude. The horizontal lines represent non-specific-adhesion, gravity, and surface tension based restoring force; the green and blue lines represent fluid drag and inertial force which both increase with web vibration frequency. At low frequencies (***red regime***), the chips are predicted to remain in contact with the web since the non-specific-adhesion (a few μN) and the gravitational force push the components in contact (1.7μN*cos(θ)), this condition is not desired since the chips reside in one point and do not move around to participate in the self-assembly; this general behavior is observed in the experiments. At 20Hz (***green regime begins***) the inertial force that acts on the components is predicted to become sufficiently strong to overcome gravity; separation and hopping of components should begin to occur. The actual hopping is difficult to observe in the experiments, however, the onset of a collective downward sliding motion that leads to a sampling of the receptors occurs once the 20Hz is reached in our experiments. Once the downward motion takes place the chips show a small sideway oscillatory motion which can be explained by the pulsating liquid drag. The calculated

dependencies have clear implications on the assembly rate and yield which can now be directly measured and understood:

First, we recorded the effect of gravity on the assembly rate (Figure 3-3C) testing various tilt angles. In each consecutive experiment (5 experiments per data point) we recorded the number of captured components for a constant assembly time of 3 minutes using a constant level of web vibration (0.5 mm amplitude and 30Hz frequency). A depicted value of 98% means that 98% of the receptors captured a chip within 3 minutes leaving 2% of the receptors vacant. The capture rate decreases slightly towards higher tilt angle since the chips begin to slide too fast; some slide over a solder bump and are not immediately captured.

Second, and in analogy to the predictions made in figure 3-3B we recorded the effect of vibration frequency (0 - 30Hz) (Figure 3-3D) in consecutive experiments (5 experiments per data point) maintaining constant vibration amplitude (0.5 mm) and tilt angle (10°). The green and red regimes can be found again. As predicted at low vibration frequency (0 - 10Hz, red regime), the progression of the self-assembly was slow and non-uniform. A portion of the chips remains stationary because the agitation is insufficiently strong to overcome non-specific-adhesion and gravity; most of the assembly takes place towards the center of the web due to an insufficient spreading. At 20 to 25Hz the progression of the self-assembly reaches an optimized value (green regime), the chips are distributed uniformly across the surface and slide slowly in one direction is supported by the calculations made above.

We have also adjusted the tilt angle and vibration amplitudes. Without going into the details we would like to point out that 10° represents an optimized tilt angle. Higher values lead to a faster sliding motion which in turn reduced the capturing rate since more chips slid over a solder bump before being captured. This should be investigated further in the future. Equally the 0.5 mm vibration amplitudes represented an optimized value for the chip size used in this study. Higher amplitudes lead to lateral oscillatory motion of the chips which exceeded the size of the solder bumps which in turn reduced the capturing rate. We think that more research is required. However, the goal so far was to demonstrate that perfect functional assemblies can be produced and that processes of self-assembly can exceed the yield of conventional deterministic manufacturing such as serial robotic pick and place. This goal has been reached using the presented parameters and we are convinced that the process can be tailored to various applications. Of particular interest are applications where low cost and assembly of objects in large quantities is desired. One example is briefly discussed below.

Figure 3-4 provides one example where the process is applied to the assembly of GaN LEDs targeting an application in the cost effective production of area lighting modules on the basis of distributed solid state light sources. We used LEDs, unpackaged n-GaN/p-GaN thin LEDs with a side length of 500 μm and a height of 190 μm (F4142L, OSRAM) as device segments. As shown in Figure 3-4A, the area lighting modules are fabricated in three steps: (i) assembly of LEDs on the bottom electrode using the RTR system, (ii) isolation and passivation of assembled LEDs with UV curable polymer, and (iii) lamination of top conductive layer to complete the electrical connections.

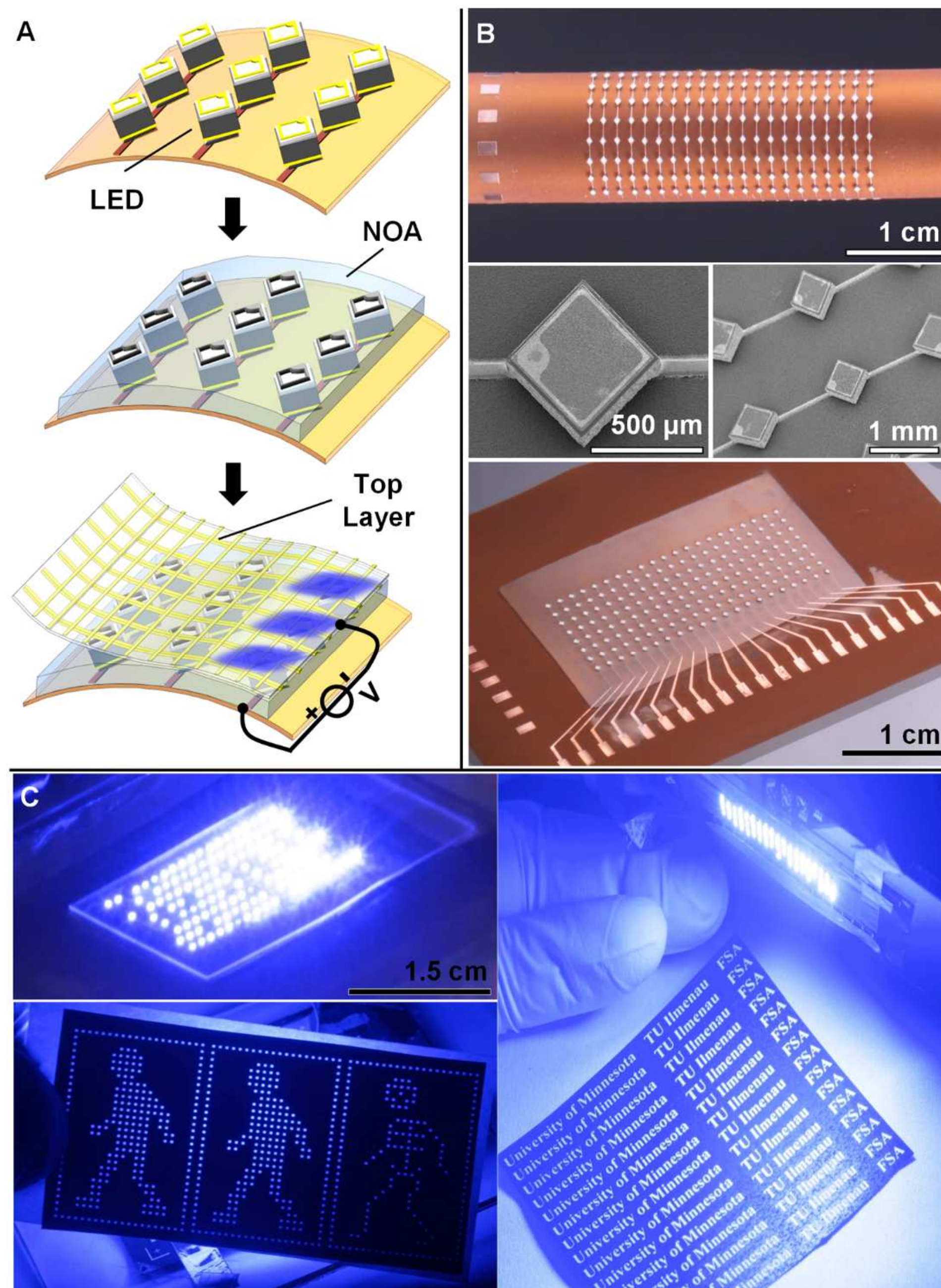

Figure 3-4. RTR fluidic self-assembly system applied to the fabrication of area lighting modules. (A) Fabrication procedure: Assembly of LED using the RTR fluidic self-assembly system, area isolation and passivation of assembled LEDs with UV curable polymer (NOA), and lamination of top conductive layer. (B) Optical photograph of assembled LEDs wrapped onto a cylinder (Top), SEM close-ups (middle), and optical photograph after isolation using UV curable polymer (bottom). (C) Application as lighting panel (Left, top), backlighting unit (Left, bottom), and area illumination unit (Right).

First, for the successful assembly of the LEDs (Figure 3-4B, top) the following conditions were used. The substrates were identical to the ones used above with the exception that each pad is connected to an interconnecting line. The interconnecting lines are protected with a dry film to prevent solder wetting and assembly of LEDs in this region; see materials and methods sections for more details. A higher vibrational amplitude (2 - 3 mm) was required when compared to the Si components; the reason is that the LED has a gold top contact; the gold top contact is 25 times smaller than the bottom contact; however, attachment with the wrong orientation can occur under the wrong conditions. This was prevented using a higher vibrational amplitude.

Second, after assembly a UV curable polymer (NOA 73, Norland Optical Adhesive, NJ) is used as a separation layer between the top and bottom contact (Figure 3-4B, bottom). To apply this isolation layer we first place a polydimethylsiloxan (PDMS, Sylgard® 184, Dow Corning Co.) block on the assembled LEDs to protect the topside of the LEDs. The matrix in between is subsequently filled using a UV curable polymer through capillary action. Unfortunately, this process is not perfect and polymer residues can be present on the top of the LEDs which need to be removed using O_2 plasma cleaning step (60 seconds). More details are described in materials and method sections.

The ***third*** step of the fabrication procedure is a lamination step whereby the top conductive layer is applied. The third step is a new approach which has not yet been optimized. The goal was not to use an evaporation step or wire-bonding but to find an alternative contacting method that would not require any vacuum processing in the long run. The approach was in part inspired by the ability to form a conformal electrical

contact by simply placing a metal coated polymeric material (for example a gold coated PDMS stamp with correct thickness) onto the surface that needs to be electrically contacted; we demonstrated that this is possible in the past [61], and the approach has later been used in a modified form by others to contact and transfer metal contacts on secondary surfaces [8, 9, 101]. A problem with the original method is that the adhesive force is primarily based on Van-der-Waals adhesion which cannot be tailored to be as large as one would like in certain applications. Instead of transferring a metal contact onto the surface we decided to test a two-phase-material approach where portions of the surface are adhesive (and less conductive) and other portions are conductive (and less adhesive) to tailor the properties to desired levels. In the simplest form, the approach can be described to make use of a metallic mesh (Figure 3-4A, bottom) which is surrounded by an adhesive surface whereby the adhesive is used to maintain a close contact to the surface of the LEDs; once attached the conducting traces remain fixed in place through the surrounding adhesive. The problem of alignment can be circumvented by choosing a mesh periodicity which is smaller than the widths of the contact pad on the top of the LEDs (100 μm in our design). To test this new contacting scheme a 7 cm x 7 cm wide gold mesh is fabricated using standard photolithography involving evaporation of 250 nm thick layer of gold without adhesion layer on a bare Si wafer, wet chemical etching, and final transferred to a clear commercially available tape (3M Scotch tape, 3M). The resulting conducting tape is then applied to contact the top of the LEDs. Figure 4C provides images of functional arrays that have been produced so far. The approach has not yet been optimized and the results are not perfect as a consequence; most LEDs light

up (~ 90%) but some can be found where no contact was made (Figure 3-4C). The optimization of the top contact is outside of the focus of the sponsored research project dealing with self-assembly. Anyway it would be interesting to test various pitches and metal thicknesses. In the long term it would be required to have a simple contacting scheme to provide a more cost effective alternative to conventional serial wire-bonding. Nevertheless, we have also tested standard wire-bonding and were able to produce defect free lighting modules Figure 3-6 in supporting information.

3.3 Conclusion

This publication provides the blueprints and operational parameters of a first RTR fluidic self-assembly platform to assemble and electrically connect semiconductor chips with a yield clearly exceeding a 99% benchmark set by robotic pick and place machines. At present the installed apparatus supports an assembly rate of ~15k chips per hour using a 2.5 cm wide web testing standard square shaped dies 500 µm in size; scaling to 150k chips per hour would require a 25 cm wide web. The technology is completely different from conventional deterministic robotic assembly and the industry that develop around it. Most importantly the fluidic self-assembly approach is entirely parallel and does not require any pick and place operations. This means that it is fairly straight forward to scale this technology to any desired assembly rate by increasing the substrate width and number of nozzles. We are convinced that the key to the high yield and high alignment accuracy is inherently related with the high restoring force of liquid solder bumps that we continue to use in our experiments. Over many years we have experimented with other forces including Coulomb forces [102], hydrophobic and hydrophilic forces [68],

magnetic (not published), gravity and shape recognition and we have yet to find another approach that achieves a similar yield and alignment accuracy. The approach can be extended using shape recognition concepts to enable unique angular alignment and contact pad registration [15, 18, 19] or using sequential batch assembly processes [13, 78] to assemble more than one component type on the substrate if desired. Moreover, it is possible to transfer the chip onto other flexible or stretchable substrates. It should also be possible to extend this scheme towards smaller chips sizes in the future.

3.4 Experimental

3.4.1 Si components

500 μm in lateral size Si components were fabricated using 200 μm thick Si wafers (University Wafers, Boston, MA) that were first cleaned using a standard RCA clean: 1:1:5 solution of $NH_4OH + H_2O_2 + H_2O$ at 80 °C for 15 min; 1:50 solution of HF + H_2O at 25 °C for 15 s; 1:1:6 solution of $HCl + H_2O_2 + H_2O$ at 80 °C for 15 min with a DI water rinse after each step. Following the clean, 10 nm Cr and 200 nm Au layers was deposited using an e-beam evaporator. Photoresist (Microposit 1813, Shipley) was then spin coated at 3,000 rpm for 30 sec. After a soft-bake at 105 °C for 1 min, the substrate was exposed with 90 mJ/cm^2 UV light and developed in 1 Microposit 351 : 5 H_2O developer for 25 sec. The Au and Cr layers were subsequently wet-etched using a gold etchant (GE-6, Transene Inc, MA) for 45 sec and a chromium etchant (CR-12S, Cyantek Corp., CA) for 5 sec, respectively. The photoresist was removed using a reactive ion etch (O_2, 100 sccm, 100 W, 100 mTorr). Finally, the wafer was diced using a fully automated

dicing machine. To prevent damage and contaminations, the gold contact was protected with a photoresist (Microposit 1813, Shipley) during the dicing step.

3.4.2 Self-Assembly Substrate

A copper cladded conventional flexible printed circuit board material is the starting material (Pyralux® LF series, DuPont, NC). The 20 µm thick Cu cladding is cleaned with a 1 HCl : 10 DI water solution, DI water, methanol, acetone, isopropyl alcohol. Dry film (Optical resist, Alpha 300, Megauk, UK) is laminated on the top using a tension controlled laminator at 95 °C with 250 kPa, exposed with 55 mJ/cm^2 UV light through a transparency mask, and developed in 2% K_2CO_3 in room temperature for 50 sec. Following the development, the unprotected copper is removed through etching in a 30% $FeCl_3$ solution in 5 min. The dry film is stripped in a 4% KOH solution at 40 °C leaving bare copper squares (receptors) on the substrates. The substrate is rinsed in DI water. Finally, the copper pads are coated using a low melting point solder (Indalloy #117, MP. 47 °C, Indium Corp., NY) through dip coating in a preheated solder bath in order to realize the predefined receptors; the solder baths contains a layer of water on top of the heavier solder to prevent oxidation of the solder. Drops of HCL can be added to the water covering the liquid solder to remove any surface oxides on the solder if present. The surface of the liquid solder should be mirror like.

3.4.3 SSL application

3.4.3.1 Bottom electrode

The fabrication of the bottom electrode follows the lithographic procedure above with the exception that a second layer of dry film and lithography is used to protect the electrical interconnection line from being coated with solder during the dip coating process.

3.4.3.2 Isolation using NOA

Following self-assembly of LEDs, a fully cured PDMS (Sylgard® 184, Dow Corning Co.) stamp was placed on the top of assembled LED array under moderated pressure. UV curable polymer (NOA 73, Norland Optical Adhesive, NJ) was dispensed on the side of PDMS stamp to fill the gap on the basis of capillary action. The NOA was cured under UV light. NOA residues were found on some of the LEDs which required a de-scum using a reactive ion etcher for 60s (CF_4: 20 sccm, O_2: 80 sccm, 200 W).

3.4.3.3 Top Electrode Lamination Layer

250 nm Au was deposited using an e-beam evaporator onto a bare Si wafers (University Wafers, Boston, MA) that was previously cleaned in a solution of H_2SO_4 + H_2O_2 for 15 min and rinsed with DI water. No adhesion promoter was used. Photoresist (Microposit 1813 Shipley) is applied (4,000 RPM), exposed, and developed in Microposit 351 : 5 H_2O developer (25 s). The Au layer is etched in a gold etchant (GE-6, Transene Inc, MA) for 50 sec, washed in isopropyl alcohol, and carefully dried. The patterned Au

mesh is transfer printed onto a clear adhesive tape (3M scotch tape) which is then used to contact the top of the LEDs through lamination.

3.5 Acknowledgements

The research received financial support in part through grants from the National Science Foundation (NSF Grant DMI-1068013), German Science Foundation (DFG Grants JA 1023/3-1), and the Carl-Zeiss Foundation

3.6 Supporting Information

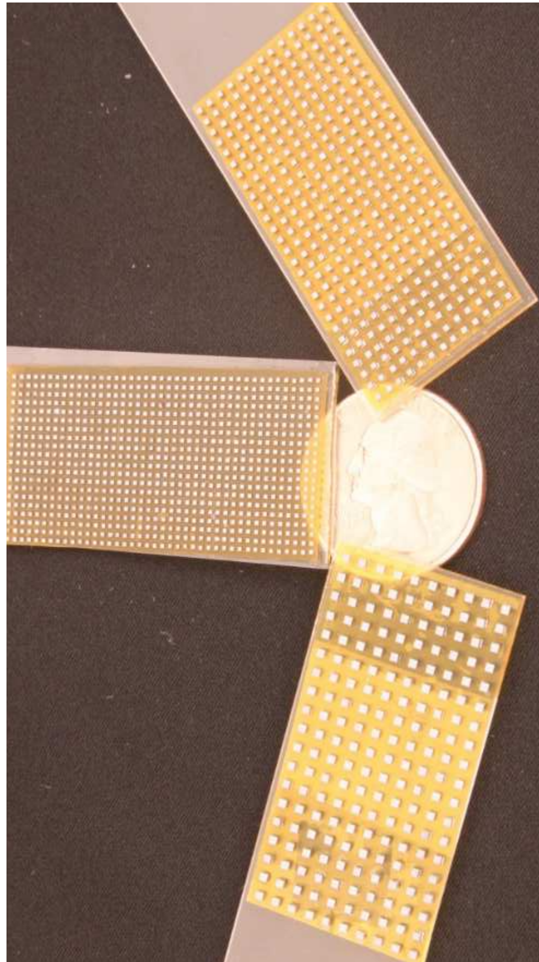

Figure 3-5. Periodic assemblies of 500 (middle), 700 (top), and 1000 μm (bottom) sized Si chips with different thicknesses (200, 350, and 500 μm, respectively).

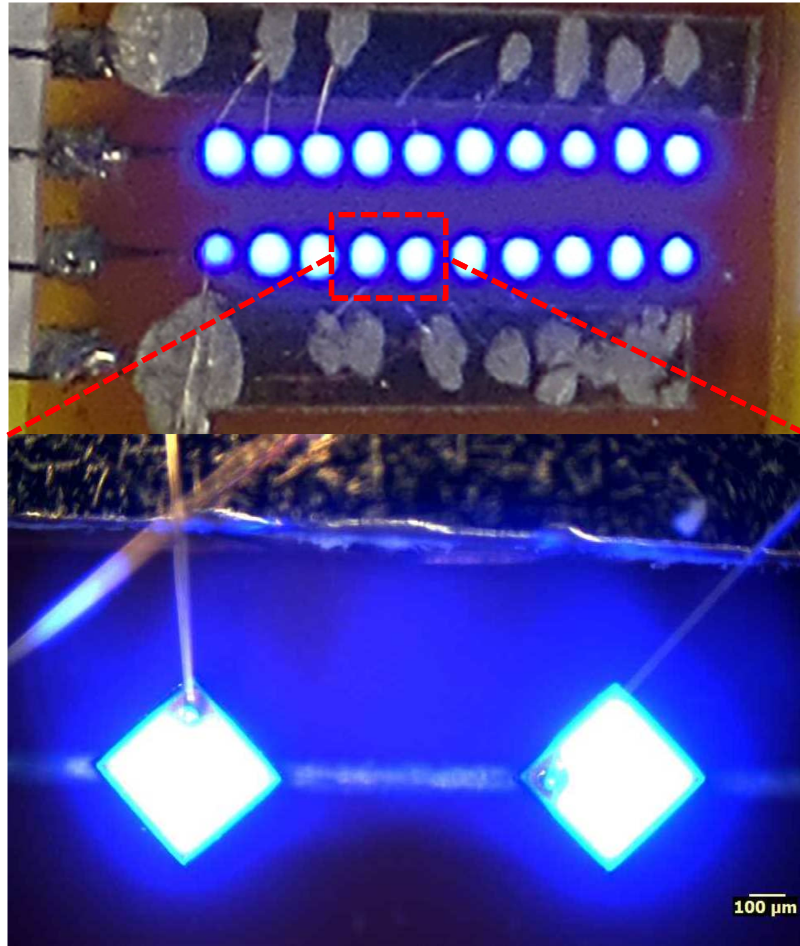

Figure 3-6. Functional 2×10 LEDs array assembled by using the proposed RTR assembly system. Standard wire-bonding method was used to make electrical connection on the top electrode on LEDs.

3.7 *Advanced Materials* Table of Contents

A first automated-reel-to-reel-fluidic-self-assembly process for macroelectronics applications is reported. This system enables high speed assembly of semiconductor dies (15,000 chips/hour using 2.5 cm wide web) over large area substrates. The optimization of the system (>99% assembly yield) is based on identification, calculation, and optimization of the relevant forces. As an application the production of a solid state lighting panel is discussed involving a novel approach to apply a conductive layer through lamination.

Keyword : reel to reel process, fluidic self-assembly, flexible electronics, solid state lighting.

Se-Chul Park, Jun Fang, Shantonu Biswas, Mahsa Mozafari, Thomas Stauden, and Heiko O. Jacobs

A First Implementation of an Automated Reel-to-Reel Fluidic Self-Assembly Machine

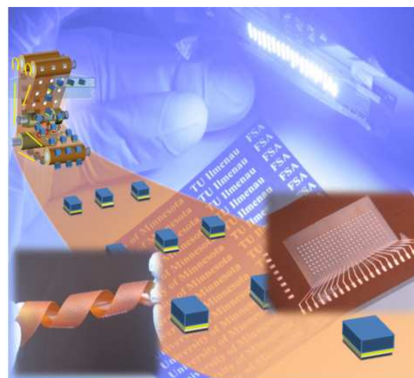

Figure 3-7. Functional 2×10 LEDs array assembled by using the proposed RTR assembly system.

CHAPTER IV

4. Approaching Roll-to-Roll Fluidic Self-assembly: Relevant Parameters, Machine Design, and Applications

Se-Chul Park[1], Jun Fang[1], Shantonu Biswas[2], Mahsa Mozafari[2], Thomas Stauden[2], and Heiko O. Jacobs[1,2,*]

1 University of Minnesota, Electrical and Computer Engineering, Rm. 4-178, 200 Union St. SE, Minneapolis, MN 55455, USA

2 Fachgebiet Nanotechnologie, Technische Universität Ilmenau, Gustav-Kirchhoff-Strasse 1, Ilmenau, D-98693, Germany

Reprinted with permission,
Se-Chul Park, Jun Fang, Shantonu Biswas, Mahsa Mozafari, Thomas Stauden, and Heiko O. Jacobs, "Approaching Roll-to-Roll Fluidic Self-assembly: Relevant Parameters, Machine Design, and Applications," Journal of Microelectromechanical systems, (*In Press*)

Copyright (2015) IEEE

4.1 Summary

This paper presents the implementation of an automated roll-to-roll fluidic self-assembly system based on surface tension driven self-assembly with applications in the field of macroelectronics. The reported system incorporates automated agitation, web motion, component dispensing, and recycling. The process enables the assembly and electrical connection of semiconductor dies/chips in a continuous and parallel fashion over wide area substrates. At present the method achieves an assembly rate of 15,000 chips per hour and an assembly yield exceeding 99%. The identification and modeling of the relationship between process parameters and forces on one side and assembly rates, detachment rates, error rates, and yield on the other is discussed as it lead to the discovery of the reported design. As an application we demonstrate the realization of a solid state lighting module. This particular application requires the assembly of a conductive multilayer sandwich structure which is achieved by combining the introduced assembly process with a novel lamination step.

Index Terms: roll-to-roll, fluidic self-assembly, flexible electronics, solid state lighting.

4.2 Introduction

The field of macroelectronics requires the integration of functional semiconductors over large area substrates in flat panel screens, large-area lighting modules, or solar panels. While the traditional microelectronics research has focused on a

higher functional density and single crystal Si, the main drive for macroelectronics research has been the integration of functional materials and devices over large, flexible substrates with higher cost efficiency.

Utilized methods range from serial direct write (inkjet like) techniques and screen printing methods for organic semiconductors and hybrid organic/inorganic structure to parallel transfer [7-10] and self-assembly techniques [11-13, 18, 19] for inorganic materials and devices. Previous demonstrations utilizing parallel transfer [7-10] and self-assembly techniques [11-13, 18, 19, 44] include flexible [22] and cylindrical displays [12], curved focal plane arrays [9], oscillators [7], RF ID tags [23], and PV modules [10] using materials such as ZnO [24], GaAs [13, 25], InP [26], GaN [14, 27], and Si [7, 9, 12, 28, 29]. In contrast to parallel transfer where functional devices are transferred from a donor wafer to a target substrate maintaining orientation and functional density, self-assembly is advantageous as it redistributes microscopic devices over large areas and order randomly distributed chips. For example, a binned container full of semiconductor dies/chiplets of a certain type and quality can be redistributed and assembled at precise locations on a substrate at any desired pitch or desired functional density using directed self-assembly. Despite of this advantage, there are only two methods available with a yield of 100%. While both methods are based on gravity, one uses shape recognition to assemble trapezoidal Si chips onto planar substrates [11, 74, 96] and the other uses surface tension driven self-assembly either using hydrophobic adhesive [44, 79, 84] or solder [12-15, 18, 97]. In our previous work, we first demonstrated an automated roll-to-

roll self-assembly platform, scalable to any desired level, for assembling and electrically connecting semiconductor components in a continuous fashion [103].

In this report, we demonstrate a theoretical model for optimizing the relationship between the relevant forces and other operational parameters, and experimentally verify the evaluated results at various chip sizes. In our modeling, we utilize fluid dynamics and various effects of the web angle and agitation on assembly- and detachment rates. Our system achieves an assembly rate of ~15,000 chips per hour using a 2.5 cm wide web. This enables us to assemble square shaped chips, 300 - 1000 μm in size. Under optimized conditions, an assembly yield of 99.8% is achieved. In addition, we use a novel lamination approach in the realization of flexible solid state lighting modules incorporating distributed inorganic light emitting diodes (LEDs) using the assembly system. Since this application requires not only self-assembly, but also the formation of multilayer interconnects, the lamination approach is crucial.

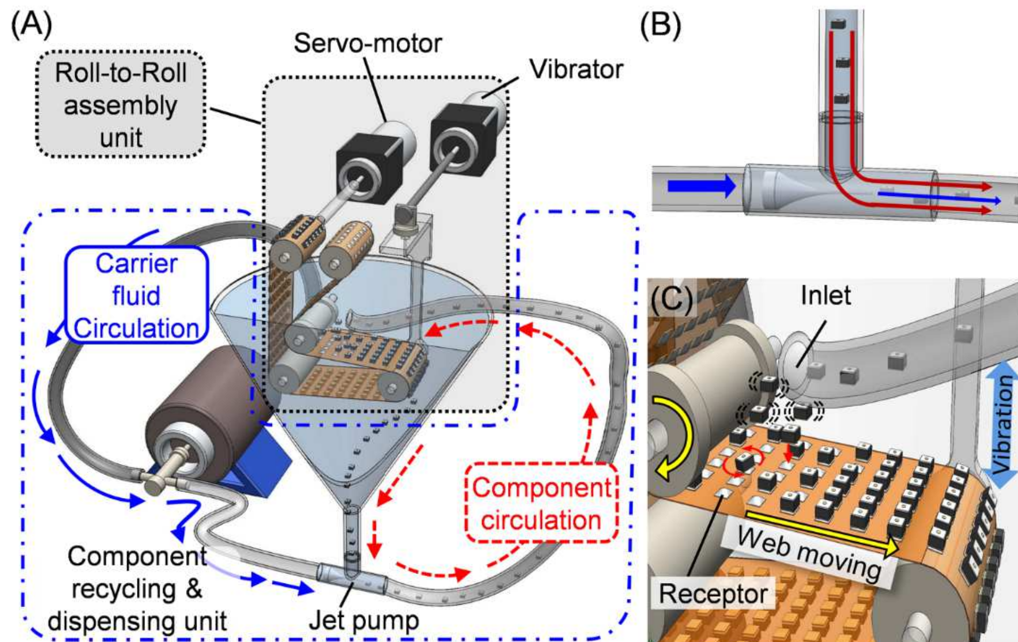

Figure 4-1. Automated Roll-to-Roll fluidic self-assembly process. (A) Overview illustrating component dispensing, fluidic self-assembly based on surface tension, and recycling of excess components. (B) Principle of jet pump. (C) Illustration of surface-tension driven self-assembly using molten-solder-based-receptor.

4.3 Results and Discussion

4.3.1 Self-Assembly Process and Layout of Testing Platform

Figure 4-1 illustrates the layout of automated roll-to-roll fluidic self-assembly system. The system contains two units:

(i) Roll-to-roll assembly unit (shaded in gray) involving motor, rollers, customized agitator, and polyimide web to regulate operation parameters such as web moving speed, web angle, agitation frequency and amplitude.

(ii) Component recycling and dispensing unit (shaded in blue) containing diaphragm pump, jet pump and dispensing nozzle to reintroduce and gently

dispense unassembled components.

The system operation includes four steps:

(i) transporting the components to the assembly unit; a jet pump delivers the unassembled components upward into a narrow fluid channel (5 mm inner diameter tubing). Originally we installed a mechanical pump between the bottom of the chamber and the dispensing head to circulate the components, however, this lead to mechanical damage to the components and the pump. To prevent this damage, we use an indirect circulation approach coupling a mechanical pump (QV variable speed pump, Fluid metering, Inc., NY) with the customized jet pump as shown in Figure 4-1(B). The jet pump requires a smaller diameter nozzle (1.48 mm^2) to accelerate the carrier fluid into a desired direction. Typical velocity of carrier fluid in the upward fluid channel (20 mm^2 tubing) is 25 cm/s to lift up the dense silicon components (density of 2.33 g/cm) to the dispensing head.

(ii) dispensing the transported components on the substrate; the components are dispensed on top of the substrate by gravity. Gentle introduction of components to the receptor is important to reduce the effect of liquid flow which induces additional drag. The dispensing head is located 5 cm away from the polyimide web (50 μm thick, 5 cm wide) pointing not directly at the web. Since the components leave the narrow dispensing head and meet large volume of liquid, the velocity decreases and the components fall downward following a vertical path to the web by gravity.

(iii) assembling the components on the substrate; the dispensed components are self-

assembled on the advancing substrate. Figure 4-1(C) shows the detailed attachment process. The substrates contain multiple pre-defined solder-coated receptors which are formed using a customized dip-coating of a low melting point solder on copper clad polyimide (50 μm thick, Pyralux® LF series, DuPont, NC) films patterned using a microfabrication technique. Procedure to fabricate the substrate is described in the experimental section. The self-assembly process is accomplished in water at 80 °C where the solder (Indalloy #117, MP. 47 °C, Indium Corp., NY) is molten. An immersion heater is used to maintain constant temperature. The surface of the molten solder based receptor wets the gold contact of the component and the component is assembled on a stable, aligned, and electrically connected position. This assembly process is powered by minimization of the free surface area of the molten solder (400 mJ/m^2 in water). Successful self-assembly process requires removal of metal oxides from the surface of the molten solder since metal oxides impede the wetting of metal contact with the solder. This removal is accomplished by adding a few drops of hydrochloric acid to the water (pH 2.0). A web moving velocity with single dispensing head is currently 10 m/hour. As the components reach at the angled web, a uniform distribution of components is required. The described process is predominantly based on gravitational sedimentation resulting sliding and tumbling of components on the angled web. In addition, the customized vibrator can agitate the web at controlled vibration conditions through up-and-down motion of the lower roller. This additional agitation helps the distribution of the

components over the web and the removal of excess components at the web turning point. The operation parameters such as the angle of web, vibration amplitude and frequency will be discussed in the results section.

(iv) collecting and recycling the unassembled components; the excess components drop down to the bottom of the chamber by gravity and are collected the T-section of the jet pump. After this point, the excess components are transported upward again and previous steps are repeated.

4.3.2 Assembly Results using Optimized Process

Figure 4-2 describes self-assembly results of various component sizes and receptor layouts including regular array and arbitrary patterns. We would test if (i) variations in size of the components would increase the number of defects and/or (ii) the position of the receptors on the substrate would affect the number of defects. Under optimal condition (will be discussed later), the defects were generally independent of the receptor position and component size. For example, Figure 4-2(A) depicts 570 receptors holding a single Si component where 4 misaligned components were found decreasing the yield to 99.3%; the misalignment was originated from a fabrication defect in the solder bump height, limited by manual dip-coating process not by the assembly system. Figure 4-2(B) shows assembly results using arbitrary patterns which maintain the same periodicity of regular array with lower area density (42.0%, 43.9% of parts per area in (A)). There was no tendency which would indicate that the process prefers regular pattern in terms of yield.

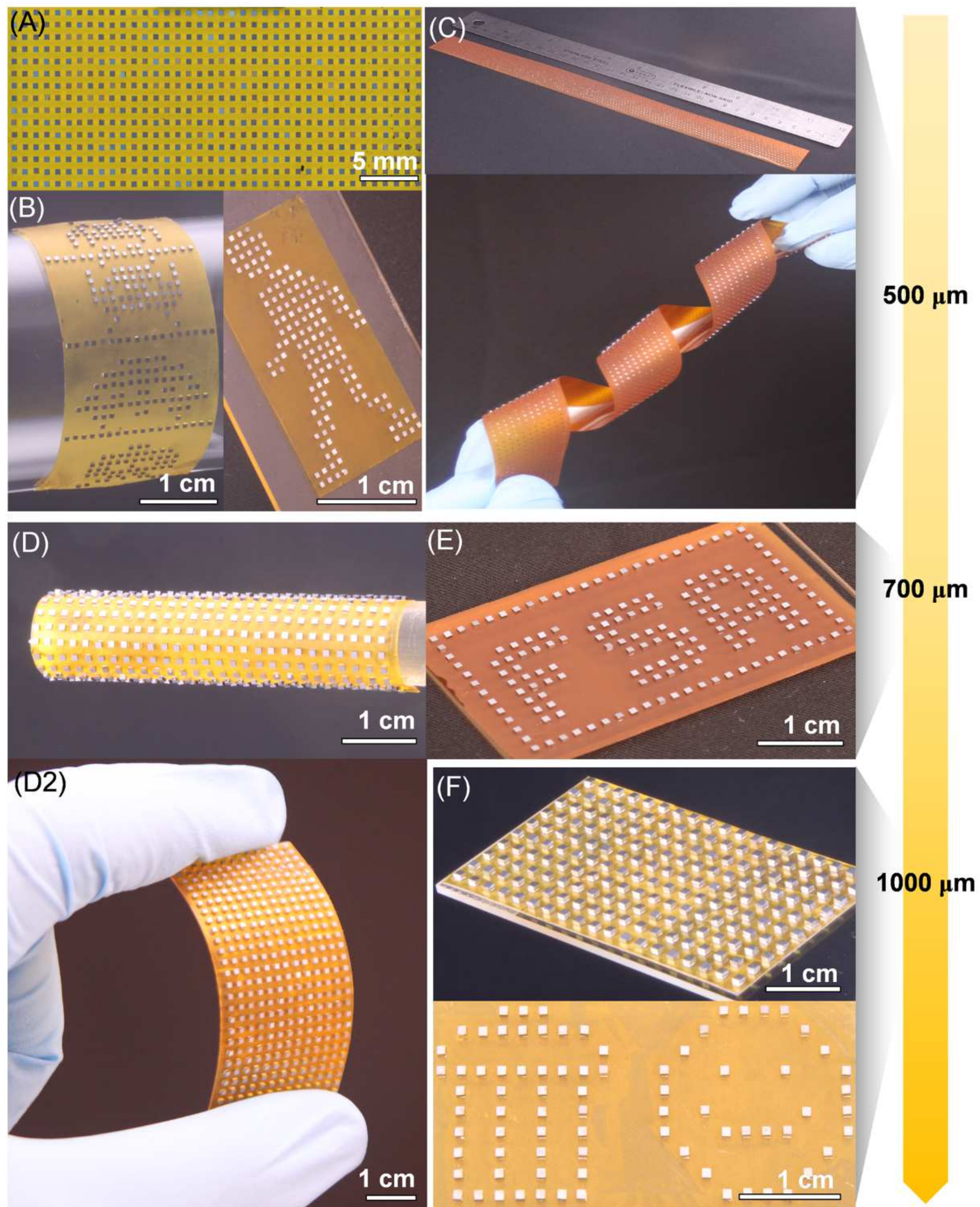

Figure 4-2. Photographs showing assembly results of various sized Si components. Small (500 μm) components assemblies testing (A) periodic 1.1 mm pitched, (B) arbitrary, and (C) continuous assembly on 2 cm wide substrates (a 29 cm long section is shown). Mid-sized (700 μm) chip assemblies testing (D) periodic 1.7 mm pitched, and (E) arbitrary assemblies. Large (1000 μm) chip assemblies testing (F) periodic 2.4 mm pitched and (G) arbitrary assemblies.

Figure 4-2(C) depicts assembly results on a 29 cm x 2 cm substrate with 1523 Si components assembled in 6 min. We found 1 missing and 3 misaligned defects in this sample which reduce the yield to 99.7%. The defect positions were randomly distributed across the substrate which shows that a single nozzle can effectively spread the components over a 2 cm wide assembly area.

The use of the nozzle in combination with a tilted plane has the advantage that it can minimize shear forces when compared to prior designs [12, 21]; previously a sliding slurry of excess components inside a rotating barrel was used as a delivery mechanism; a heavy sliding slurry has the disadvantage that it can remove already assembled components leading to a deterioration of the yield. Previously such a drop in yield was observed for large (>500 μm) components as they became too heavy when compared to the restoring force of the solder connection which scales with the area of the contact pad. This is less of a challenge in the current design since we can adjust the tilt angle and the amount of excess components independently. Figure 4-2(D)-(F) depict assemblies of larger chips with a side length of 700 μm and 1000 μm and chip thickness of 350 μm and 550 μm, respectively, representing a factor of 3.5 and 10 in terms of weight when compared to the Si chips with a side length of 500 μm. Figure 4-2(D) depicts 351 chips with a side length of 700 μm; no missing or excess components were found. Figure 4-2(F) depicts 190 chips with a side length of 1000 μm; no missing or excess components but 1 misalignment was found reducing the yield to 99.5 %. Assemblies in Figure 4-2(E) and Figure 4-2(G) had no defects. For reasons explained at the beginning of this paragraph it was previously [12, 21] not possible to assemble such a wide range of chip

sizes. The range is presently increased by a factor of 10 in terms of weight (relevant parameter) of the chips. Further extensions of this range should be possible but we are presently limited to chips with a side length of 300 - 1000 μm; smaller chips would require a higher resolution patterning methods to fabricate the solder bumps then presently used; larger chips have been tested but obstruction in the dispensing head would require a new design.

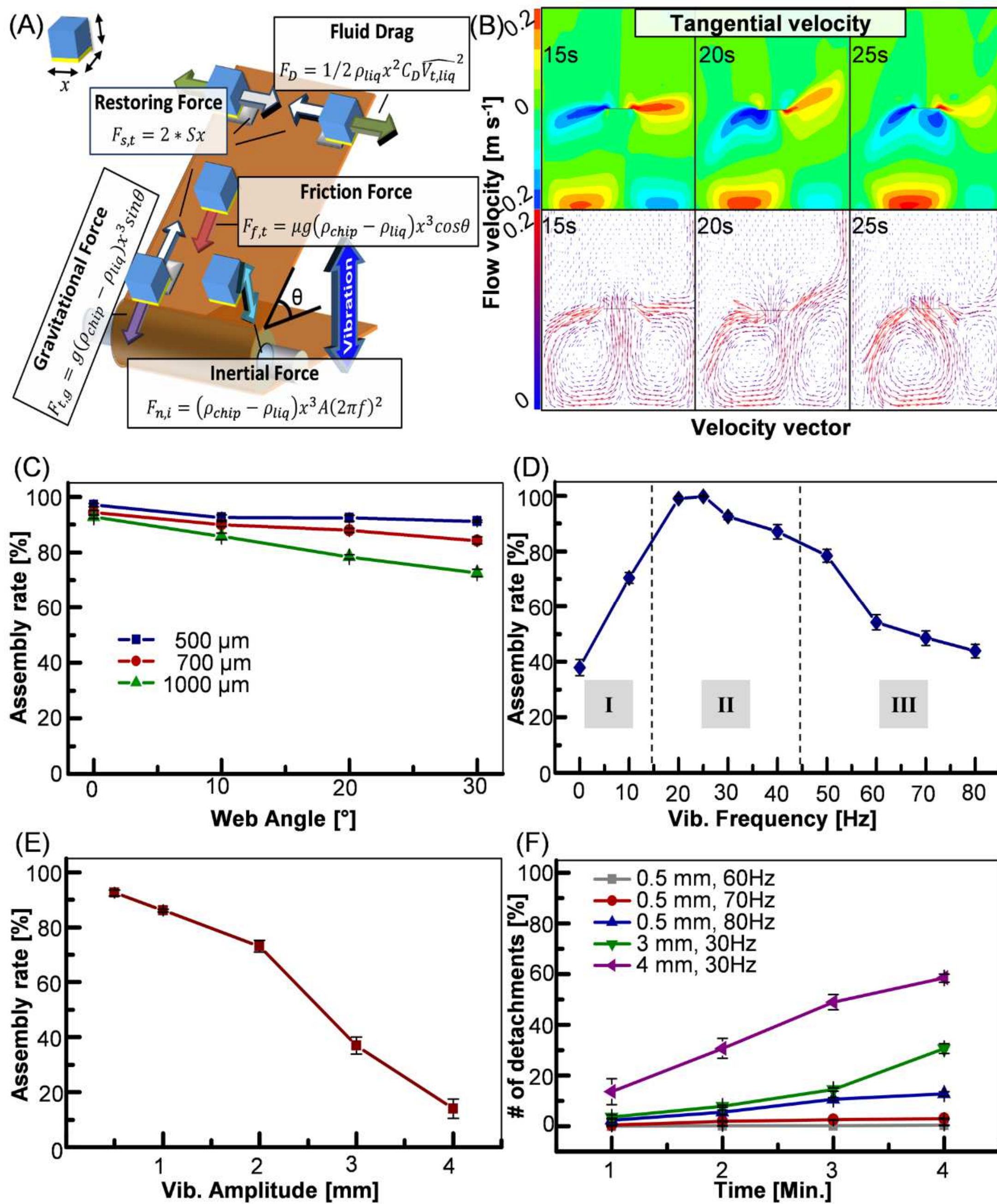

Figure 4-3. Comparison of the relevant forces, fluid dynamics computation, and experimental validation. (A) Relevant forces including restoring force, gravity, non-specific adhesion, inertial and fluid drag; the inertial and fluid drag are a result of agitation. (B) Calculated fluid velocity profiles induced by a harmonic up-and-down motion of a 5 cm wide web. Experimental validation and optimization testing the (C) assembly rate as a function of web angles, (D) assembly rate as a function of vibration frequency, (E) assembly rate as function of vibrational amplitude, and (F) detachment rate under excessive vibration as a function of time.

4.3.3 Relevant Forces Governing the Self-assembly Process and Optimization

The results described in previous figure (Figure 4-2) were obtained by careful optimization of the entire system looking at relevant aspects including component delivery to the web, component distribution, component assembly, and removal of excess components. The most relevant part of the optimization scheme is summarized in Figure 4-3. The first part (A - B) discusses the relevant forces. The second part provides an experimental validation (C - F) and looks at the number of assembled chips in a constant time interval (referred to as assembly rate) as a function of various assembly conditions as well as the detachment rate under conditions that are not favorable to providing an insight into the details of the process.

Figure 4-3(A) presents the relevant force elements, specifically:

(i) The Surface-tension-based-restoring-force ($F_{s,t}$) of a molten solder interconnect which can be calculated using

$$F_{s,t} = 2 * Sx. \qquad (4\text{-}1)$$

The equation is valid if the misalignment of assembled component in the tangential direction is large compared to the solder thickness [99]. For example, the restoring force in tangential direction is approximately 400 μN considering a 0.5 mm Si cube and 400 mN/m surface tension (S) of the solder; the component in the figures are under assumption that a gravitational force or drag force cause misalignment of components; actual misalignments are much smaller than what is illustrated.

(ii) The tangential gravitational force (

$$F_{t,g} = g(\rho_{chip} - \rho_{liq})x^3 \sin\theta \quad (4\text{-}2)$$

, roughly 1.7μN*sinθ for a 0.5 mm Si cube) on the angled web (θ) is at least a factor of 230 smaller than the surface tension based restoring force which is also the reason why already assembled chips remain attached to the solder bumps in the upside down oriented web. However, unfavorable conditions can be used to test the effect of gravity. For example, it is possible to load the web with a large number of excess components exceeding a single layer, under conditions of a high tilt angle, to cause a "sliding slurry" and shear forces to push assembled chips out of alignment up to a point where detachment is reached. While these effects can be reached they are not present in cases where less than a single layer of components is introduced and where the tilt angle is reduced to prevent unidirectional sliding of closely packed excess chips.

(iii) Non-specific adhesion ($F_{nonspecific\ adhesion}$) of the Si chips on the polyimide web is related since it influences the distribution of the chips. If no web vibration is used, high tilt angles are required to cause component sliding. Specifically, we observed that previously static Si cubes only begin to slide along the polyimide web at an approximate tilt angle of 48° increasing to a full sliding motion of all chips at a tilt angle of 60°. The required critical angle, where the gravity based force on the component is sufficiently strong to cause sliding of previously static chips, is important since it can be used to calculate the non-specific adhesive forces,

$$F_{nonspecific\ adhesion} = g(\rho_{chip} - \rho_{liq})x^3 \sin\theta_{crit} \tag{4-3}$$

, yielding 1.5 μN. Once in motion chips continue to slide. Under vibration, discussed later, unidirectional sliding can be observed at tilt angles down to 10°. In other words vibration can be used to achieve a slow and uniform sliding motion of the chips on the polyimide surface. For example, at a tilt angle of 10° the tangential force due to gravity is only 0.3 μN. Yet this force is sufficient to observe slow uniform downward sliding motion of 3 to 5 mm/s on an otherwise stationary web. At this speed and considering a 1 mm pitched receptor array it takes about 300 ms for an unassembled chip to reach a nearest neighbor. The sliding motion is also important considering the "residence time" which is defined as the time for a chip to be in partial contact with a 500 μm wide solder bump. The residence time is about 170 ms considering a sliding motion of 3 mm/s. A sufficiently long "residence time" is required for solder wetting to take place. Solder wetting leads to the final attachment of the chip.

(iv) The inertial force originated from the vibration of web with amplitude (A) and frequency (f) can be calculated using

$$F_{n,i} = (\rho_{chip} - \rho_{liq})x^3 A\ (2\pi f)^2. \tag{4-4}$$

This equation is valid when the chips contact with the web. A chip remains in contact with the web, for example, because of a solder connection (strongest, 400 μN), non-specific-adhesion (a few 1 μN), and gravitational force (1.7μN*cosθ). However, if the vibration frequency or amplitude exceeds critical values, separation and hopping will occur. For example, 3.0 μN (larger than gravity acting on a 0.5 mm Si cube)

would be reached using 0.5 mm amplitude, 30Hz oscillation which is experimentally feasible. As mentioned previously, the web oscillation causes a significant difference in the sliding behavior. Chips slide down even at a very low tilt angle down to 10° which can now be understood since the inertial force is sufficiently strong to overcome non-specific adhesion (estimated 1.5 μN) and gravity. At the same time this mechanism is not likely to reach a value to cause chips to detach from a solder bump; 400 μN (adhesion to a solder bump) would require us to maintain 7 cm vibration amplitude at 30Hz which is experimentally not feasible using a polyimide web immersed in water even at a high web tension due to an insufficient mechanical stiffness of the arrangement.

(v) The oscillating fluid drag force is a secondary effect that may have to be considered. The origin is also the vertical vibrational motion of the web. In general terms fluid drag is an effective form of agitation since it can be tuned over a wide range of amplitudes reaching values to move previously static chips on the polyimide surface around or to even exceed the surface tension based restoring force of an already assembled chip on the solder bump which would lead to component detachment. For example, a 0.5 mm cube exposed to a relative fluid velocity of 1.6 m/s will experience 400 μN drag force, calculated using

$$F_D = 0.5\rho_{liq} x^2 C_D V^2 \tag{4-5}$$

, with C_D = 1.27 and ρ_{liq} = 971 kg/m at 80 °C; the quadratic drag equation [100] is used rather than Stoke's drag because the calculated Reynolds number is larger than

100 regarding the experimental condition). Such a high drag force would lead to the detachment of a previously assembled chip; this is not desired but the detachment under high drag can be validated experimentally (discussed later in Figure 4-3(F)). Consequently a much lower value is typically chosen to obtain high yield assemblies; at an optimized value for the liquid flow of 100 mm/s the shear force reaches 1.3 μN (calculated using $F_D = 0.5\rho_{liq}x^2C_DV^2$, with C_D = 1, Re = 153). A shear force value of 1.3 μN is 300 times smaller than the 400 μN restoring force of the liquid solder joint providing a sufficient safety margin to prevent component detachment. Yet such a small force is sufficient to move chips around on the surface, and it is again on the same order of magnitude than non-specific adhesion estimate (1.5 μN). Unfortunately, the liquid flow and subsequent drag force cannot be assumed constant across the surface of the oscillation web and a more precise understanding requires a somewhat complex computational fluid dynamics (CFD) analysis (Ansys CFX).

Figure 4-3(B) shows calculated fluid velocity profiles surrounding an infinitely long 5 cm wide oscillating plate excited using an optimized vibration condition used in the experiments (amplitude 0.5 mm, frequency 30Hz). The first profile (left) represent a liquid motion which is close to a published time independent flow profile surrounding an infinitely large extended plane [104]. However, our web has a finite width and is in oscillatory motion; consequently a direct comparison to a time independent study cannot be justified. As a consequence a variable moving finite element mesh method is used to determine if there are changes in the liquid velocity profile over time. Boundary layers and dimensions are identical to the experimental conditions with the exception that the

web and container was assumed to be infinitely long to reduce the problem to a 2D computation.

The provided URL[1] links to a video which shows the progression of the liquid flow over a period of 26 s. Three frames are shown in the Figure 4-3(B). First, the normal component of the liquid velocity on the surface of the web reaches the 100 mm/s peak value matching the speed of the oscillating web ($A*2\pi f$) which it should. Second, a tangential 30Hz oscillation of the liquid layer is observed as expected since this matches the drive frequency. Third, the tangential velocity amplitude is not constant and enhanced towards the edge of the web being at a minimum in the center which can also be expected considering the symmetry.

Finally, and this is interesting, the observed flow profile is not constant over time periods exceeding a few seconds. Instead the formation of short lived vortices can be observed which go hand in hand with shifts of the flow profile leading to higher amplitude oscillations towards the center of the web. This is importance since it explains why the chips experience a left and right vibration even in the center of the web and not only towards the edge as originally thought.

A frame-by-frame analysis provides additional insights into typical values of the amplitude (and velocity) of the tangential liquid flow $(V_{t,liq})$ in our experiments. Towards the sides of the web (within 50% of the total area) the values are typically larger (up to a factor of 2) than the amplitude (and velocity) of the web driving the motion. For example,

[1] http://www.ece.umn.edu/~hjacobs/videos.html

the optimized 0.5 mm vertical 30Hz web oscillation (100 mm/s peak normal velocity) leads at times to a tangential liquid velocity amplitude of 200 mm/s. At 200 mm/s liquid velocity, a drag force of 4.7 μN would be present on a stationary chip (calculated using $F_D = 0.5\rho_{liq}x^2C_D\,\widehat{V_{t,liq}}^{\,2}$, with C_D = 1, Re = 306). In the center, half of the web, 100 mm/s is observed at times. At 100 mm/s liquid velocity, a drag force of 1.3 μN would be present. In both cases the forces are larger than the non-specific adhesion which explain why chips are never stationary in the experiments and do not simply slide down in a linear trajectory but vibrate left-and-right. At the same time the forces (< 5 μN) provides a sufficient safety margin to prevent detachment of already assembled chips which would require 400 μN. Moreover, a 30Hz oscillation with a peak tangential liquid velocity amplitude of $\widehat{V_{t,liq}}$ = 100 mm/s translates into a 1.2 mm back and forth tangential displacement of a liquid layer which in turn defines an envelope for chip movement to take place. In other words, the chips will follow this oscillating liquid movement with an amplitude smaller than the 1.2 mm envelope. Specifically, the chip motion needs to satisfy a nonlinear differential equation

$$0.5\,\rho_{liq}x^2C_D\left(\widehat{V_{t,liq}}\sin(2\pi ft) - v_{chip}\right)^2 = \rho_{chip}x^3\frac{d\,v_{chip}}{dt} \quad (4\text{-}6)$$

which describes the force balance between drag force and inertial force. A simple closed analytical solution for the displacement of the chips can only be given if we assume a step response whereby the liquid flows at a constant speed $\widehat{V_{t,liq}}/\sqrt{2}$ for a period of time $1/(2f)$ before it changes direction. Under this assumption the vibrational amplitude reduces to

$$\Delta X_{chip} = \frac{\widehat{V_{t,liq}}}{f\sqrt{8}} - \quad k * \ln\left(1 + \frac{\widehat{V_{t,liq}}}{kf\sqrt{8}}\right) \tag{4-7}$$

, with $k = \frac{2x\,\rho_{Chip}}{c_D \rho_{liq}}$ and ΔX_{chip} becomes 230 µm using $\widehat{V_{t,liq}}$ = 100 mm/s, f = 30Hz, x = 500 µm chip size.

To summarize the previous two paragraphs, the input for the calculation was the vibration frequency and amplitude. A 0.5 mm, 30Hz vertical web oscillation will cause localized tangential liquid velocity of approximately 100 mm/s, which in turn leads to a subsequent drag force of 1.3 µN and periodic chip displacement of approximately 230 µm in case of a 500 µm sized chip; these values represent physical parameters that work well experimentally (discussed later). Higher vibrational amplitudes lead to higher velocities, tangential forces, and localized displacements; for example a 4 mm, 30 Hz oscillation increases the values to 750 mm/s, 80 µN, and 5.3 mm, respectively, which represents a condition far away from the optimum both in terms of capture rate and component detachment rate (validated in Figure 4-3(D)&(E), discussed later).

Table 4-1 provides a summary of the relevant forces, their range, and use. The understanding of the various scaling laws was essential in the design and optimization of the self-assembly platform. The values with a green background represent optimized conditions for chips with a side length of 500 µm to provide assembly yields exceeding 99%.

In order to study and validate the calculated dependencies several experiments have been performed:

Table 4-1. Summary of the forces, their range, and use.

Tangential Grav. Force $F_{t,g} = g(\rho_{chip} - \rho_{liq})x^2 \sin\theta$	**Inertial Force** $F_{n,i} = (\rho_{chi} - \rho_{liq})x^2 A\,(2\pi f)^2$	**Fluid Drag Force** $F_d = 0.5\rho_{liq} x^2 C_D V^2$	**Surface Tension** $F_{s,t} = 2 * Sx$
0.3 µN tangential gravitational force is reached at θ = 10° web tilt; chips slide down with 3 mm/ s under dynamic agitation which leads to a sufficiently long solder contact residence time of 170 ms	**3.0 µN** normal inertial force (1.6G acceleration) is reached at 0.5 mm, 30Hz web vibration; this exceeds slightly the gravitational force causing a gentle lift/hopping motion and overcoming non-specific adhesion of previously static chips.	**1.3 µN** fluid drag force is reached at a relative liquid velocity of V = 100 mm/s caused by a 0.5 mm, 30Hz web vibration. This drag force is sufficient to overcome non-specific adhesion of previously static chips and to cause a 230 µm, 30Hz chip vibration.	
1.5 µN tangential gravitational force is reached at θ **= 60**° web tilt which exceeds non-specific adhesion of static chips; chips slide down with 40 mm/s; solder contact residence time is 12.5 ms which is too short to capture chips effectively.	**24 µN** inertial force (14G acceleration) is reached at 4 mm, 30Hz web vibration causing a significant lift/hopping motion ➔ capture rate and speed of the self-assembly process is reduced as a result.	**80 µN** liquid drag force is reached at a relative liquid velocity of V = 750 mm/s caused by a 4 mm 30Hz web vibration. This value is reaching a level where detachment events of previously assembled chips can be recorded.	**400 µN** used to capture x = 500 µm sized chips
1.7 µN gravitational force is reached at θ = 90°. Chips drop down with 100 mm/s and are not captured.	**400 µN** inertial force (235G acceleration) requires 7 cm 30Hz web vibration; this would* detach all assembled chips at once.	**400 µN** liquid drag force is reached at a liquid velocity of V = 1.6 m/s; this would* detach all assembled chips at once.	

* not yet tested due to an insufficient mechanical stiffness of the arrangement.

First, we evaluated the effect of gravity on the assembly rate (Figure 4-3(C)) testing various inclined angles and three chip sizes with different weights (0.117 mg, 0.4 mg, 1.1 mg). In each experiment (5 experiments per data point) we tracked the number of assembled components for a fixed time of 3 minutes using a constant vibration (0.5 mm amplitude and 30Hz frequency). A described value of 98% indicates that 98% of the receptors carried a single component within 3 minutes while 2% of the receptors were unfilled. The effect of gravity is not very strong but cannot be neglected at the scale discussed here. In analogy to the previous section points (ii) and (iii), the reason why the capture rate shows a slight reduction using the heavier chips is due to a faster sliding motion and shorter residence time on the solder bumps particular towards higher tilt

angles. As an example at a tilt of 30° the sliding speeds (determined by recording and analyzing the relative motion of the chips using a video camera) were 3 mm/s, 8 mm/s, and 14 mm/s for the 500, 700, 1000 μm sized chips, respectively. Chip detachment of previously assembled chips was not observed which agrees with the theory (previous section point (ii)) that gravitational shear forces are not strong enough to cause detachment.

Second, we examined the influence of vibration frequency (0 - 80Hz) (Figure 4-3D) in consecutive experiments (5 experiments per data point) maintaining a fixed vibration amplitude (0.5 mm) and web angle (10°). Three operational windows can be defined that exhibit different assembly rates which can be explained as follows: (1) Slow vibration (0 - 10Hz, 0.5 mm, 10°) — in this region the advancement of self-assembly was slow and unsteady. In analogy to the previous section point (iii) some components did not show active movement due to the insufficient agitation; in this region, non-specific adhesion and gravity are dominant than inertial and drag force. Moreover, the poor distribution of component caused the assembly only on the center of the web. (2) Optimal assembly window (20 - 40Hz, 0.5 mm, 10°) — under this condition, the advancement of the self-assembly is optimized, components spread uniformly across the web and are not too fast for the self-assembly to take place; across the entire web a slow unidirectional sliding motion of the components is observed at about 3 mm/s; this velocity translates into a "residence" time of 170 ms considering a 500 μm sized solder bump. At 30Hz, 200 - 300 μm lateral chip vibration is observed which is caused by the oscillating shear flow of the liquid which is in close agreement with the theory (previous section point (v),

predicting a chip displacement of 230 μm). (3) High vibration (50 - 80Hz, 0.5 mm, 10°) — In this regime, chips slide over the receptors but do not get captured by the solder bump as effectively as the slower moving chips. Some detachment is likely present but will be studied separately below.

Third, we evaluated the effect of vibration amplitude (0.5 - 4 mm) (Figure 4-3(E)) in consecutive experiments (5 experiments per data point) maintaining a fixed frequency (30Hz) and tilt angle (10°). The first data point represents the optimal condition of the previous set of experiments where excellent spreading was obtained. An increase in amplitudes beyond the optimal value reduces the assembly rate. This trend can again be explained by components that begin to move too rapidly for capturing to take place (in analogy to the previous section points (ii) and (iii)). A second reason is that the liquid flow is increased to a point where the drag force causes the detachment of previously correctly assembled chips (in analogy to the previous section point (v)). Both effects should be present and a final experiment is required to confirm that a detachment condition can be reached.

The *final* set of experiments is used to test and confirm that component detachment can take place if the vibration is increased to a point where the liquid drag force becomes too large. The experiments start with previously perfectly assembled arrays containing 500 μm sized chips which are exposed to harsh vibration conditions without any excess chips inside the assembly system to a point where detachment can be observed. Figure 4-3(F) depicts the total number of detachment events as a function of exposure time to various, including harsh vibration/fluid drag conditions. The results

under harsh conditions are useful since they provide a deeper understanding as to why a drop in yield under high frequencies (Figure 4-3(D)) and high amplitude (Figure 4-3E) was recorded in the previous set of experiments. The conclusion is that the previously recorded drop in yield under adverse assembly conditions was actually due to a combination of a reduced capturing rate and increased detachment rate which both have a negative impact on the progression of the self-assembly process.

The understanding and optimization of all parameters lead to the defect free assemblies discussed at the beginning. We think that more research is needed to understand the ultimate level of assembly speed and throughput that can be achieved which has not yet been the focus of the research. In addition, there are questions of the reliability of the electrical interconnects which need to be addressed going forward. However, the goal was to demonstrate that functional assemblies is feasible and that the self-assembly process reach the performance of serial robotic assembly. This goal has been achieved and we believe that our process can be adapted to various applications. For example, a field where assembly of functional microelectronics with high throughput is required would be particularly interesting application. One example is presented below.

4.3.4 Production of Flexible Solid State Lighting Modules

Figure 4-4 shows the assembly of GaN LEDs which can be applied to produce other solid state lighting modules in a cost efficient manner. We used 115 μm tall and 300 μm x 300 μm thin GaN LEDs (XT290, Cree). Figure 4-4(A) shows the process flow to fabricate the flexible solid state lighting modules: (i) Preparation of electrically

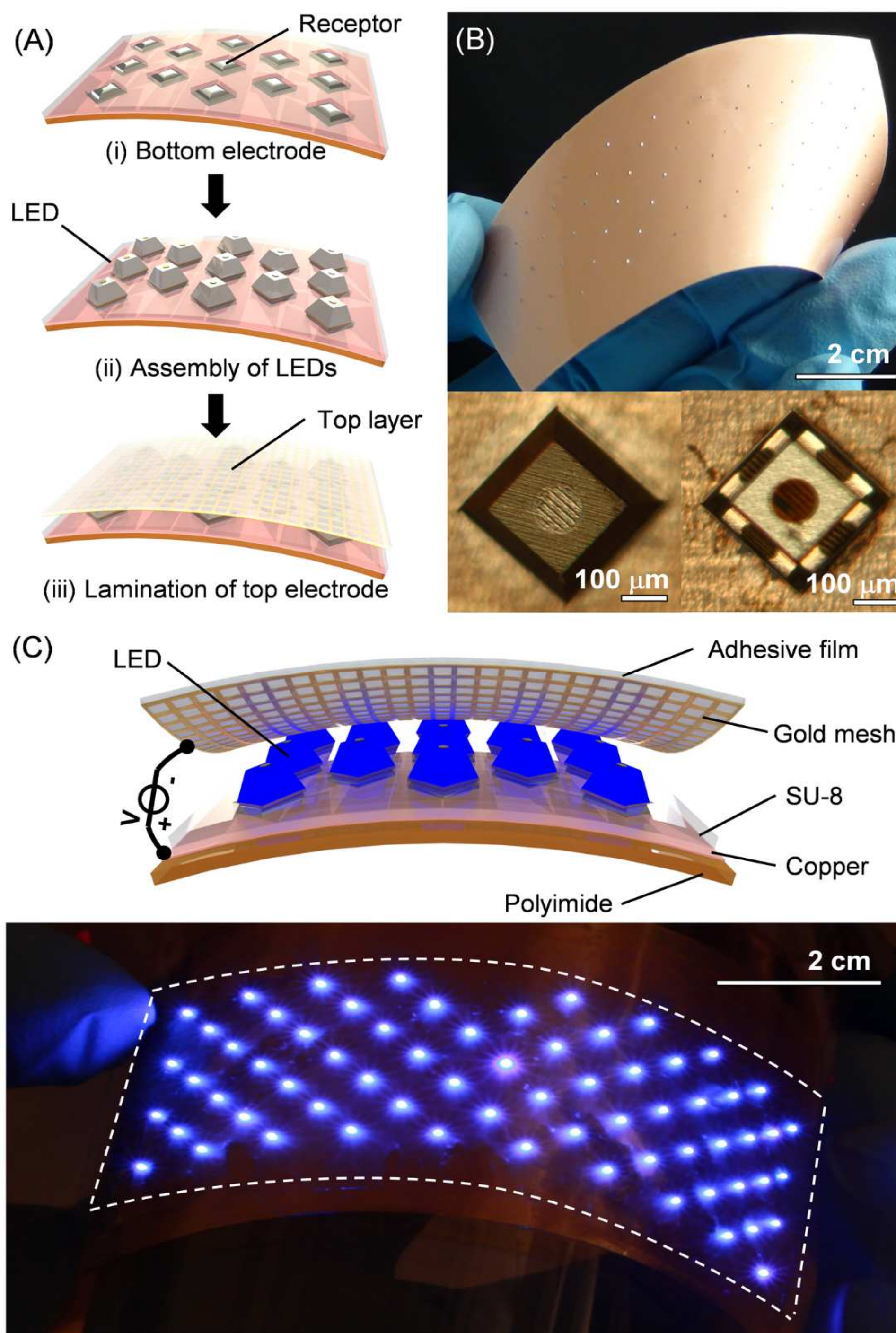

Figure 4-4. Flexible solid state lighting modules realized by the roll-to-roll fluidic self-assembly platform. (A) Fabrication steps: (i) Preparation of electrically isolated flexible bottom electrode with receptors, (ii) assembly of LED using the roll-to-roll fluidic self-assembly system, and (iii) lamination of top conductive film. (B) Photograph of assembled LEDs on flexible bottom electrode, close-ups of LEDs: with an anti-solder wetting layer to control right-side-up assembly (bottom, left), and after removing the anti-solder wetting layer (bottom, right). (C) Photograph of flexible solid state lighting modules.

isolated bottom electrode with receptors, (ii) assembly of LEDs on the bottom electrode using the FSA process, and (iii) lamination of top conductive film to finish the electrical connections.

First, a plain copper clad polyimide substrate (3.7 cm × 8 cm in total size, 2.3 cm × 7 cm in assembly region) was used as a support and common electrical contact to the LEDs. A spin coated 15 μm thick layer of epoxy based photoresist (SU-8 2010, MicroChem) is applied and patterned by lithography to define an array of openings to the copper for solder wetting and assembly to take place. Use of this polymer isolation layer eliminates additional electrical isolation steps and enables direct lamination of top conductive layer after the assembly process. The process of wire-bonding is not required. The solder based receptors were formed using the same dip-coating method described before.

Second, the LEDs (Figure 4-4(B), top) need to be modified to ensure that the chips assemble with the correct (bottom side) contact on the substrate. This requires the application of a sacrificial 100 nm thick and sputter coated Ti anti-solder wetting layer onto the top face of the LEDs. Solder does not wet the Ti coating which ensures that the chips assemble with the correct orientation on the substrate. The Ti coating of correctly assembled LEDs is removed using a 45 second long wet chemical etch (Figure 4-(B), bottom right).

The *third* step is to laminate the top conductive film. The goal was to find an alternative electrical connecting method eliminating series wire-bonding which requires increasingly long processing time with an increase in the number of the components.

Forming a direct electrical contact without conventional microfabrication process has been demonstrated by locating a metal coated silicone rubber or transferring a metal layer onto the desired substrate [8, 9, 61, 101].

However, the adhesiveness of the original method based on Van-der-Waals force was not sufficient enough for certain applications. The alternative we chose has a composite structure, where parts of the surface are adhesive (and not conductive) while the rest are conductive (and less adhesive), to achieve sufficient electrical conductivity and adhesion. In the simplest form, we used a metal mesh (Figure 4-4(C)**,** top) enclosed by an adhesive surface; The Van-der-Waals adhesion between the conducting traces were sufficient to provide a small contact resistance while the surrounding adhesive stabilizes the mechanical contact between the two surfaces. To avoid misalignment, we designed a mesh periodicity which is smaller than the width of the contact pad on the top of the LEDs (100 μm in our design). For example, a 25 μm pitch ensures that at least 3 horizontal and 3 vertical lines cross the top contact of the LED providing a 3 × 3 redundancy.

To test this new contact method, we fabricated a 4 cm × 7 cm gold mesh using microfabrication and transfer to a clear adhesive tape (3M Scotch tape, 3M). The composite of fabricated conducting and adhesive portions is then attached to connect the top of the LEDs. Figure 4-4(C) (bottom) illustrates operation of a lighting module that consists of 67 LEDs contacted using this method. Most LEDs lit up (~ 99%). One defect was found where no contact was made.

4.4 Conclusion

Herein we report the optimization of a roll-to-roll fluidic self-assembly system to assemble functional semiconductor components. Under optimized operation the system is able to assemble and electrically connect 300 - 1000 μm square components with yields approaching 100%. The optimization required a theoretical analysis and experimental validation of the relevant parameters (forces that act on the components, component transport and dispersion, and fluid dynamics calculations). The gained knowledge leads to the defect free assemblies. The system can be improved further using shape recognition to achieve contact pad registration and unique orientation [15, 18, 19] or using sequential batch assembly to integrate more than one type of components [13, 78]. Moreover, it is possible to transfer assembled chips onto other flexible or stretchable substrates. It should also be possible to extend this scheme towards smaller chip sizes in the future. Applications include flexible solid-state lighting module, large area flexible solar cell panel, and flexible energy harvesting module through integration and distribution of microscopic devices.

4.5 Experimental

4.5.1 Si components

To fabricate 500 μm in lateral size Si chips, 200 μm thick Si wafers (University Wafers, Boston, MA) that were cleaned with a Piranha solution (1 H_2SO_4 : 1 H_2O_2) at 120 °C for 15 min and rinsed with DI water. An e-beam evaporator was used to coat the wafer with 10 nm Cr and 200 nm Au layers. Photoresist (Microposit 1813, Shipley) was then spun on at 3,000 rpm for 30 sec. After a soft-baking, the substrate was exposed with

90 mJ/cm^2 UV light and developed in 1 Microposit 351 : 5 H_2O solution for 25 sec. The Au and Cr layers were subsequently defined using wet-chemical etching. The photoresist was stripped using acetone and a reactive ion etch (O_2, 100 sccm, 100 W, 100 mTorr). Finally, the wafer was diced using a wafer dicing saw. 700 μm and 1000 μm wide Si chips were prepared with the same conditions except the thickness of the wafers was 350 μm and 550 μm, respectively.

4.5.2 Self-assembly substrate

A copper clad polyimide is the starting material (Pyralux® LF series, DuPont, NC). The 20 μm thick Cu layer was cleaned with a 1 HCl : 10 DI water solution, DI water. Dry-film (Alpha 300, Megauk, UK) was applied on the top using a tension controlled laminator at 95 °C with 250 kPa, exposed with 55 mJ/cm^2 UV light through a transparency mask, and developed in 2% K_2CO_3 in room temperature for 50 sec. The exposed Cu was wet-chemically etched in a 30% $FeCl_3$ solution for 5 min. The dry-film was removed in a 4% KOH solution at 40 °C leaving Cu squares (receptors) on the substrates. The substrate was rinsed with DI water. Finally, a low melting point solder (Indalloy #117, MP. 47 °C, Indium Corp., NY) was applied on the Cu pads through dip coating in a preheated solder bath to fabricate the predefined receptors.

4.5.3 SSL application

4.5.3.1 Bottom electrode

The fabrication of the bottom electrode uses same copper clad polyimide and follows the cleaning procedure above. Following the cleaning step, epoxy based negative photoresist is used to prevent undesired wetting of solder and electrically isolate bottom electrode from top conductive layer. SU-8 2010 (MicroChem) was spin coated onto the substrate at 2,000 rpm for 30 sec. After pre-baking at 95 °C for 3 min, the substrate was exposed with 150 mJ/cm^2 UV light and post-exposure baked at 95 °C for 3 min. The substrate was then developed in propylene glycol methyl ether acetate (PGMEA). Finally, the receptor was formed by dip-coating the solder onto the exposed copper island.

4.5.3.2 Top Electrode Lamination Layer

Si wafers (University Wafers, Boston, MA) that were cleaned with a Piranha solution and rinsed with DI water. 250 nm Au was the applied using an e-beam evaporator without adhesion layer. Photoresist (Microposit 1813 Shipley) was applied (3,000 rpm), exposed, and developed in Microposit 351 : 5 H_2O solution (25 sec). The Au layer was wet-chemically etched, washed in isopropyl alcohol, and carefully dried. The patterned Au mesh was transferred onto a clear adhesive tape (3M scotch tape).

4.6 Acknowledgements

The research received financial support in part through grants from the National Science Foundation (NSF Grant DMI-1068013), German Science Foundation (DFG Grants JA 1023/3-1), and the Carl-Zeiss Foundation

CHAPTER V

5. Millimeter Thin and Rubber-Like Solid-State Lighting Modules Fabricated Using Roll-to-Roll Fluidic Self-Assembly and Lamination

Se-Chul Park[1], Jun Fang[1], Shantonu Biswas[2], Mahsa Mozafari[2], Thomas Stauden[2], and Heiko O. Jacobs[1,2,*]

1 University of Minnesota, Electrical and Computer Engineering, Rm. 4-178, 200 Union St. SE, Minneapolis, MN 55455, USA

2 Fachgebiet Nanotechnologie, Technische Universität Ilmenau, Gustav-Kirchhoff-Strasse 1, Ilmenau, D-98693, Germany

Reprinted with permission,
Se-Chul Park, Jun Fang, Shantonu Biswas, Mahsa Mozafari, Thomas Stauden, and Heiko O. Jacobs, "Millimeter Thin And Rubber-Like Solid-state Lighting Modules Fabricated Using Roll-to-Roll Fluidic Self-Assembly and Lamination," Advanced Materials, DOI: 10.1002/adma.201500839, (2015)

Copyright (2015) John Wiley & Sons, Inc.

5.1 Introduction

The field of stretchable electronics has seen a rapid increase in research activities in recent years. It enables new kinds of applications such as smart clothing [105], conformable photovoltaics [30], stretchable batteries [31, 32], artificial electronic skins [33, 34], or mechanically soft and conformable health monitoring devices [35, 36] to give a few recent examples. The realization typically requires integration of functional semiconductor materials on a low temperature stretchable polymeric rubber-like support which is in stark contrast to traditional semiconductor manufacturing which requires the use of high temperature processing and rigid semiconductor wafers. From a technical point of view a classification into two groups can be made: ***Class 1 - 'Polymeric substrate first'*** uses the low temperature polymeric substrates right at the outset of the processing sequence. Commonly direct-write techniques are subsequently used to deposit the required functional materials. This approach may provide certain advantages from a cost savings point of view; however, any subsequent processing step is limited in terms of processing temperature. Class 1 methods are often challenged when it comes to the performance of the devices and the complexity of the circuits or systems they can produce. While new materials [106, 107] including nanomaterials are sought to be the solution many of the challenges due to the low temperature processing requirements remain. For example, the field of printable electronics which applies electronic inks in the form of nanoparticles using direct-write inkjet-like printing methods has not yet achieved the breakthroughs since the high temperature processing and annealing steps required from a device point of view cannot be carried out [108-110]. ***Class 2 - 'Polymeric***

substrate last' refers to methods which delay the use of the low temperature substrate as long as possible. This class of methods shares the advantage that they can be combined with well-established semiconductor device technologies; the use of nanomaterials is not required. While this may look as a capitulation going back to the old and established method, it has been proven to be a very successful methodology. A pioneer in the field has been E. Menard and coworkers [111]. Today established semiconductor device technologies and segmentation (etching) methods are frequently used to produce microscopic functional device segments, which are subsequently transferred onto low temperature substrates. Various forms of stretchable semiconductor device layers and stretchable metallic interconnects have been reported. The first examples were based on semiconductor materials such as GaAs [30, 112], InGaN [113], and Si [112, 114, 115] which can be stretched and compressed (demonstrated 50%) if the thin film are transferred onto a polymeric substrate in a way to yield buckled 3D wave like topologies [116] similar to an accordion fold. The required fabrication of very thin device layers is perhaps a slight disadvantage.

However, it is also possible to use more rigid device elements. Here, segmented devices are distributed on rubber-like substrate and electrically connected using stretchable meander shaped metallic interconnects. This approach has been particularly successful and various new applications were demonstrated; conformable optoelectronic modules [117-119], stretchable sensor arrays [35], and rubber-like electrocardiographic electrode arrays [120] are some examples. In contrast with the first method, this methodology enables, in principle, direct use of commercial devices and circuit elements.

As mentioned class 2 methods require the assembly of the device layer or the application of interconnects towards the end of the processing sequence which can be challenging as well. Finalization of the functional system requires steps of assembly, alignment, transfer, contact pad registration, or electrical contact formation which are all challenging points. For example, it is difficult to form electrical interconnects between individual layers in subsequent transfer steps. As a results most of the reported structures complete the electrical interconnects directly on the wafer to eliminate this step. In other words transfer of the entire structure in a single step is often used. Moreover, the stretchable systems reported so far used semiconductor device elements which had all contacts on a single face to eliminate the realization of multilayer alignment; the arrangement presented here will use devices with top and bottom contact which is particular challenging from an interconnection point of view; a lamination step will be discussed to overcome this challenge. Another challenge involves limitations in the size of the stretchable systems which are currently limited to the size and layout of the donor wafer. Large-area integration and redistribution of the active devices is commonly not possible; transfer techniques use a donor substrate/wafer and maintain orientation and integration density.

This publication addresses this issue of assembly and redistribution. In the presented case we will use conventional binned dies on a carrier tape with a pitch and orientation specified by the manufacturer, which is different from the desired final arrangement. In other words redistribution is required and simple transfer is not possible. A process of directed self-assembly is used to achieve redistribution, alignment, and

registration. The process extends the range of applications to the utilization of commercially available segmented semiconductor chips instead of previously used specially designed donor wafers to transfer the parts. As a demonstrator we choose to fabricate a millimeter thin rubber-like solid-state-lighting-module incorporating distributed and electrically connected LEDs. Fabrication of this structure incorporates: (i) design and fabrication of the bottom electrode, (ii) assembly and electrical connection of the LEDs, and (iii) lamination of a conductive top layer. The bottom electrode is designed using a computation tool to realize *'stretch-tolerant',* a *'gradient`* and *'no-stretch-regions'*. The composite structure can be stretched to 220% of the original length while the assembly sites for the chips remain within a *'no-stretch-region'* which is more robust than other designs. The assembly of the chips is achieved using a roll-to-roll fluidic self-assembly platform [103] which is adapted to work with the soft and rubber-like material. To complete the electrical connections and to eliminate critical alignments a hybrid top conductive lamination layer will be presented. The laminate is composed of a conductive wire mesh (less adhesive) which is embedded in an adhesive (not conductive) matrix. The composite can tailor the electrical and adhesive properties independently and defect free lighting modules can be formed. The origin of defects. in the 1 mm thick structure under stress will be discussed.

5.2 Results and Discussion

Figure 5-1 provides an overview of the experimental strategy to fabricate mechanically flexible and foldable area lighting modules on the basis of solder directed fluidic self-assembly and lamination. Our goal was to establish a scalable process to

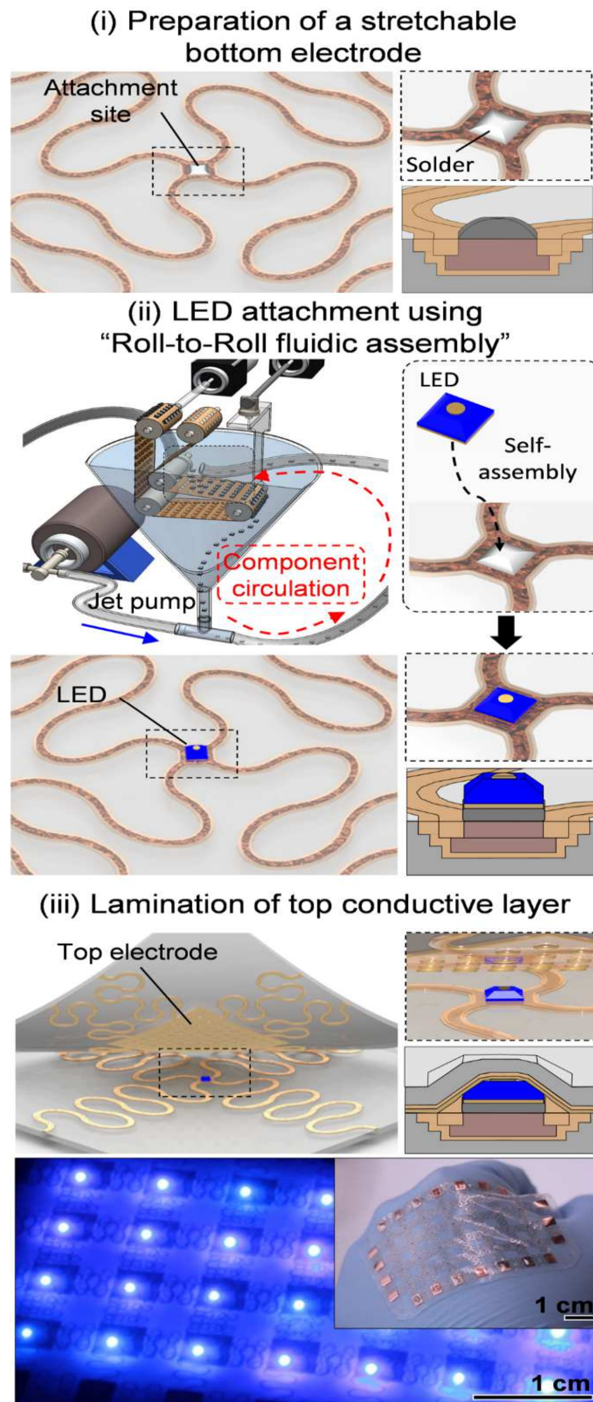

Figure 5-1. Overview of the three basic steps used to fabricate a rubber-like solid-state lighting module: (i) preparation of a stretchable bottom electrode with solder coated attachment site, (ii) the attachment of the LEDs using solder directed fluidic self-assembly, and (iii) the lamination of a stretchable top conductive layer.

fabricate such modules in a continuous roll-to-roll process. Moreover, the process is designed to be compatible with unpackaged commercially available LED chips. We used n-GaN/p-GaN thin LEDs with a side length of 300 μm and a height of 115 μm (XT290, Cree) as device segments in this study. The fabrication of the specific area lighting module requires the use of stretchable materials and interconnects to relieve the stress as the structure is bent. Overall the process is divided by the three required milestones to fabricate a functional unit. First, a sufficiently reliable bottom electrode with receptors that provides sufficient stretchability to relieve the stress has to be fabricated. Second, the attachment of the LEDs needs to be done over wide area substrates which is accomplished using a solder directed fluidic self-assembly [12, 13, 68, 103] instead of conventional robotic pick and place or wafer level transfer. Third the electrical connections need to be completed to operate the LED array. The third step was particular challenging; the use of wire-bonding had to be eliminated and it was required to develop a lamination step which applies a stretchable top conductive layer to the structure to complete the electrical connections (photograph, Figure 5-1 bottom) without any critical alignment. The required fabrication steps, technology, and present limitations will be described in the following sections.

5.2.1 Part 1: Preparation and characterization of the stretchable stress relieving rubber supported metal electrode.

The rubber-like bottom electrode has to satisfy a number of requirements: (i) it needs to be compatible with the fluidic self-assembly process we presently use; specifically solder based receptors and LED attachment points have to be formed which

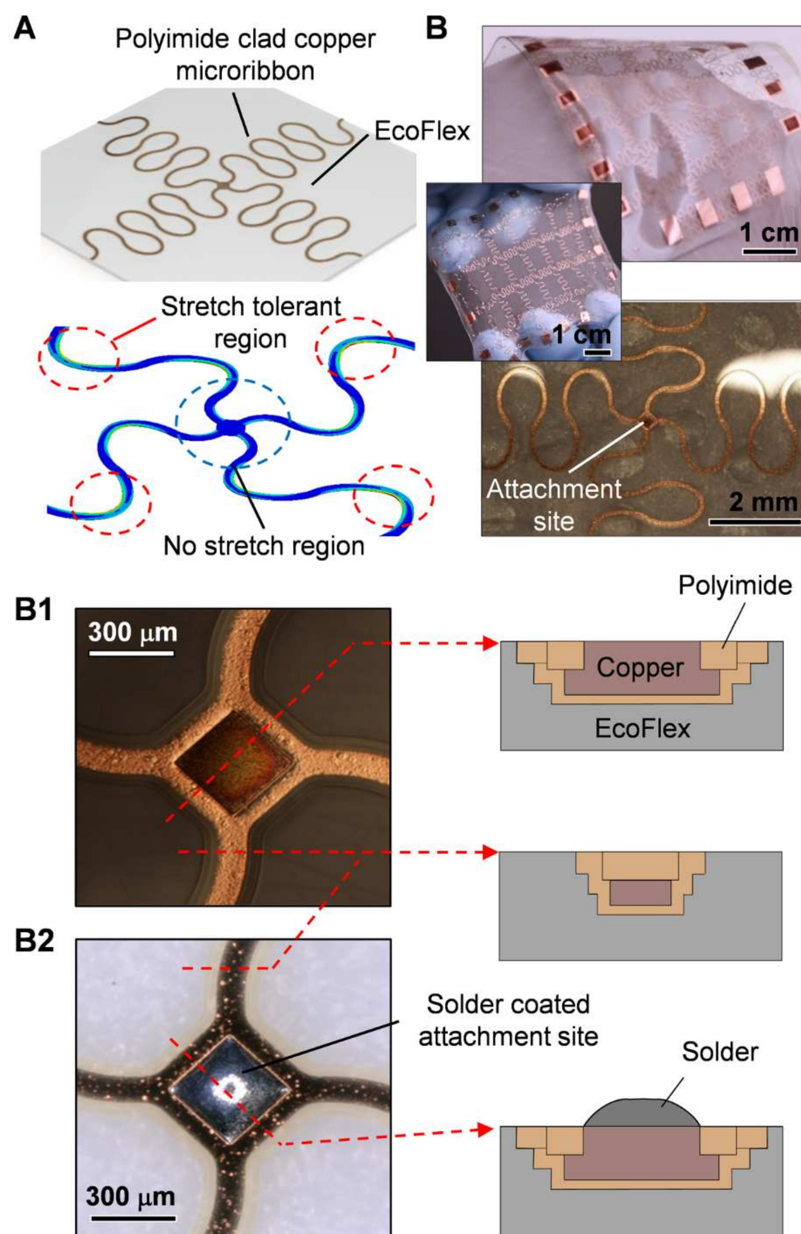

Figure 5-2 Schematics (A) and photographs (B) of the fabricated stretchable bottom electrode. The structure is designed to be compatible with a fluidic self-assembly process which requires the integration of a solder bump in a no-stretch-assembly region. One stress profile calculation (also being discussed in Figure 5-3) is shown. The profile depicts a no-stretch-region (blue circle). The no-stretch-region is the preferred location to define an attachment site for the LEDs with minimal mechanical stress. The attachment sites within the array are electrically connected using 100 µm wide and 5 µm thick meander shaped copper traces. These traces are mechanically and chemically stabilized using a polyimide cladding with the illustrated cross-sections. The color difference in the corresponding top view photographs is due to a difference in the background; a white paper cloth versus a transparent background.

are mechanically stable during the self-assembly process and during operation, (ii) the substrate needs to provide a common electrical connection to the anode of the LEDs, (iii) the interconnection has to be chemically stable during the self-assembly and electrically isolated from the top conductive layer, and (iv) it needs to provide a sufficient amount of mechanical stretchability to relieve the stress between the top and bottom contact of the LEDs during folding.

While a number of previously published methods were tested [35, 119, 120], we ended up with a new design as shown in Figure 5-2. Two major difficulties were found and eliminated.

The first challenge dealt with the interface between the hard and no-stretchable semiconductor dies and the soft and stretchable meander shaped conducting matrix used as interconnection (Figure 5-2(A)). Electrical failure at the interface between hard and soft materials through crack and fracture of the metal was found to be an issue in several designs. The current design minimizes this problem and was based on computation model (Ansys Mechanical) testing several layouts with the goal to achieve a “no-stretch-region” (highlighted with the blue circle) which is larger than the LED chip. Additional calculations and a comparison of various elliptic-arc-interconnect-designs are presented in the supporting information section (Figure 5-6). The chosen design was based on a compromise between redundancy in the number of parallel interconnects and required level of stretchability which is further discussed in the supporting information section. In brief, the depicted design minimizes mechanical stress in close proximity to the chip and diverts the stress to “stretch-tolerant-regions” (highlighted with the red circle).

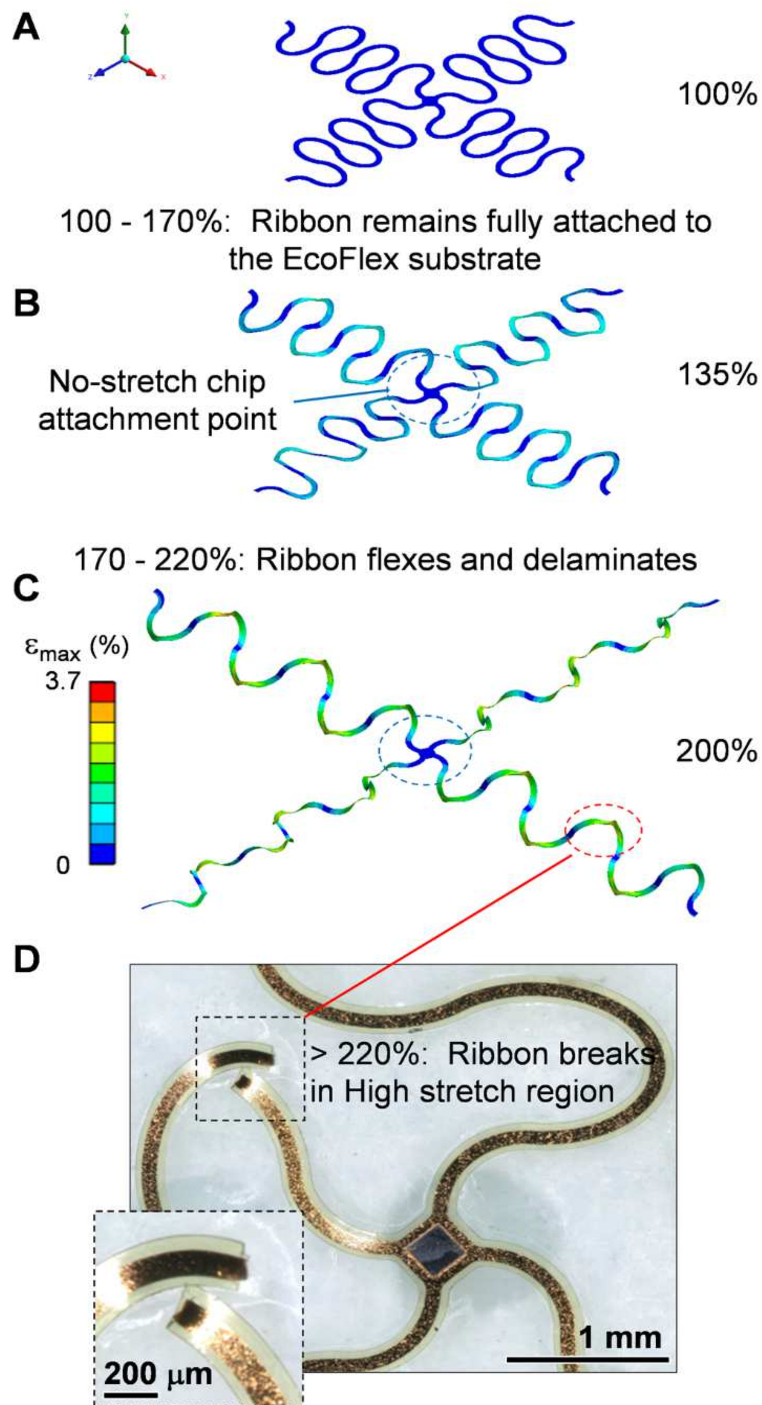

Figure 5-3 Computational analysis and photograph depicting strain (color coded) and mechanical torsion and flexing (Ansys) of the metal ribbons. (A) Reference structure, not being stretched. (B) Reversible stretch region (100-170%); ribbons remain mainly attached to the EcoFlex substrate. (C) Irreversible stretch region (170-220%) leading to complete delamination; localized flexing and torsion of the ribbon is visible. (D) Typical failure exceeding the 220% stretch limit.

The second challenge dealt with the realization of a stretchable interconnect region which is compatible with the fluidic self-assembly process. Previous research used a stretchable interconnect which was tailored to work with conventional robotic assembly [118, 119]. These were not sufficiently stable in our experiments. Several modifications were required to support the fluidic self-assembly process. A complete surrounding of the metallic conductor with a polyimide cladding was required to achieve the mechanical and chemical stability necessary to support subsequent processes such as solder dip-coating and fluidic self-assembly. Without such a cladding, the metal was insufficiently stable during the solder wetting process. Delamination and fracture occurred during the solder dip coating process. Even in regions that did survive the solder dip coating process the metal meander was not sufficiently stable when being stretched. Both problems were eliminated introducing the "polyimide-clad-copper-microribbons" which are traces of copper which are completely surrounded with upper and lower polyimide cladding. The cladding provides additional mechanical strength and additional adhesion to the EcoFlex substrate. Moreover, the polyimide cladding provides an effective method to prevent solder wetting in the stretchable interconnect regions. At the same time it can be lithographically patterned and a window can be defined to access the copper. The ability to define windows is also essential from a self-assembly point of view; the fabrication of non-stretchable chip attachment points and subsequent chip attachment on the basis of solder wetting requires these windows. From a fabrication point of view the "polyimide-clad-copper-microribbons" are supported on top of a silicone rubber (EcoFlex®, Smooth-On) based substrate; Figure 5-7 details the fabrication steps. Attachment sites for the self-

assembly are formed using square-shaped windows in the upper polyimide cladding to access the copper which is subsequently coated with solder (Indalloy #117, MP. 47 °C, Indium Corp., NY) through dip coating. LED attach at these location using the self-assembly process discussed later.

From a stretchability point-of-view, the bottom electrode can be stretched to about 220% (elongated by a factor of 2.2) before electrical failure occurs. Careful analysis, however, shows that the ribbons begin to delaminate from the EcoFlex substrate when being stretched to about 170% of the original length. In the range from 170% to 200% flexing and torsion becomes clearly visible which agree well with computational analysis of these types of unsupported metal ribbons (Figure 5-3 (A-C)). The torsion is a result of the buildup of strain and stress at the outer and inner edge of the meander. We would like to note that the stress relieving mechanism through torsion and delamination is not possible in any device where the metal is sandwiched in between two slabs of EcoFlex. This leads to higher strain on metal traces which eventually cause an earlier failure. For example, as soon as a meander is fully encapsulated with EcoFlex the electrical connections begin to fail at an approximate stretch of 170% of the original length using the current design (5 μm thick and 100 μm wide copper ribbon surrounded with a 8 μm top and 7 μm bottom polyimide cladding (150 and 200 μm wide, respectively). This stretch limit can likely be increased through a reduction of the widths of the ribbons.

All stretch experiments involved anchoring one end of the fabricated electrode to a fixed support while the other end is attached to freely moving support. As a result the reported numbers are for the condition of uniaxial stretching in both the x and y direction.

The previously mentioned 170% represents the limit before irreversible interfacial delamination occurs. The rupture and electrical discontinuity depicted in Figure 5-3D occurred at around 220% stretch along the *x* direction. The encapsulation with a second slap of EcoFlex brings up the question whether voids and air bubbles are introduced as the structure is stretched. The introduction of voids would require a vertical separating force. Indeed there is an origin of a vertical force which is the torsion of the ribbon (clearly visible in Figure 5-3(C)). However, in our design the torsion was not sufficiently strong to cause the formation of stress relieving voids; the ribbon would rupture first.

We have also measured the electrical resistance of the bottom and top electrode as it is being stretched (Supporting information, Figure 5-8(A) and Figure 5-8(B)). On the bottom electrode the electrical resistance remains constant up to 220% stretch. Afterwards we observe an increase in the resistance due to an irreversible mechanical fracture in the stretch tolerant region. The fracture occurs at the predicted location based on the mechanical stress profile calculations (Figure 5-3(C) and Figure 5-3(D)). The top electrode has a different layout. It uses a reduced meander length. As anticipated, the onset of the irreversible mechanical failure occurs earlier with a reduction of the meander length. The electrical resistance remains constant up to 130% stretch.

5.2.2 Part 2: Attachment of the LEDs using solder directed fluidic self-assembly.

We assembled the LEDs on the solder coated attachment sites utilizing a roll-to-roll fluidic self-assemble machine which has been reported recently [103]. It applies LEDs to desired areas on a continuously advancing web using a nozzle, which is similar to conventional printing of inks. However, localized electrical attachment is based on

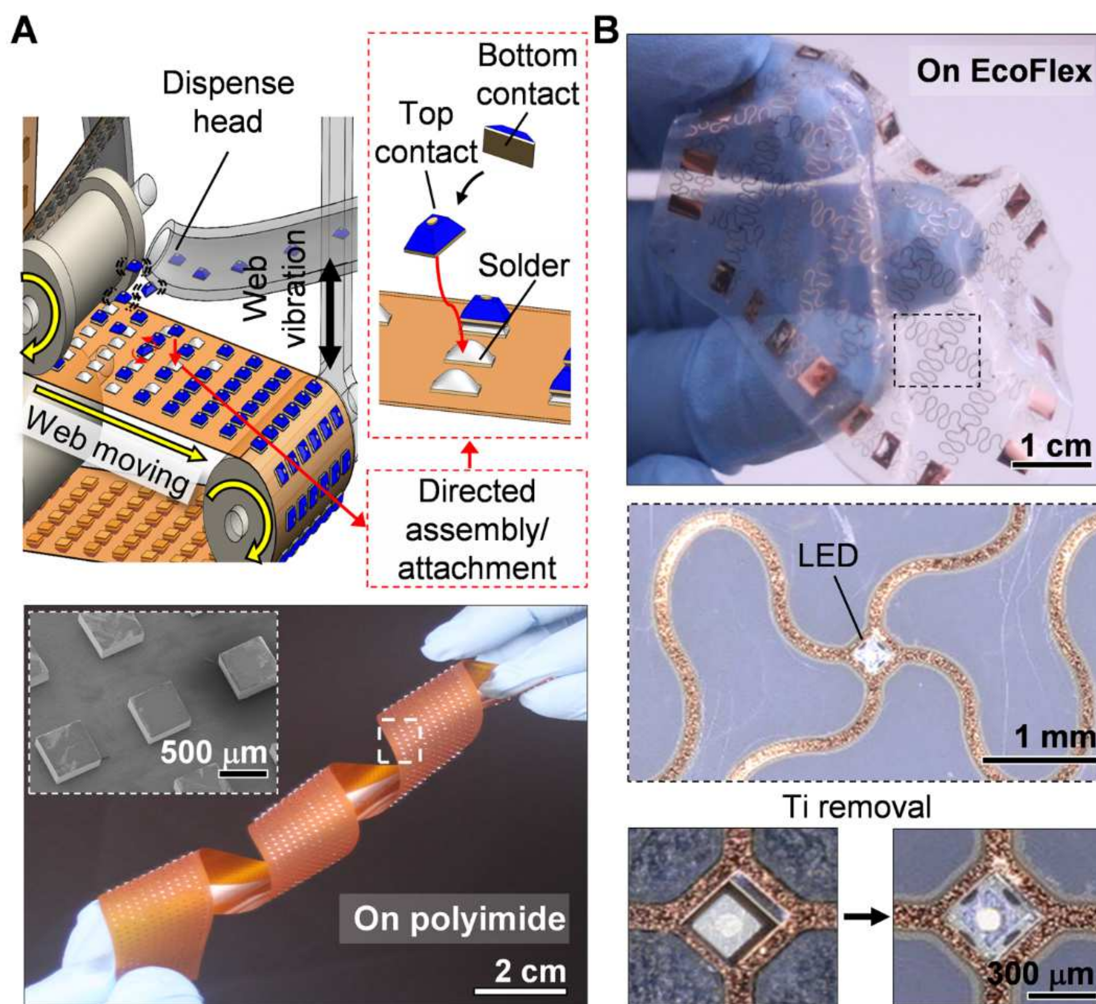

Figure 5-4 Chip attachment using roll-to-roll fluidic assembly and photographs of the resulting structures. (A) The application and assembly of the chips is achieved using localized application using a dispensing head and directed assembly using surface tension-driven assembly [103]. The molten solder bumps have a high surface energy which leads to the attachment and alignment of the chips and the formation of an electrical contact to the anode of chips. Results of assembled chips with a high density (bottom left) and a low area density (right) are shown. A 100 nm thick Ti layer is used as an anti-solder wetting layer to ensure correct right-side-up (negative terminal facing up) LED assembly; this Ti layer is removed in 45 second Ti etch (B, bottom) prior to the lamination of the stretchable top contact.

directed self-assembly on the basis of surface tension-driven assembly involving a conductive adhesive or solder [12, 13, 68, 80, 103, 121]. The reported process (Figure 5-4) is able to assemble semiconductor chips onto continuously advancing substrates with a yield approaching 100%. We used 9000 LED chips in the roll-to-roll fluidic assembly platform. The chips circulate through the system. Access chips are captured at the bottom and reintroduced at the assemble sites. Several adaptations had to be made to get defect-free assemblies using the EcoFlex rubber-like substrates used in this study. EcoFlex caused problems due to non-specific adhesion which hinders the movement and distribution of the components on the substrate. To minimize this non-specific adhesion, a combination of an oxygen plasma treatment (3 min, 100 Watt, 100 sccm O_2) of EcoFlex surface and the use of a non-ionic surfactant inside the assembly solution (Triton X-100, Sigma Aldrich, 5 mL per 1 liter assembly solution) was required. Freely moving components on the substrate was only observed after this treatment. As a result it was possible to achieve defect-free assemblies on the EcoFlex substrates as illustrated in Figure 5-4(B).

It is also important to point out that the LED has two contacts, a small circular top contact and a large square bottom contact. Correct assembly is only possible if the top sides is modified to ensure that the chips assemble with the correct (bottom side) contact on the substrate. This requires the application of a sacrificial 100 nm thick and sputter coated Ti anti-solder wetting layer onto the top face of the LEDs prior to the self-assembly. Solder does not wet this Ti layer which ensures that the chips assemble with the correct orientation on the substrate (Figure 5-4B, *bottom, left*). The Ti coating of

correctly assembled LEDs is removed using a 45 second long wet chemical etch (Figure 5-4(B)*, bottom, right*).

After LED assembly we tested the stretchability of the array. The structure maintained the electrical conductivity up to the previously established 220% stretch limit. Most importantly the introduced localized "no-stretch" assembly sites were found to be very effective to minimize strain; no detachment of the LEDs at these sites was observed during the stretch experiments which means that the meander shaped interconnects would fail first. This is a dramatic improvement over earlier designs were we lost most of the chips as a result of delamination when the substrate was stretched. Moreover, the design satisfied the required mechanical and chemical stability for the self-assembly process. For example no mechanical damage of the bottom electrode was observed as a result of the assembly process.

5.2.3 Part 3: Preparation and Characterization of a Stretchable Conductive Top Layer, Lamination, and Test of the Final Device.

The completion of the lighting module requires the realization and lamination of the top electrode (Figure 5-5). Our goal was to eliminate conventional serial wire-bonding which is commonly used to contact the top layer of the LEDs and to replace this step using a method that can in principle be scaled to a roll-to-roll processing scheme. A solution to this problem is critical since it could lower the production cost and enable processing over larger areas. An ideal method would be a simple lamination step.

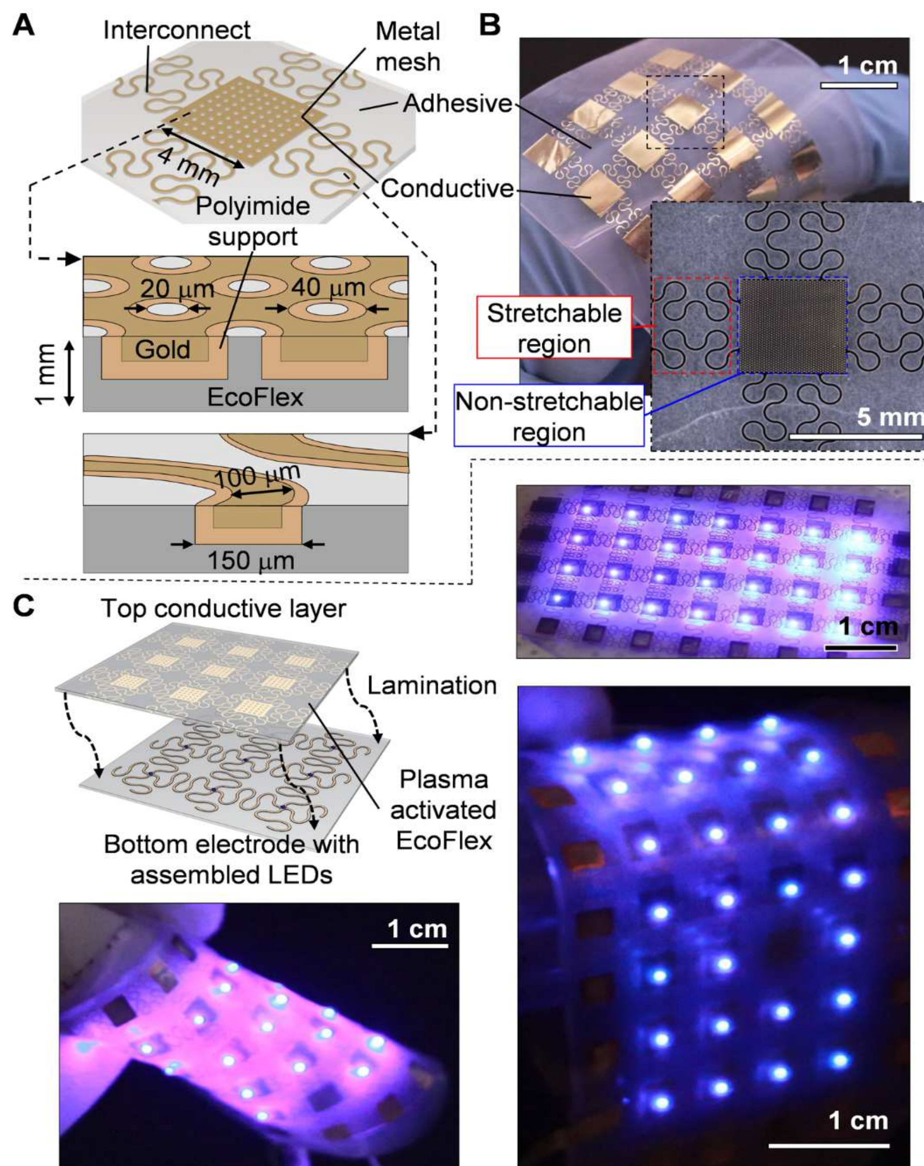

Figure 5-5. Schematics and photographs describing the design, fabrication, and application of the stretchable top conductive lamination layer next to results of a completed 2 mm thin rubber-like module under test. (A) The designed laminate is a composite made up of (i) conductive and (ii) adhesive as well as (iii) stretchable (meander) and (iv) non-stretchable (metal mesh) regions; Oxygen plasma activated EcoFlex acts as an adhesive during the lamination process. The 20 μm in diameter intermediate EcoFlex bonding sites holds the metal mesh in place which in turn contacts the top contact of the LEDs. A weak point of the current design is the abrupt transition from the “non-stretchable” mesh to the “stretchable” meander. Here the polyimide support (a partial cladding visible in A) improves the mechanical stability. (C) The lamination is presently done by hand; as a consequence we used a 4 mm x 4 mm metal mesh to tolerate a 2 mm misalignment with respect to the center contact of the LED. Outside this limit the top contact will not be contacted. The bottom photograph shows a completed lighting module under various levels of deformation.

To accomplish these goals, the top laminate needs to be conductive, provide some level of adhesion, and form electrical interconnects to the top contact of the LEDs. Moreover the laminate needs to relieve mechanical stress when the structure is bent. Figure 5-5(A) and Figure 5-5(B) shows the design next to the fabrication result; Figure 5-9 provided a flowchart of the fabrication steps. We introduce a laminate which integrates 3 design elements:

First, the laminate uses a composite materials approach whereby portions of the surface are more adhesive (not conductive) and other portions are conductive (less adhesive) which allows us to tailor the adhesive strength and interconnect resistance over a wider range then otherwise possible. The adhesive, here in form of oxygen plasma activated silicone rubber, is used to hold the metal-polyimide support structures in place. The approach provides a contact force which pushes the slightly protruding conducting metal (Au or Cu) in contact with the LEDs.

Second, the laminate features an anisotropic stretchable profile which is composed of no-stretch domains (locations to host the rigid and hard LED chips) and high-stretch domains (locations of the stretchable interconnects between isolated device segments) which is more robust when compared with laminates with an isotropic stretch profile.

Third, the laminate eliminates the requirement of critical alignment through the use of a tight metal mesh that provides redundant pathways to the top contacts on the chips. In other words the gold mesh is designed to be very fine using a pitch (40 µm) that

is smaller than the diameter (100 μm) of the top contact. The combination of high-pitch mesh that is extended over larger areas (4 mm x 4 mm) has several benefits: (i) it eliminates critical alignment steps so that alignment can be done by hand, (ii) it provides a number of redundant electrical pathways and electrical connection points (a 2 × 2 redundancy in the current design) to the top contact of the LEDs, (iii) it provides room to expose the intermediate adhesive material (EcoFlex) that increases the mechanical adhesion of this interface. The pitch of LED attachment site (7 mm) was chosen by considering several factors such as distribution of light, aspects to aid in fabrication, and overall desired size of the substrate. The most important factor to aid in the fabrication was the size of the straight-wire-metal-mesh which connects to the top contact of the LEDs. We use 2.5 turns interconnects with a 0.45 mm amplitude for top conductive layer.

Figure 5-5(C) provides images of a functional laminate containing 28 LEDs. Several images of the structure are shown as the structure is bent into different shapes. The entire thickness of the structure is 2 mm. So far we have tested several structures and typically we observe discontinuities in the electrical connection to appear somewhere in the array when the structure is bent to an approximate 1 cm radius of curvature resulting in a defect as shown. We were expecting to achieve a smaller (about 0.5 cm) radius of curvature since the compressive and tensile stress should be in the 10-20% range; the actual numbers depends on the location of the neutral plane; assuming a location close to the center of the slab it is equal to the *thickness*/(2**radius of curvature*) which is 10%; assuming that the location of the neutral plane is shifted towards one side of the slab it would become 20%. Independent of this detail, the top and bottom electrode alone

provided a higher level of stretchability than the calculated 20% upper limit which means that the illustrated defects cannot be a result of fracture of the meander shaped interconnects. Instead the cause is an insufficient adhesion between the cathode of LEDs and the top conductive layer leading to interfacial delamination which is a reversible defect. This means it is possible to apply weak pressure to repair this interface to light up the disconnected LED. Moreover, the structure can be stretched up to 120% of the original length. Beyond this point LEDs in the array begin to turn dark again as a result of interfacial delamination between the metal grid and the top contact; again a full recovery of the function is possible using the application of pressure. The first permanent failure mode is reached when the structure is stretched to about 135%; at this point we were able to record fracture of the meander shaped interconnect in the high stress region; the relatively large metal mesh region, the bottom electrode, and bottom contacts to the LEDs remained intact. To summarize, the weak point of the assembled structure is currently the top layer and in particular the contact to the cathode. We anticipate further improvements using designs which increase the adhesion at this interface.

5.3 Conclusion

Inorganic LEDs are essentially hard objects and area lighting panels with distributed LEDs are often sought of being planar and mechanically rigid. However, in principle it is possible to design rubber-like and mechanically soft lighting structures using inorganic semiconductors if we learn how to distribute and electrically connect microscopic LED chips in a rubber-like matrix. The presented structure was a first step in this direction. The focus of this report was an intentionally chosen multilayer sandwich

structure which is more challenging to fabricate when compared to previously reported structures where the device contacts are on a single face [113, 117, 119, 122]. As a results more steps are required: (i) design of the stretchable bottom electrode, (ii) assembly and electrical connection of microscopic LEDs using a roll-to-roll fluidic self-assembly step, and (iii) the lamination of the top electrode which is different from prior designs. The following key elements have been learned. The combination of *`stretch-tolerant´* regions with *`no-stretch attachment sites´* reduced the bond failure to the chips; the bonds remain intact and sustains the 220% stretch limit set by the meander shaped interconnects. The introduced polyimide cladding increased the robustness of the meander and helped to achieve this number. Such high numbers have been reported previously using meander shaped conductors facing an air interface [123]; however would like to point out that out-of-plane-torsion leads to delamination and controlled pop-up of the conductors under these conditions; this behavior is known to close observers of the field [119, 124, 125]. With the lamination of the top electrode a sandwich structure forms and the relief of this stress through out-of-plane-torsion and pop-up of interconnects is no longer possible. As a result the extremely high level of stretchability will be lost in applications that require encapsulation. This is interesting; most practical application will require protection and some kind of encapsulation [117, 118, 124, 126].

The achieved flexibility and radius of curvature of the entire sandwich structures was not as good as anticipated. The reason appears to be an insufficient force and bond to form a reliable electrical contact between the top of the LEDs and the top laminate. However, the approach to form this contact is new; it was based on hybrid materials

approach using a metal grid with openings to an adhesive to attach the structure. Optimization of this interface has not been done and would require adjustments to the feature size and area of the non-conductive adhesive versus feature size and area of metallic surface.

The use of fluidic self-assembly on stretchable and rubber-like substrates on the other hand was very successful since the assembly yield and speed is on par or better than robotic methods. The process supports the assembly of smaller chips, assembly on non-planar and soft substrates, and higher volume when compared with conventional serial robotic pick and place and wire-bonding.

Finally, the presented methods are not limited to the realization of solid-state lighting panels. It could be extended to other applications in the fields of wearable electronics, energy harvesting, conformable photovoltaics, and electronic or biomedical skins. Applications which require the realization of multicomponent systems and not just the repetition of a single chip type would certainly be more challenging. However, in principle such systems could be made. It would require the use of concepts such as shape recognition to enable flip-chip self-assembly with unique angular alignment or methods of sequential self-assembly to assemble more than one component/chip type on the surface.

5.4 Experimental Section

5.4.1 Bottom electrode

500 μm thick Si wafers (University Wafers, Boston, MA) were first cleaned in a solution of H_2SO_4 + H_2O_2 for 15 min and rinsed with DI water. Following the cleaning step, Poly(methyl methacrylate) (PMMA) is used as a releasing layer. Specifically, 950 PMMA C4 (MicroChem) was spin-coated onto the substrate at 2,000 rpm for 30 sec. After baking at 180 °C for 3 min, a polyimide sacrificial layer (PI2610, HD Microsystem) was spin-coated onto the substrate at 3,000 rpm for 30 sec and pre-baked at 100 °C for 3 min. The polyimide layer was then fully cured in convection oven at 200 °C for 5 hours. The primary photoimageable polyimide layer (HD4100, HD Microsystem) was spin-coated at 2,000 rpm for 30 sec followed by pre-baking at 90 °C for 100 sec and 100 °C for 100 sec subsequently. The substrate was then exposed with 192 mJ cm^{-2} UV light, developed in PA 401D (HD Microsystem) for 150 sec and rinsed in PA 400R (HD Microsystem) for 10 sec. After drying, 10 nm Ti and 200 nm Cu were sputter deposited onto the substrate. Photoresist (AZ9260, AZ Electronic Materials) was then applied at 2,000 rpm, pre-baked at 110 °C for 165 sec and exposed with 500 mJ cm^{-2} UV light. The photoresist was developed using a 1:4 solution of AZ 400K developer diluted with DI water for 3 min. Subsequently a thick copper layer was electroplated in 2:5:20 solution of $CuSO_4$ + H_2SO_4 + DI water for 15 min. The photoresist was removed using a RIE (O_2, 100 sccm, 100 W, 100 mTorr). The thin sputtered Cu and Ti layer were subsequently wet-etched in 30% $FeCl_3$ and buffered oxide etch solutions. The fabrication of secondary polyimide layer followed the same process with the primary polyimide layer above. After

patterning the secondary polyimide layer, a silicone rubber precursor (EcoFlex 00-30, Smooth-On, Inc.) was poured onto the substrate and cured at room temperature for 4 hours. The entire bottom electrode was then transferred to silicone rubber from the Si substrate by removing PMMA releasing layer with Acetone. The remaining polyimide sacrificial layer was removed using a RIE (80 sccm O_2 + 20 sccm CF_4, 200 W, 100 mTorr). Finally, the receptor was formed by dip-coating in a heated solder bath.

5.4.2 Top conductive layer

The fabrication of top conductive lamination layer follows the cleaning process, coating PMMA releasing layer and polyimide sacrificial layer process above. After coating the sacrificial layer, 10 nm Cr and 250 nm Au was deposited using an e-beam evaporator onto the substrate. Photoresist (Microposit 1813 Shipley) is applied (3,000 rpm), exposed, and developed in 1 Microposit 351 : 5 H_2O developer (25 sec). The Au and Cr layers were subsequently wet-etched followed by removing the photoresist using a RIE. Subsequent processes like patterning the polyimide layer, applying the silicone rubber support, transfer, release, removal of the sacrificial layer were identical to what has been described above. Before lamination step the silicone rubber surface was activate using O_2 plasma (100 sccm, 100 W, 100 mTorr).

5.5 Acknowledgements

The research received financial support in part through grants from the National Science Foundation (NSF Grant DMI-1068013), German Science Foundation (DFG Grants JA 1023/3-1), and the Carl-Zeiss Foundation.

5.6 Supporting Information

We compared a “single loop design” with a “multiple loop compressed arc design” which confirmed that the strain and stress reduces with an increased number of windings and path length of the looped interconnecting line. Next, we compared a “large-amplitude single-loop design” with a “small-amplitude multi-loop design” which had an identical path length along the trajectory of the loops. The large amplitude design leads to a reduction of the stress and strain. The design that we choose in the end was a compromise. We decided to limit the amplitude to 0.8 mm which leaves a sufficiently large space. The space is used to provide four redundant connections to the straight-wire-metal-mesh which connects to the top contact of the LEDs.

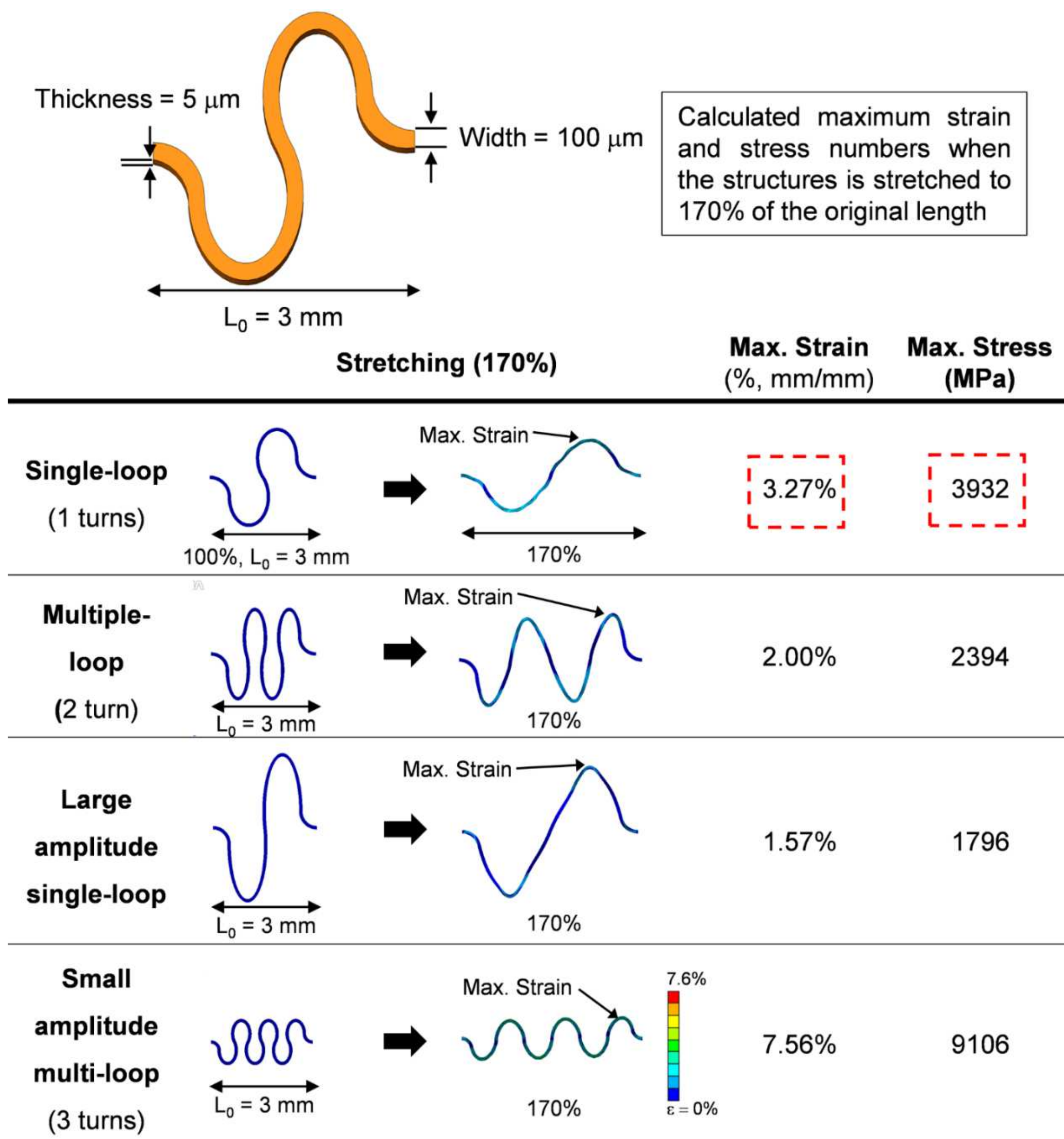

Figure 5-6 Comparison of mechanical properties of various interconnect designs such as large amplitude, small amplitude with many turns.

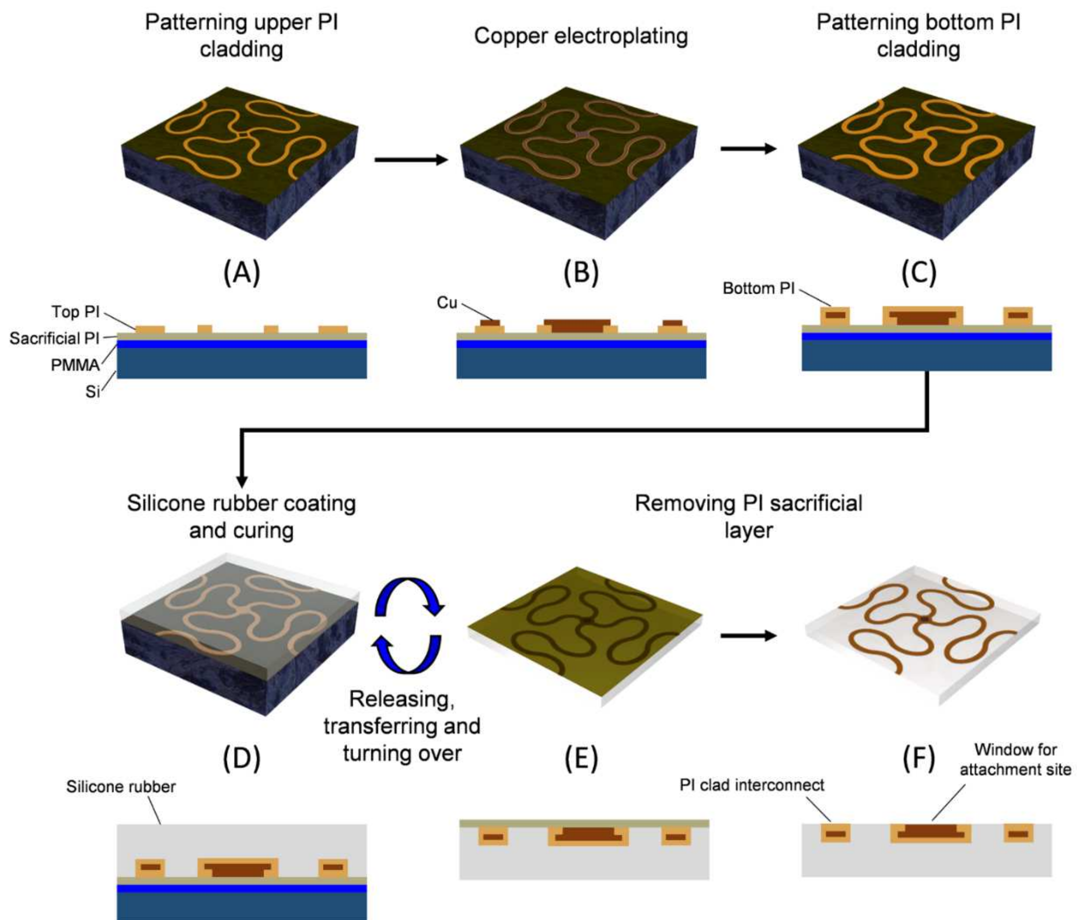

Figure 5-7 Fabrication procedure of the bottom electrode. (A) Patterning of the upper polyimide (PI) cladding on the Si substrate with PMMA releasing layer and PI sacrificial layer. (B) Electroplating copper based conductive traces. (C) Patterning bottom PI cladding on top of copper traces. (D) Coating and curing silicone rubber substrate. (E) Releasing and transferring the bottom electrode to the silicone substrate from the Si substrate. (F) Removing the PI sacrificial layer using a reactive ion etch.

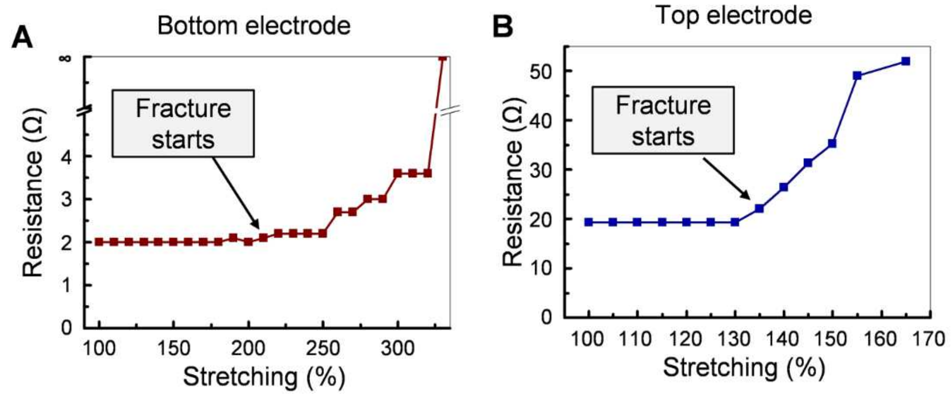

Figure 5-8**.** Electrical resistance testing with stretching. (A) The bottom electrode (2.0-2.2 ohm, Cu meanders, 100 µm wide and 5 µm thick), Electrical resistance remained constant up to 220% stretch. (B) The top electrode (19.0-19.3 ohm, Au meanders, 100 µm wide and 0.25 µm thick), Electrical resistance remained constant up to 130% stretch.

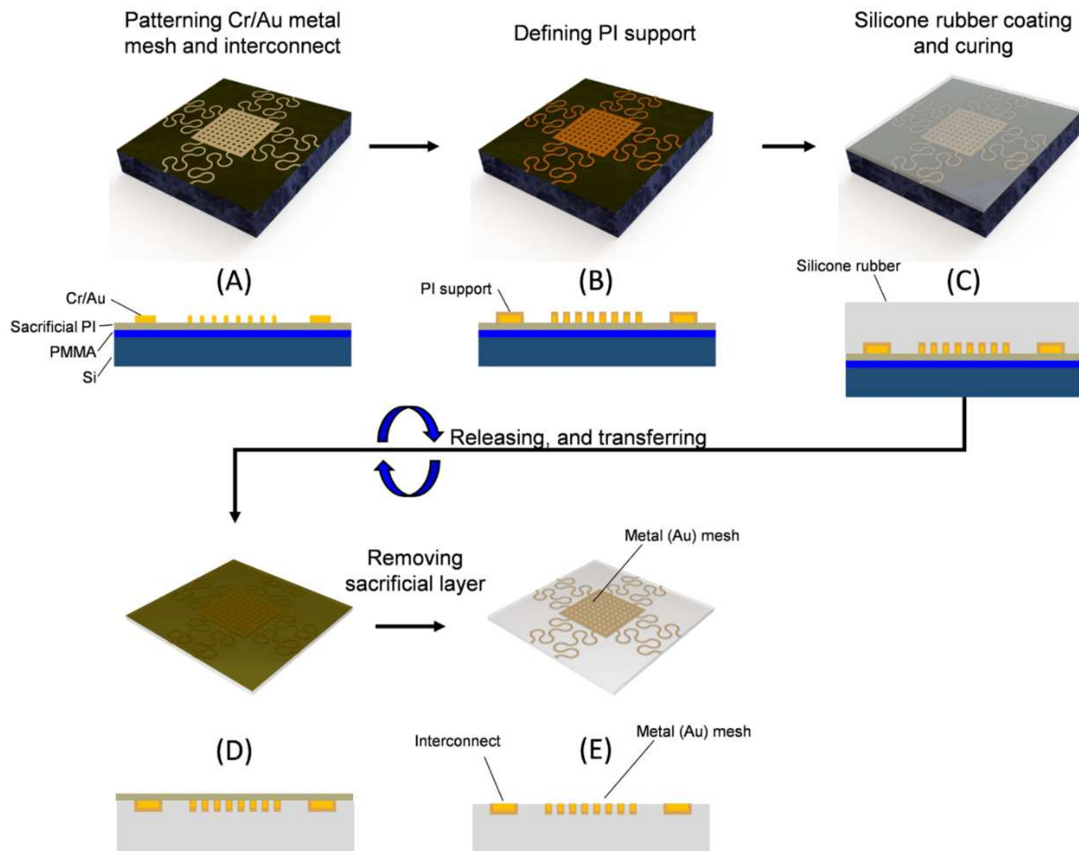

Figure 5-9. Fabrication procedure of the top conductive lamination layer. (A) Patterning Cr/Au metal mesh and interconnects. (B) Defining polyimide (PI) support layer. (C) Applying silicone rubber. (D) Releasing and transferring the top conductive layer. (E) Removing the sacrificial PI using a reactive ion etch.

5.7 *Advanced Materials* Table of Contents

A millimeter thin rubber-like solid-state lighting module is reported. The fabrication of the lighting module incorporates assembly and electrical connection of LEDs. The assembly is achieved using a roll-to-roll fluidic self-assembly. The realized structure is a 2 mm thin multilayer structure. The LEDs are sandwiched in-between a stretchable top and bottom electrode to relieve the stress as the structure is bent. The top contact is realized using a novel lamination which eliminates critical alignment and wire-bonding.

Keyword : reel to reel process, fluidic self-assembly, flexible electronics, solid state lighting.

Se-Chul Park, Jun Fang, Shantonu Biswas, Mahsa Mozafari, Thomas Stauden, and Heiko O. Jacobs

Millimeter Thin and Rubber-Like Solid-State Lighting Modules Fabricated Using Roll-to-Roll Fluidic Self-Assembly and Lamination

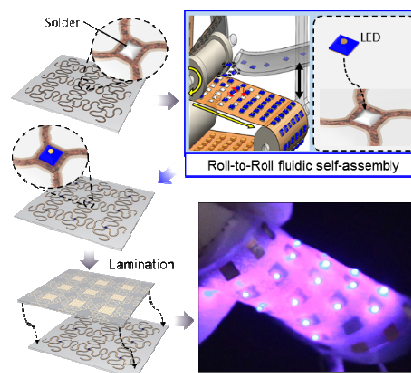

Figure 5-10. Table of Contents

CHAPTER VI

6. Conclusion

In this thesis, we have focused on the extension of surface-tension driven fluidic self-assembly technique based on molten solder receptors to enable automated, high throughput, large-area integration of functional semiconductor chips. Compared with Ink-Jet printing, which is the most commonly used method for organic semiconductor, the self-assembly can be used for inorganic semiconductor, providing longer lifetime and higher carrier mobility. Moreover, while the pitch and functional density are limited to the parallel transfer method, they can be freely designed to any desired values in the self-assembly method which distributes and assembles inorganic semiconductor chips.

First, we have developed the automated fluidic self-assembly system on the basis of the surface-tension driven self-assembly. Our self-assembly system is different from the discontinuous, small batch process which has previously been demonstrated by others. By combining the conveyer belt-like process and roll-to-roll type approach with molten-solder driven self-assembly, our system provides a new route to realize a high throughput integration/assembly. The current system can achieve 15,000 chips per hour with high assembly yield of 99% using a 2.5 cm web. The assembly speed is comparable

with a high-end conventional robotic assembly machine. However, owing to the parallel manner of the self-assembly, it is quiet straight forward to scale the system to any desired throughput by increasing the number of the dispensing unit and width of the web. We believe that the high yield and high accuracy results are mainly from high surface tension of the molten solder. The molten solder driven self-assembly can be further extended to other approaches using magnetic force, gravity, electrophoretic and dielectrophoretic force, and shape recognition.

We have also discussed the experimental optimization process, followed by identification and modeling of the governing forces of our system. Under various operation conditions, we tested the assembly of components with different sizes. In the future, the knowledge obtained from our optimization and analysis of such systems may contribute to the design of automated fluidic self-assembly processes.

We have also demonstrated the solid-state lighting modules by distribution, assembly, and electrical connection of inorganic LEDs on flexible and/or stretchable substrates. For electrical connection, we have introduced a novel lamination step of polymer based conductive layer. This lamination approach is designed to eliminate the conventional wire-bonding process which is a major time-consuming process for electrical connection to a large quantity of components over a large area. Therefore, when further optimized, this approach can be a new way to form electrical connections with less complexity and low cost. The applications of our roll-to-roll system are not limited to solid-state lighting modules, but also include flexible large-area solar panels, wearable health monitoring systems, and flexible displays.

Our system can be further improved, when combined with the shape recognition concept or the sequential multi-batch process, to assemble more than one type of chips and thus, become a heterogeneous system. Moreover, the concept used in our roll-to-roll fluidic self-assembly can be applied to integrate much smaller chips as well. In the future, the techniques we have described in this thesis can be applied to systems with different materials, size, and function. We believe that our technology may help realize a more cost-effective manufacturing technology in the fields of macroelectronics, flexible electronics, and wearable electronics.

CHAPTER VII

7. Bibliography

[1] R. H. Reuss, B. R. Chalamala, A. Moussessian, M. G. Kane, A. Kumar, D. C. Zhang*, et al.*, "Macroelectronics: Perspectives on Technology and Applications," *Proceedings of the IEEE,* vol. 93, pp. 1239-1256, 2005.

[2] *Simense SIPLACE SX series DataSheet*. Available: http://www.siplace.com/bausteine.net/f/6620/DaBl_SIPLACESXeng_1906.pdf?fd=2

[3] R.S.Fearing, "Survey of Sticking Effects for Micro Parts Handling," in *IEEE/RSJ International Conference on Intelligent Robots and Systems*, Los Alamitos, CA, 1995, pp. 212-217.

[4] J. J. Cole, C. R. Barry, X. Wang, and H. O. Jacobs, "Nanocontact electrification through forced delamination of dielectric interfaces," *ACS Nano,* vol. 4, pp. 7492-8, Dec 28 2010.

[5] J. J. Cole, C. R. Barry, R. J. Knuesel, X. Wang, and H. O. Jacobs, "Nanocontact electrification: patterned surface charges affecting adhesion, transfer, and printing," *Langmuir,* vol. 27, pp. 7321-9, Jun 7 2011.

[6] M.B.Cohn, K.F.Böhringer, J. M. Noworolski, A. Singh, C. G. Keller, K. Y. Goldberg*, et al.*, "Microassembly Technologies for MEMS," in *Proceedings of SPIE on Micromachined Devices and Components*, Santa Clara, CA, 1998, pp. 2-16.

[7] D.-H. Kim, J.-H. Ahn, H.-S. Kim, K.-J. Lee, T.-H. Kim, C.-J. Yu*, et al.*, "Complementary logic gates and ring oscillators on plastic substrates by use of printed ribbons of single-crystalline silicon," *IEEE Electron Device Lett,* vol. 29, pp. 73-76, 2008.

[8] Y.-L. Loo, R. L. Willett, K. W. Baldwin, and J. A. Rogers, "Additive, nanoscale patterning of metal films with a stamp and a surface chemistry mediated transfer process: Applications in plastic electronics," *Appl. Phys. Lett.,* vol. 81, pp. 562-564, 2002.

[9] H. C. Ko, M. P. Stoykovich, J. Song, V. Malyarchuk, W. M. Choi, C.-J. Yu*, et al.*, "A hemispherical electronic eye camera based on compressible silicon optoelectronics," *Nature,* vol. 454, pp. 748-753, 2008.

[10] J. Yoon, A. J. Baca, S.-I. Park, P. Elvikis, J. B. Geddes, III, L. Li*, et al.*, "Ultrathin silicon solar microcells for semitransparent, mechanically flexible and microconcentrator module designs," *Nature Mater.,* vol. 7, pp. 907-915, 2008.

[11] H. J. J. Yeh and J. S. Smith, "Fluidic self-assembly for the integration of gaas light-emitting diodes on si substrates," *IEEE Photonic Tech. L.,* vol. 6, pp. 706-708, 1994.

[12] H. O. Jacobs, A. R. Tao, A. Schwartz, D. H. Gracias, and G. M. Whitesides, "Fabrication of a Cylindrical Display by Patterned Assembly," *Science,* vol. 296, pp. 323-325, 2002.

[13] W. Zheng, P. Buhlmann, and H. O. Jacobs, "Sequential Shape-and-Solder-Directed Self-Assembly of Functional Microsystems," *Proc. Natl. Acad. Sci.,* vol. 101, pp. 12814-12817, 2004.

[14] W. Zheng and H. O. Jacobs, "Shape-and-Solder-Directed Self-Assembly to Package Semiconductor Device Segments," *Appl. Phys. Lett.,* vol. 85, pp. 3635-3637, 2004.
[15] W. Zheng and H. O. Jacobs, "Fabrication of Multicomponent Microsystems by Directed Three-Dimensional Self-Assembly," *Adv. Func. Mater.,* vol. 15, pp. 732-738, 2005.
[16] W. Zheng, J. B. Chung, and H. O. Jacobs, "Non-robotic fabrication of packaged microsystems by shape-and-solder-directed self-assembly," in *IEEE International Conference on Micro Electro Mechanical Systems*, Miami, FL, 2005, pp. 8-11.
[17] J. H. Chung, W. Zheng, and H. O. Jacobs, "Programmable reconfigurable self-assembly: approaching the parallel heterogeneous integration on flexible substrates," in *IEEE International Conference on Micro Electro Mechanical Systems.*, Miami, FL, 2005, pp. 572-575.
[18] W. Zheng and H. O. Jacobs, "Self-assembly process to integrate and connect semiconductor dies on surfaces with single-angular orientation and contact-pad registration," *Adv. Mater.,* vol. 18, pp. 1387-1392, 2006.
[19] S. A. Stauth and B. A. Parviz, "Self-assembled single-crystal silicon circuits on plastic," *Proc. Natl. Acad. Sci.,* vol. 103, pp. 13922-13927, 2006.
[20] W. Zheng and H. O. Jacobs, "Fluidic Heterogeneous Microsystems Assembly and Packaging," *Journal of Microelectromechanical Systems,* vol. 15, pp. 864-870, 2006.
[21] J.-H. Chung, W. Zheng, T. J. Hatch, and H. O. Jacobs, "Programmable Reconfigurable Self-Assembly: Parallel Heterogeneous Integration of Chip-Scale Components on Planar and Nonplanar Surface," *Journal of Microelectromechanical systems,* vol. 15, pp. 457-464, 2006.
[22] G. P. Crawford, "A bright new page in portable displays," *IEEE Spectrum,* vol. 37, pp. 40-46, Oct 2000 2000.
[23] P. Liu, S. Ferguson, D. Edwards, and Y. Sasaki, "Radio frequency identification device and method," US Patent 6867983, 2002.
[24] J. J. Cole, X. Wang, R. J. Knuesel, and H. O. Jacobs, "Patterned growth and transfer of ZnO micro- and nanocrystals with size and location control," *Advanced Materials,* vol. 20, pp. 1474-1478, 2008.
[25] Y. Sun, S. Kim, I. Adesida, and J. A. Rogers, "Bendable GaAs metal-semiconductor field-effect transistors formed with printed GaAs wire arrays on plastic substrates," *Appl. Phys. Lett.,* vol. 87, pp. 083501/1-083501/3, 2005.
[26] Y. Sun and J. A. Rogers, "Fabricating Semiconductor Nano/Microwires and Transfer Printing Ordered Arrays of them onto Plastic Substrates," *Nano Lett.,* vol. 4, pp. 1953-1959, 2004.
[27] K. J. Lee, M. A. Meitl, J.-H. Ahn, J. A. Rogers, R. G. Nuzzo, V. Kumar*, et al.*, "Bendable GaN high electron mobility transistors on plastic substrates," *J. Appl. Phys.,* vol. 100, pp. 124507/1-124507/4, 2006.
[28] Z. T. Zhu, E. Menard, K. Hurley, R. G. Nuzzo, and J. A. Rogers, "Spin on dopants for high-performance single-crystal silicon transistors on flexible plastic substrates," *Appl. Phys. Lett.,* vol. 86, pp. 133507/1-133507/3, 2005.
[29] M. A. Meitl, Z.-T. Zhu, V. Kumar, K. J. Lee, X. Feng, Y. Y. Huang*, et al.*, "Transfer printing by kinetic control of adhesion to an elastomeric stamp," *Nature Mater.,* vol. 5, pp. 33-38, 2006.
[30] J. Lee, J. Wu, M. Shi, J. Yoon, S.-I. Park, M. Li*, et al.*, "Stretchable GaAs Photovoltaics with Designs That Enable High Areal Coverage," *Advanced Materials,* vol. 23, pp. 986-991, 2011.

[31] A. M. Gaikwad, A. M. Zamarayeva, J. Rousseau, H. Chu, I. Derin, and D. A. Steingart, "Highly Stretchable Alkaline Batteries Based on an Embedded Conductive Fabric," *Advanced Materials,* vol. 24, pp. 5071–5076, 2012.
[32] M. Kaltenbrunner, G. Kettlgruber, C. Siket, R. Schwödiauer, and S. Bauer, "Arrays of Ultracompliant Electrochemical Dry Gel Cells for Stretchable Electronics," *Advanced Materials,* vol. 22, pp. 2065-5067, 2010.
[33] T. Someya, Y. Kato, T. Sekitani, S. Iba, Y. Noguchi, Y. Murase*, et al.*, "Conformable, flexible, large-area networks of pressure and thermal sensors with organic transistor active matrixes," *Proceedings of the National Academy of Sciences of the United States of America,* vol. 102, pp. 12321-12325, 2005.
[34] B. C.-K. Tee, C. Wang, R. Allen, and Z. Bao, "An electrically and mechanically self-healing composite with pressure- and flexion-sensitive properties for electronic skin applications," *Nature Nanotechnology,* vol. 7, pp. 825-832, 2012.
[35] D.-H. Kim, N. Lu, R. Ma, Y.-S. Kim, R.-H. Kim, S. Wang*, et al.*, "Epidermal Electronics," *Science,* vol. 333, pp. 838-843, 2011.
[36] R. C. Webb, A. P. Bonifas, A. Behnaz, Y. Zhang, K. J. Yu, H. Cheng*, et al.*, "Ultrathin conformal devices for precise and continuous thermal characterization of human skin," *Nature Materials,* vol. 12, pp. 938-944, 2013.
[37] R. G. Nuzzo and D. L. Allara, "Adsorption of bifunctional organic disulfides on gold surfaces," *Journal of the American Chemical Society,* vol. 105, pp. 4481-4483, 1983.
[38] C. Mao, W. Sun, and N. C. Seeman, "Assembly of Borromean rings from DNA," *Nature,* vol. 386, pp. 137-138, 1997.
[39] K. S. Chichak, S. J. Cantrill, A. R. Pease, S.-H. Chiu, G. W. V. Cave, J. L. Atwood*, et al.*, "Molecular Borromean Rings," *Science,* vol. 304, pp. 1308-1312, 2004.
[40] G. M. Whitesides and B. Grzybowski, "Self-Assembly at All Scales," *Science,* vol. 295, pp. 1766-1769, 2002.
[41] G. M. Whitesides and M. Boncheva, "Beyond Molecules: Self-Assembly of Mesoscopic and Macroscopic Components," *Proceedings of the National Academy of Sciences,* vol. 99, pp. 4769-4774, 2002.
[42] J. P. Mathias, E. E. Simanek, C. T. Seto, and G. M. Whitesides, "Self Assembly through Hydrogen Bonding: Preparation of a Supramolecular Aggregate Composed of Ten Molecules," *Angewandte Chemie International Edition,* vol. 32, pp. 1766-1769, 1993.
[43] D. J. Norris and Y. A. Vlasov, "Chemical Approaches to Three-Dimensional Semiconductor Photonic Crystals," *Advanced Materials,* vol. 13, pp. 371-376, 2001.
[44] M. Mastrangeli, S. Abbasi, C. Varel, C. Van Hoof, J. Celis, K. Böhringer*, et al.*, "Self-assembly from milli-to nanoscales: methods and applications," *J. Micromech. Microeng.,* vol. 19, p. 083001, 2009.
[45] J. H. Fendler, "Chemical Self-Assembly for Electronic Applications," *Chemistry of Materials,* vol. 13, pp. 3796-9210, 2001.
[46] Y. Xia, B. Gates, and Z. Y. Li, "Self-Assembly Approaches to Three-Dimensional Photonic Crystals," *Advanced Materials,* vol. 13, pp. 409-413, 2001.
[47] C. Chothia and J. Janin, "Principles of Protein-Protein Recognition," *Nature,* vol. 256, pp. 705-708, 1975.
[48] J. Janin, "Protein-Protein Recognition," *Progress in Biophysics and Molecular Biology,* vol. 64, pp. 145-166, 1995.
[49] J. T. Moore, P. D. Beale, T. A. Winningham, and K. Douglas, "Controlled Morphology of Biologically Derived Metal Nanopatterns," *Applied Physics Letters,* vol. 71, pp. 1264-1266, 1997.

[50] M. J. Dabrowski, J. P. Chen, H. Shi, W. C. Chin, and W. M. Atkins, "Strategies for Protein-Based Nanofabrication: Ni2+-Nta as a Chemical Mask to Control Biologically Imposed Symmetry," *Chemistry & Biology,* vol. 5, pp. 689-697, 1998.

[51] E. Braun, Y. Eichen, U. Sivan, and G. Ben-Yoseph, "DNA-Templated Assembly and Electrode Attachment of a Conducting Silver Wire," *Nature,* vol. 391, pp. 775-778, 1998.

[52] P. Malherbe, J. G. Richards, H. Gaillard, A. Thompson, C. Diener, A. Schuler*, et al.*, "cDNA Cloning of a Novel Secreted Isoform of the Human Receptor for Advanced Glycation End Products and Characterization of Cells Co-Expressing Cell-Surface Scavenger Receptors and Swedish Mutant Amyloid Precursor Protein," *Molecular Brain Research,* vol. 71, pp. 159-170, 1999.

[53] C. Niemeyer, B. Ceyhan, S. Gao, L. Chi, S. Peschel, and U. Simon, "Site-Selective Immobilization of Gold Nanoparticles Functionalized with DNA Oligomers," *Colloid & Polymer Science,* vol. 279, pp. 68-72, 2001.

[54] C. Niemeyer, "Progress in "Engineering up" Nanotechnology Devices Utilizing DNA as a Construction Material," *Applied Physics A: Materials Science & Processing,* vol. 68, pp. 119-124, 1999.

[55] I. S. Choi, N. Bowden, and G. M. Whitesides, "Macroscopic, Hierarchical, Two-Dimensional Self-Assembly," *Angewandte Chemie International Edition,* vol. 38, pp. 3078-3081, 1999.

[56] P. Yang, A. H. Rizvi, B. Messer, B. F. Chmelka, G. M. Whitesides, and G. D. Stucky, "Patterning Porous Oxides within Microchannel Networks," *Advanced Materials,* vol. 13, pp. 427-431, 2001.

[57] C. Petit, A. Taleb, and M. P. Pileni, "Self-Organization of Magnetic Nanosized Cobalt Particles," *Advanced Materials,* vol. 10, pp. 259-261, 1998.

[58] Y. Saado, T. Ji, M. Golosovsky, D. Davidov, Y. Avni, and A. Frenkel, "Self-Assembled Heterostructures Based on Magnetic Particles for Photonic Bandgap Applications," *Optical Materials,* vol. 17, pp. 1-6, 2001.

[59] W. Zhou, E. Carpenter, J. Lin, A. Kumbhar, J. Sims, and C. O'Connor, "Nanostructures of Gold Coated Iron Core-Shell Nanoparticles and the Nanobands Assembled under Magnetic Field," *The European Physical Journal D - Atomic, Molecular, Optical and Plasma Physics,* vol. 16, pp. 289-292, 2001.

[60] R. H. M. Chan, C. K. M. Fung, and W. J. Li, "Rapid assembly of carbon nanotubes for nanosensing by dielectrophoretic force," *Nanotechnology,* vol. 15, pp. 672-677, 2004.

[61] H. O. Jacobs and G. M. Whitesides, "Submicrometer patterning of charge in thin-film electrets," *Science,* vol. 291, pp. 1763-6, Mar 2 2001.

[62] H. O. Jacobs, S. A. Campbell, and M. G. Steward, "Approaching Nanoxerography: The Use of Electrostatic Forces to Position Nanoparticles with 100 Nanometer Scale Resolution," *Advanced Materials,* vol. 14, pp. 1553-1557, 2002.

[63] C. R. Barry, M. G. Steward, and H. O. Jacobs, "Nanoxerography: The Use of Electrostatic Forces to Pattern Nanoparticles," in *Proceedings of The 2003 NSF Design, Service and Manufacturing Grantees and Research Conference*, Birmingham, Alabama, 2003.

[64] E. C. Lin, J. Fang, S. C. Park, T. Stauden, J. Pezoldt, and H. O. Jacobs, "Effective collection and detection of airborne species using SERS-based detection and localized electrodynamic precipitation," *Adv Mater,* vol. 25, pp. 3554-9, Jul 12 2013.

[65] E. C. Lin, J. Fang, S. C. Park, F. W. Johnson, and H. O. Jacobs, "Effective localized collection and identification of airborne species through electrodynamic precipitation and SERS-based detection," *Nat Commun,* vol. 4, p. 1636, 2013.

[66] Y. Xia, B. Gates, Y. Yin, and Y. Lu, "Monodispersed colloidal spheres: Old materials with new applications," *advanced Materials,* vol. 12, pp. 693-713, 2000.

[67] A. Blaaderen, R. Ruel, and P. Wiltzius, "Template-directed colloidal crystallization," *Nature,* vol. 385, pp. 321-324, 1997.

[68] R. J. Knuesel and H. O. Jacobs, "Self-assembly of microscopic chiplets at a liquid-liquid-solid interface forming a flexible segmented monocrystalline solar cell," *Proc. Natl. Acad. Sci.,* vol. 107, pp. 993-8, Jan 19 2010.

[69] R. J. Knuesel and H. O. Jacobs, "Self-tiling monocrystalline silicon; a process to produce electrically connected domains of Si and microconcentrator solar cell modules on plastic supports," *Adv Mater,* vol. 23, pp. 2727-33, Jun 24 2011.

[70] R. Knuesel, S. Park, W. Zheng, and H. O. Jacobs, "Self-assembly and self-tiling: integrating active dies across length scales on flexible substrates," *Journal of Microelectromechanical Systems,* vol. 21, pp. 85-99, 2012.

[71] C. G. Fonstad, "Magnetically-Assisted Statistical Assembly - a new heterogeneous integration technique," *MIT technical report,* 2002.

[72] E. Iwase and I. Shimoyama, "Multistep sequential batch assembly of three-dimensional ferromagnetic microstructures with elastic hinges," *Journal of Microelectromechanical Systems,* vol. 14, pp. 1265-1271, 2005.

[73] J. C. Breger, C. Yoon, R. Xiao, H. R. Kwag, M. O. Wang, J. P. Fisher*, et al.*, "Self-folding thermo-magnetically responsive soft-microgrippers," *ACS Applied Materials and Interfaces,* vol. 7, pp. 3398-3405, 2015.

[74] J. S. Smith and H. J. J. Yeh, "Method and apparatus for fabricating self-assembling microstructures," US Patent, 1998.

[75] C. F. Edman, R. B. Swint, C. Gurtner, R. E. Formosa, S. D. Roh, K. E. Lee*, et al.*, "Electric field directed assembly of an InGaAs LED onto silicon circuitry," *IEEE Photonics Technology Letters,* vol. 12, pp. 1198-1200, 2000.

[76] H. Ye, Z. Gu, T. Yu, and D. H. Gracias, "Integrating nanowires with substrates using directed assembly and nanoscale soldering," *IEEE Transactions on Nanotechnology,* vol. 5, pp. 62-66, 2006.

[77] S. J. Papadakis, Z. Gu, and D. H. Gracias, "Dielectrophoretic assembly of reversible and irreversible metal nanowire networks and vertically aligned arrays," *Appl. Phys. Lett.,* vol. 88, pp. 233118-1 - 3, 2006.

[78] X. Xiong, Y. Hanein, J. Fang, Y. Wang, W. Wang, D. T. Schwartz*, et al.*, "Controlled Multibatch Self-Assembly of Microdevices," *JOURNAL OF MICROELECTROMECHANICAL SYSTEMS,* vol. 12, pp. 117-127, 2003.

[79] U. Srinivasan, D. Liepmann, and R. T. Howe, "Microstructure to substrate self-assembly using capillary forces," *J. Microelectromech. S,* vol. 10, pp. 17-24, 2001.

[80] U. Srinivasan, M. A. Helmbrecht, C. Rembe, R. S. Muller, and R. T. Howe, "Fluidic self-assembly of micromirrors onto microactuators using capillary forces," *IEEE J. Sel. Top. Quantum. Electron.,* vol. 8, pp. 4-11, 2002.

[81] K. F. Böhringer, U. Srinivasan, and R. T. Howe, "Modeling of Fluidic Forces and Binding Sites for Fluidic Self-Assembly," in *Proc. 14th Int. Conf. Micro Electro. Mech. S.*, Interlaken, Switzerland, 2001.

[82] P. W. K. Rothermund, "Using lateral capillary forces to compute by self-assembly," *Proceedings of the National Academy of Sciences,* vol. 97, pp. 984–989, 1999.

[83] S. Park and K. F. Böhringer, "A Fully Dry Self-Assembly Process with Proper in-Plane Orientation," in *IEEE International Conference on Micro Electro Mechanical Systems*, Tucson, AZ, 2008, pp. 1077-1080.

[84] J. Fang and K.F.Böhringer, "Parallel micro component-to-substrate assembly with controlled poses and high surface coverage," *Journal of Micromechanics and Microengineering,* vol. 16, pp. 721-730, 2006.

[85] K. Hosokawa, I. Shimoyama, and H. Miura, "Two-Dimensional Micro-Self-Assembly Using the Surface Tension of Water," *Sensors and Actuators A: Physical,* vol. 57, pp. 117-125, 1996.

[86] G. W. Dahlmann and E. M. Yeatman, "High Q Microwave Inductors on Silicon by Surface Tension Self-Assembly," *Electronics Letters,* vol. 36, pp. 1707-1708, 2002.

[87] R. R. A. Syms, C. Gormley, and S. Blackstone, "Improving Yield, Accuracy and Complexity in Surface Tension Self-Assembled MOEMS," *Sensors and Actuators A: Physical,* vol. 88, pp. 273-283, 2001.

[88] E. Smela, O. Inganas, and I. Lundstrom, "Self-Opening and Closing Boxes and Other Micromachined Folding Structures," in *8th International Conference on Solid State Sensors and actuators and Eurosensors IX.* , Stockholm, Sweden, 1995, pp. 350-351.

[89] M. Boncheva, D. H. Gracias, H. O. Jacobs, and G. M. Whitesides, "Biomimetic self-assembly of a functional asymmetrical electronic device," *Proceedings of the National Academy of Sciences,* vol. 99, pp. 4937-40, Apr 16 2002.

[90] A. Terfort, N. Bowden, and G. M. Whitesides, "Three-Dimensional Self-Assembly of Millimetre-Scale Components," *Nature,* vol. 386, pp. 162-164, 1997.

[91] T. L. Breen, J. Tien, S. R. J. Oliver, T. Hadzic, and G. M. Whitesides, "Design and Self-Assembly of Open, Regular, 3d Mesostructures," *Science,* vol. 284, pp. 948-851, 1999.

[92] D. H. Gracias, J. Tien, T. L. Breen, C. Hsu, and G. M. Whitesides, "Forming Electrical Networks in Three Dimensions by Self-Assembly," *Science,* vol. 289, pp. 1170-1172, 2000.

[93] B. Chang, A. Shah, I. Routa, H. Lipsanen, and Q. Zhou, "Surface-tension driven self-assembly of microchips on hydrophobic receptor sites with water using forced wetting," *Applied Physics Letters,* vol. 101, p. 114105, 2012.

[94] T. Fukushima, E. Iwata, T. Konno, J.-C. Bea, K.-W. Lee, T. Tanaka*, et al.*, "Surface tension-driven chip self-assembly with load-free hydrogen fluoride-assisted direct bonding at room temperature for three-dimensional integrated circuits," *Applied Physics Letters,* vol. 96, pp. 154105(1-3), 2010.

[95] J. Y. Kim, C. Ingrosso, V. Fakhfouri, M. Striccoli, A. Agostiano, M. L. Curri*, et al.*, "Inkjet-Printed Multicolor Arrays of Highly Luminescent Nanocrystal-Based Nanocomposites," *Small,* vol. 5, pp. 1051-1057, 2009.

[96] R. Stewart and J. Smith, "Methods and apparatuses to identify devices," US Patent 6988667, 2002.

[97] E. Saeedi, S. S. Kim, J. R. Etzkorn, D. R. Meldrum, and B. A. Parviz, "Automation and yield of micron-scale self-assembly processes," in *Proceedings of the 3rd IEEE International Conference on Automation Science and Engineering*, Scottsdale, USA 2007, pp. 375-380.

[98] C. J. Morris and B. A. Parviz, "Micro-scale metal contacts for capillary force-driven self-assembly," *Journal of Micromechanics and Microengineering,* vol. 18, p. 015022, 2008.

[99] J. Berthier, S. b. Mermoz, K. Brakke, L. Sanchez, C. Fre´tigny, and L. a. D. Cioccio, "Capillary self-alignment of polygonal chips: a generalization for the shift-restoring force," *Microfluid Nanofluid,* vol. 14, pp. 845-849, 2013.

[100] D. Laskovski, P. Stevenson, and K. P. Galvin, "Lift and drag forces on an isolated cubic particle in pipe flow," *chemical engineering research and design,* vol. 87, pp. 1573-1582, 2009.

[101] H. C. Ko, G. Shin, S. Wang, M. P. Stoykovich, J. W. Lee, D.-H. Kim, *et al.*, "Curvilinear Electronics Formed Using Silicon Membrane Circuits and Elastomeric Transfer Elements," *Small,* vol. 23, pp. 2703-2709, 2009.
[102] J. J. Cole, E. C. Lin, C. R. Barry, and H. O. Jacobs, "Continuous nanoparticle generation and assembly by atmospheric pressure arc discharge," *Applied Physics Letters,* vol. 95, p. 113101, 2009.
[103] S.-C. Park, J. Fang, S. Biswas, M. Mozafari, T. Stauden, and H. O. Jacobs, "A First Implementation of an Automated Reel-to-Reel Fluidic Self-Assembly Machine," *Advanced Materials,* vol. 26, pp. 2942-2949, 2014.
[104] R. L. Panton, "Incompressible flow," 3rd ed Hoboken, N.J.: J.Wiley, 2005, pp. 235-240.
[105] W. Zeng, L. Shu, Q. Li, S. Chen, F. Wang, and X.-M. Tao, "Fiber-Based Wearable Electronics: A Review of Materials, Fabrication, Devices, and Applications," *Advanced Materials,* vol. 26, pp. 5310-5336, 2014.
[106] T. Sekitani, H. Nakajima, H. Maeda, T. Fukushima, T. Aida, K. Hata, *et al.*, "Stretchable active-matrix organic light-emitting diode display using printable elastic conductors," *Nature materials,* vol. 8, pp. 494-499, 2009.
[107] L. Hu, M. Pasta, F. L. Mantia, L. Cui, S. Jeong, H. D. Deshazer, *et al.*, "Stretchable, Porous, and Conductive Energy Textiles," *Nano Letters,* vol. 10, pp. 708-714, 2010.
[108] K.-Y. Chun, Y. Oh, J. Rho, J.-H. Ahn, Y.-J. Kim, H. R. Choi, *et al.*, "Highly conductive, printable and stretchable composite films of carbon nanotubes and silver," *Nature Nanotechnology,* vol. 5, pp. 853-857, 2010.
[109] A. P. Robinson, I. Minev, I. M. Graz, and S. Lacour, "Microstructured Silicone Substrate for Printable and Stretchable Metallic Films," *Langmuir,* vol. 27, pp. 4279-4284, 2011.
[110] B. Y. Ahn, E. B. Duoss, M. J. Motala, X. Guo, S.-I. Park, Y. Xiong, *et al.*, "Omnidirectional Printing of Flexible, Stretchable, and Spanning Silver Microelectrodes," *Science,* vol. 323, pp. 1590-1593, 2009.
[111] E. Menard, K. J. Lee, D.-Y. Khang, R. G. Nuzzo, and J. A. Rogersa), "A printable form of silicon for high performance thin film transistors on plastic substrates," *Applied Physics Letters,* vol. 84, pp. 5398-5400, 2004.
[112] Y. Sun, W. M. Choi, H. Jiang, Y. Y. Huang, and J. A. Rogers, "Controlled buckling of semiconductor nanoribbons for stretchable electronics," *Nature Nanotechnology,* vol. 1, pp. 201-207, 10.1038/nnano.2006.131 2006.
[113] S.-I. Park, Y. Xiong, R.-H. Kim, P. Elvikis, M. Meitl, D.-H. Kim, *et al.*, "Printed Assemblies of Inorganic Light-Emitting Diodes for Deformable and Semitransparent Displays," *Science,* vol. 325, pp. 977-981, 2009.
[114] D.-Y. Khang, H. Jiang, Y. Huang, and J. A. Rogers, "A Stretchable Form of Single-Crystal Silicon for High-Performance Electronics on Rubber Substrates," *Science,* vol. 311, pp. 208-212, 2006.
[115] D.-H. Kim, J.-H. Ahn, W. M. Choi, H.-S. Kim, T.-H. Kim, J. Song, *et al.*, "Stretchable and Foldable Silicon Integrated Circuits," *Science,* vol. 320, pp. 507-511, 2008.
[116] C. M. Stafford, C. Harrison, K. L. Beers, A. Karim, E. J. Amis, M. R. Vanlandingham, *et al.*, "A buckling-based metrology for measuring the elastic moduli of polymeric thin films," *Nature Materials,* vol. 3, pp. 545-550, 2004.
[117] R.-H. Kim, D.-H. Kim, J. Xiao, B. H. Kim, S.-I. Park, B. Panilaitis, *et al.*, "Waterproof AlInGaP optoelectronics on stretchable substrates with applications in biomedicine and robotics," *Nature Materials,* vol. 9, pp. 929–937, 2010.
[118] D. Ruh, P. Reith, S. Sherman, M. Theodor, J. Ruhhammer, A. Seifert, *et al.*, "Stretchable Optoelectronic Circuits Embedded in a Polymer Network," *Advanced Materials,* vol. 26, pp. 1706-1710, 2014.

[119] X. Hu, P. Krull, B. d. Graff, K. Dowling, J. A. Rogers, and W. J. Arora, "Stretchable Inorganic-Semiconductor Electronic Systems," *Advanced Materials,* vol. 23, pp. 2933-2936, 2011.
[120] S. Xu, Y. Zhang, L. Jia, K. E. Mathewson, K.-I. Jang, J. Kim*, et al.*, "Soft Microfluidic Assemblies of Sensors, Circuits, and Radios for the Skin," *Science,* vol. 344, pp. 70-74, 2014.
[121] Y. Li, K.-S. Moon, and C. P. Wong, "Adherence of self-assembled monolayers on gold and their effects for high-performance anisotropic conductive adhesives," *Journal of Electronic Materials,* vol. 34, pp. 266-271, 2005.
[122] H.-s. Kim, E. Brueckner, J. Song, Y. Li, S. Kim, C. Lu*, et al.*, "Unusual strategies for using indium gallium nitride grown on silicon (111) for solid-state lighting," *Proceedings of the National Academy of Sciences of the United States of America,* vol. 108, pp. 10072–10077, 2011.
[123] S. Xu, Y. Zhang, J. Cho, J. Lee, X. Huang, L. Jia*, et al.*, "Stretchable batteries with self-similar serpentine interconnects and integrated wireless recharging systems," *Nature Communications,* vol. 4, 2013.
[124] D.-H. Kim, J. Song, W. M. Choi, H.-S. Kim, R.-H. Kim, Z. Liu*, et al.*, "Materials and noncoplanar mesh designs for integrated circuits with linear elastic responses to extreme mechanical deformations," *Proceedings of the National Academy of Sciences,* vol. 105, pp. 18675-18680, 2008.
[125] D. S. Gray, J. Tien, and C. S. Chen, "High-Conductivity Elastomeric Electronics," *Advanced Materials,* vol. 16, pp. 393-397, 2004.
[126] Y. Hattori, L. Falgout, W. Lee, S.-Y. Jung, E. Poon, J. W. Lee*, et al.*, "Multifunctional Skin-Like Electronics for Quantitative, Clinical Monitoring of Cutaneous Wound Healing," *Advanced Healthcare Materials,* vol. 3, pp. 1597-1607, 2014.